INFORMATION TO USERS

This manuscript has been reproduced from the microfilm master. UMI films the text directly from the original or copy submitted. Thus, some thesis and dissertation copies are in typewriter face, while others may be from any type of computer printer.

The quality of this reproduction is dependent upon the quality of the copy submitted. Broken or indistinct print, colored or poor quality illustrations and photographs, print bleedthrough, substandard margins, and improper alignment can adversely affect reproduction.

In the unlikely event that the author did not send UMI a complete manuscript and there are missing pages, these will be noted. Also, if unauthorized copyright material had to be removed, a note will indicate the deletion.

Oversize materials (e.g., maps, drawings, charts) are reproduced by sectioning the original, beginning at the upper left-hand corner and continuing from left to right in equal sections with small overlaps.

Photographs included in the original manuscript have been reproduced xerographically in this copy. Higher quality 6" x 9" black and white photographic prints are available for any photographs or illustrations appearing in this copy for an additional charge. Contact UMI directly to order.

Bell & Howell Information and Learning
300 North Zeeb Road, Ann Arbor, MI 48106-1346 USA

UMI®
800-521-0600

Applications of a Three-body Potential Model and Crystal Field Calculations to the Simulation of Eu^{3+}, Er^{3+} and Yb^{3+} Environments in $PbO{\cdot}SiO_2$ glass.

Tania Peres

A Thesis
in
The Department
of
Chemistry and Biochemistry

Presented in Partial Fulfillment of the Requirements
for the Degree of Doctor of Philosophy at
Concordia University
Montreal, Quebec, Canada

April 1999

ABSTRACT

Applications of a Three-Body Potential Model and Crystal Field Calculations to the Simulation of Eu^{3+}, Er^{3+} and Yb^{3+} Environments in $PbO{\cdot}SiO_2$ glass.

Tania Peres
Concordia University, 1999

An investigation of the local environment of rare-earth doped lead silicate glasses, using molecular dynamics simulation techniques and crystal-field theory, is presented. The primary focus of the research was to develop a more realistic potential model to better describe the environment surrounding the rare-earth ion. The configurations generated from the MD simulations were used in a point-charge crystal-field model, using C_1 symmetry, to generate the emission spectra of the rare-earth ions. By refining both the aforementioned methods, we have developed a model that can isolate the individual geometrical RE^{3+} environments and calculate the individual emission spectra corresponding to each of the different geometrical arrangements. This in turn has allowed us to obtain a more complete description of the local structure of the RE^{3+} ion with respect to the overall emission spectrum.

Molecular dynamics techniques were employed to simulate undoped and rare-earth doped lead silicate glasses, using both two- and three-body potential models. Structural features of the simulations of undoped $PbO{\cdot}SiO_2$ glass were found to be in excellent agreement with published experimental results, and the three-body potential model produced a marked improvement over the two-body potential model. The

simulations using the three-body potential showed the presence of two networks in the glass; a silicate network and a lead network.

In order to obtain a better description of the effect of the lead ions in silicate glasses, a concentration study on undoped lead silicate glass was performed. At low modifier concentrations (22 mol% PbO) the lead ion was found to behave as a typical modifier. As the concentration of PbO was increased to 70 mol%, the lead ions behaved more as network formers, and an increase in PbO coordination was observed due to the lead ions sharing neighbouring oxygens. The presence of lead rich regions predominated in the glass and the two networks (silicon and lead) were found to be connected via edge-sharing oxygens.

Simulations of the Eu^{3+}-lead silicate glass, using the three-body potential model, showed that the Eu^{3+} ions were found primarily in the lead network, with only a modest presence in the silicate network, showing that the two cations (Pb^{2+}, Eu^{3+}) share similar environments. The average coordination number of Eu^{3+} was found to be 6.5. Furthermore, two main geometrical arrangements were found to exist for Eu^{3+}, a six-coordinated distorted octahedral and a seven-coordinated distorted pentagonal bipyramid.

Since the spectroscopic properties of the dopant ions are dependent on the local environment, an in depth investigation on first coordination sphere of three different rare-earth ions (Eu^{3+}-, Er^{3+}- and Yb^{3+}) doped in lead silicate was performed using the three-body potential model. Although the differences in ionic radii, interionic distance and average coordination number between the three rare-earths was quite small, the three-body potential model successfully reproduced these differences in the bulk structural features, and the results were found to be in excellent agreement with experimental data.

In order to study the clustering of erbium ions, and to examine the possibility of intercluster and cluster-to-cluster energy transfer, a concentration study on the Er^{3+}-doped lead silicate glass was performed. Erbium-erbium clustering was observed at concentrations as low as 2.0% Er^{3+}. An increase in the concentration of Er^{3+} in the glass caused an increase in Er-O coordination. This effect is due to an increased amount of erbium-erbium clustering, which resulted in the erbium ions sharing oxygens within the same coordination sphere (3.2Å).

A successful validation of the simulated structural model of the $PbO{\cdot}SiO_2{:}RE^{3+}$ glass was performed through a comparison between the room-temperature emission spectra of the experimental glass and the calculated emission spectra of the simulated glass. The simulated spectra were obtained using a point-charge crystal-field model, with a C_1 symmetry for the RE^{3+} environment. The splitting of the J manifolds, and the corresponding transition probabilities of the simulated RE^{3+} ions were also calculated.

Simulations of $^2H_{11/2}\rightarrow{}^4I_{15/2}$ and the $^4S_{3/2}\rightarrow{}^4I_{15/2}$ and $^4I_{13/2}\rightarrow{}^4I_{15/2}$ transitions in the Er^{3+} ion were found to be in moderate agreement with the corresponding room temperature experimental spectrum. The simulation of the $^5D_0\rightarrow{}^7F_J$ (J=0-4) transitions in the Eu^{3+} ion spectra were found to be in good agreement with the experimental emission spectrum. The most important results in our simulations of the Eu^{3+} emission spectrum is that we were able, with confidence, to separate and simulate the emission spectra of a rare-earth ion based on the specific geometrical arrangements of the local environments.

ACKNOWLEDMENTS

This thesis would never have been possible if it were not for the unconditional support of my thesis supervisor, Dr. John A. Capobianco. I am grateful to him for his guidance, patience and knowledge. Most importantly, however, I am grateful to him for giving me the freedom to grow as a scientist, encouraging me to pursue my goals and for taking the time to understand me as a person.

I would like to extend my gratitude to the members of my research committee, Dr. Peter H. Bird, Dr. David Jack and Dr. Lawrence D. Colebrook for their contributions to this thesis, for their patience with my "workstation crises", and for serving on my research committee.

I am indebted to Dr. Stephen H. Garofalini for the three-body potential model, for allowing me to temporarily monopolize his workstations, and for the help he so freely gave me. During my three visits to Rutgers University, Dr. Garofalini was extremely kind and generous, always making me feel like a welcome part of his research group. I would like to extend my sincerest thanks to Dr. David Litton for helping me work through the intricacies of the potential model and for his wonderful friendship.

I would also like to thank Dr. André Monteil for allowing me to visit his laboratory in Angers. I would like to extend a special thank you to Dr. Stephane Chaussedent for his tremendous help with my spectra simulations, and for his hospitality during my stay in France.

Throughout my years at Concordia, I have had the opportunity to work and befriend a wonderful group of people. I would like to thank Dr. Guy Cormier for helping me during the early stages of my thesis, Dr. Pierre-Paul Proulx for having the patience to

work with me in the spectroscopy lab, and Dr. Pierre Kabro for his tremendous help in preparing for my seminars. In particular, I would like to extend my warmest gratitude to Elizabeth Sourial. During the three years we spent working side by side, she was not only a colleague I could depend on, but also a dear friend. I would also like to thank Elham Ghobadi and Sarah Anderson for their friendship, support and never-ending help. I would like to say thanks to Sean Hughes for always having a big smile way too early in the morning and for his all his help, and to Fiorenzo Vetrone, Carmela Mancuso, Tania D'Alesio and Rafik Naccache for making the lab a great place to be.

A well known proverb says that if you can count your true friends on one hand you are a very lucky person, and so with that I would also like to thank all my friends who supported and stuck by me throughout this thesis.

Lastly, I would like to thank my family for their support, encouragement, patience and love through all the ups and downs that accompanied this work. This thesis is as much yours as it is mine because I would have never been able to do it without you. I love you all very much.

Anni è bicchieri di vino non si contano mai

TABLE OF CONTENTS

LIST OF FIGURES

CHAPTER 1

1.0 INTRODUCTION

Glass has a very long and interesting history, yet information on its structure still remains the subject of continuing controversy. Before the advent of chemistry and physics, the glass-making technique was considered a proprietary craft and trade secrets, developed on an alchemical basis, were heavily guarded [1]. Moreover, Assyrian cuneiform tablets, dating to approximately sixth century BC, reveal recipes for glass composition which do not differ greatly from some of the glasses commonly used today [1].

The origins of the lead crystal industry in the Western world are largely due to the work of George Ravenscroft in 1675 [2]. Prior to this date, the glassmaking center was located in Italy where glass was produced using soda-lime compositions for both utilitarian and luxury purposes. Carried by the Italian craftsmen, the traditions of glassmaking spread throughout Europe in the 16th and 17th centuries. The Venetian tradition was established in England in 1575 and continued for almost a century through the Puritan period and into the Restoration in 1660 [2]. At this time in England, a very important change occurred in the outlook of glass production which eventually led to the development of English lead crystal, variations of which are still used in fine glassware to this day.

These new lead glasses were called flint glasses and had unusual clarity for glass of that time period. Ravenscroft used English flints, a very hard and pure form of quartz, as a supply of silica. The use of flint pebbles, which are low in iron, were in part responsible for the added clarity. The flint glasses were not only of greater brilliance but

could be readily decorated by cutting, since they were considerably easier to grind and polish than existing soda-lime-silica glasses.[2]

Improvement in lead crystal in the 20th century has not been so much a change in the basic glass formulation, but rather is due to significant improvements in the purity of raw materials, refractories and melting furnaces. Consequently, these improvements have resulted in the degree of perfection found in modern lead crystal glasses such as Steuben art glass.

The structural properties of glass are still, however, quite controversial. One of the main reasons for the continuing debate is due to the nature of the material. Glass possesses a degree of atomic disorder characteristic of liquids, however, the atoms maintain permanent positions with respect to the location of their neighbours, which is characteristic of solids [3]. As a result, methods such as neutron and X-ray diffraction or EXAFS (Extended X-ray Absorption Fine Structure), which are commonly used to analyse crystalline solids and molecular groups, are only able to predict average structural characteristics in glasses. It was therefore necessary to search for a new technique that would yield the exact ordering by means of a statistical description through the distribution of interionic distances [4].

With the application of atomistic level simulation techniques such as Molecular dynamics (MD) and Monte-Carlo (MC), unambiguous analysis of local features around individual atoms is possible. These techniques can also calculate average structural, thermodynamic and transport properties of a given material. If the average structural features observed in the simulations are identical to those observed experimentally, then specific structures which create those averages can be explicitly obtained by the simulation rather than just inferred from the data.

In this thesis, molecular dynamic simulations were used in order to investigate the structure of undoped and trivalent rare-earth doped lead silicate glasses. The glasses under investigation belong to the oxide family of glasses which are also termed covalently bonded glasses which contain oxygen as the anion and the number of ligands present depends on the radius ratio of the cation:oxygen ion. In addition, the luminescent properties of the doped trivalent rare-earth ions are studied using a variety of other computer techniques.

1.1. THE STRUCTURE OF GLASSES

1.1.1. Definition of a Glass

Glasses are amorphous materials which may be defined as non-crystalline solids obtained by freezing super cooled liquids [5], yet they still possess the mechanical properties (elasticity and strength) which are used to characterize solids. There is a large percentage of materials, including metals, which may be produced in the amorphous state, however, the absence of crystalline structure does not qualify them to be classified as glasses. A rigid amorphous solid is called a glass, if upon heating, it turns into a liquid in a reversible fashion [3,6]. Moreover, although the glassy state is intrinsically a non-equilibrium configuration, it is also required to be stable against crystallization over a long period of time.

A more quantitative description of a glass may be given in terms of the glass transition temperature, T_g, which is independent of composition and is commonly associated with the liquid viscosity, n, of the system [1]. Specifically, T_g is the point at which the attainment of equilibrium is no longer possible with continual cooling and this corresponds to a value for n of 10^{13} poise. Although the atoms or molecules of a liquid

are able to undergo relatively large displacements, their displacements in a glass are restricted to thermal vibrations around an average fixed position. In fact, a glass is commonly described as a liquid which has been frozen in place [7].

From the basic definition of an amorphous material, a glass can therefore be described as lacking any symmetry, periodicity and long range order. The structure of glasses is a disordered network characterized mainly by the coordinations of network formers (such as B, Si, Ge, As and P) by anions (such as O and F) and these units are linked together at the corners creating short-range order [8]. Hence, to completely define the structure, it would be necessary to specify the coordinates and thermal parameters for every atom present in the glass; which is not possible for any real sample. As a result, several hypotheses, with certain variations and amplifications, have been developed about the structure of glass and the conditions for its formation. It is therefore important to review some of the more traditional models describing glass structure.

1.1.2. Structural theories and models

1.1.2.1. The Random Network Theory

The random network theory was first introduced by Zachariasen [9] and subsequently modified by Warren [10] to describe the structure of conventional oxide glasses. The basis of this network hypothesis, however, was developed from the earlier work of Goldschmidt [11] in the mid 1920's.

Zachariasen [9] postulated that the atoms in a glass are linked together by interatomic forces and the interatomic distances are essentially the same as those in the corresponding crystals. Moreover, if the free energy of the glass is to be comparable to that of the crystal, the oxygen polyhedra in the glass and crystal must be similar.

Extended three dimensional networks are formed in glasses but unlike crystals, they are linked together randomly to form a non-periodic structure which lacks long range order. In order to obtain a random network relatively free of distortion, Zachariasen [9] derived a set of criteria governing glass formation which are as follows:

(1) The oxygen atoms are linked to no more than two glass (network) forming cations.

(2) The number of oxygens (coordination number) around a glass forming cation should be four or less.

(3) The oxygen polyhedra should share corners, not edges or faces.

(4) The polyhedra are linked together by at least three corners in a three-dimensional network.

These conditions are fulfilled by the oxides of type R_2O_3, RO_2, and R_2O_5, where R= B, Si, P, Ge and As. It is also important to note that a glass can still be formed if one of the above criteria is not met, however, it would be energetically less favorable than one for which all the criteria are satisfied. Zachariasen's theory proved to be an accurate prediction of glass formation and has withstood the test of time becoming the basis for the continuous random network (CRN) theory.

Warren et al. [12], calculated X-ray diffraction patterns for silica (SiO_2) based on the CRN theory and their calculations were in excellent agreement with interference curves obtained experimentally. The authors later extended the theories of Zernike and Prins [13] by applying a Fourier analysis proposed by Debye and Menke [14] to the X-ray interference patterns for amorphous silica in order to calculate radial distribution functions. They were also able to calculate average coordination numbers and bondlengths of the ions present by using a crystalline counterpart as a model for the base structure. The X-ray analysis, however, could only provide average structural information

for distances less than 7 Å from the center of an ion. Nonetheless, Warren's work supported the basic premise of the Zachariasen's theory and the CRN model is still used today to describe the structure of vitreous silica.

1.1.2.2. The Crystallite Theory

The early crystallite theory proposed by Lebedev [15], envisioned glass as an assembly of very small crystals, called crystallites with sharp external boundaries. Due to the interpretation of X-ray data, early researchers, such as Randall et al. [16] supported the early crystallite theory. By using photographic techniques to study X-ray diffraction patterns of oxide glasses, it was noted that the diffuse halos, characteristic of vitreous materials, were coincident with prominent Bragg peaks, or groups of Bragg peaks, in the powder diffraction patterns of related crystalline materials [7].

Valenkov and Porai-Koshits [17] further expanded on Lebedev's ideas and developed a modified theory in which these discrete crystallites were not found in simple glasses. More specifically, the modern crystallite theory postulates that there are spatial fluctuations in the degree of intermediate range order within the vitreous network such that the more highly ordered regions (the crystallites), where the atomic arrangement approaches those in the related crystalline materials, are interconnected by regions with a lower degree of order [17].

In a vitreous network such as SiO_2, it is inherent that there will be fluctuations in the degree of local order. Hence the essential difference between the modern crystallite theory and the random network theories is in the magnitude of these fluctuations, particularly within the range of 1-20 Å and in the frequency that local regions exhibit crystalline structure. Moreover, in both theories, a continuous three-dimensional network

for simple oxide glass is formed. Figure 1.1.2.2.1. shows a schematic representation of for a pure glass forming oxide, A_2O_3, according to the random network theory, the modern crystallite theory. The corresponding crystalline material is also illustrated.

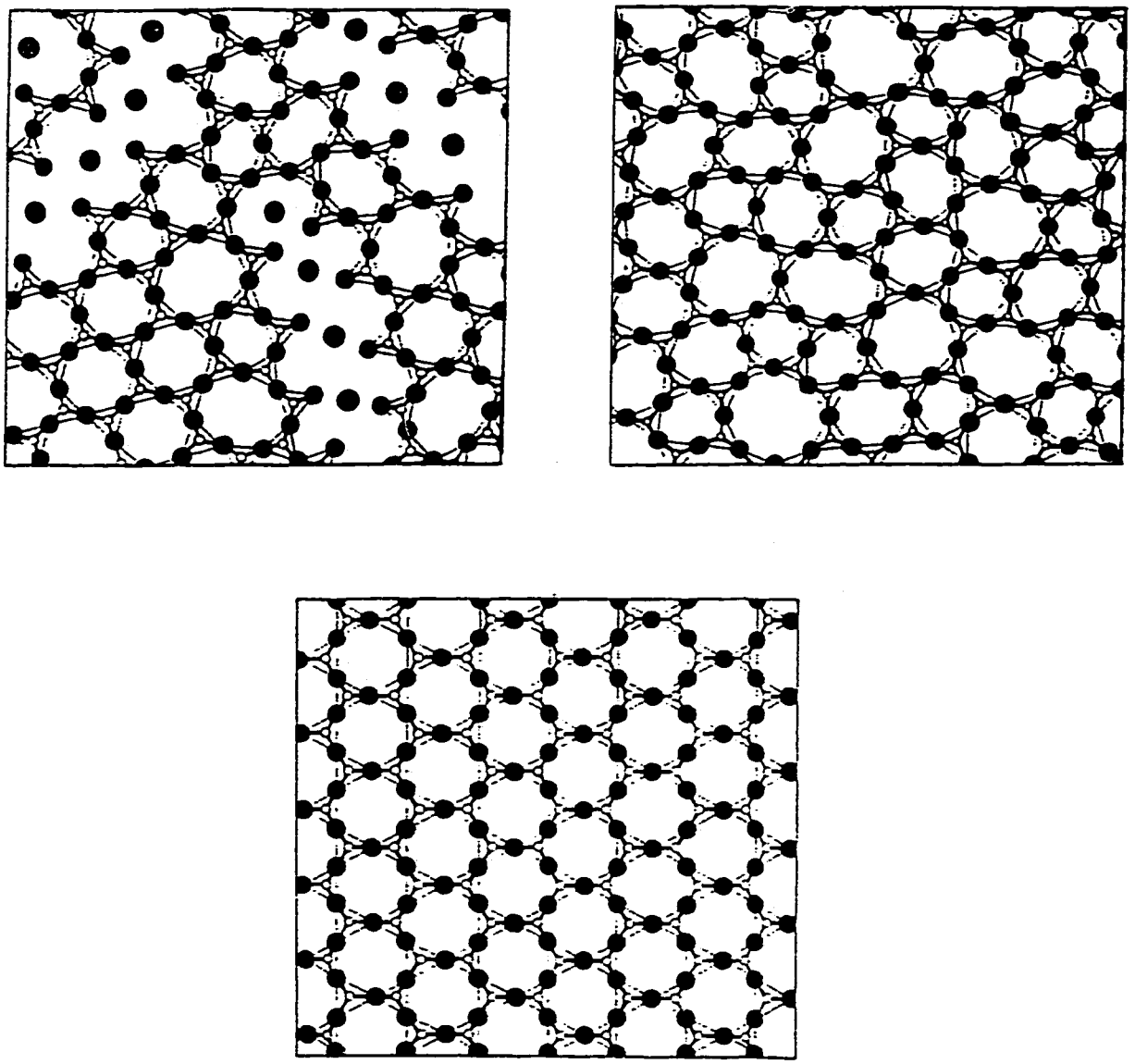

Figure 1.1.2.2.1. A schematic representation of vitreous A_2O_3 based on the modern crystallite theory (top left) and the random network theory (top right) and the corresponding crystalline material (below) (A_2O_3) [7].

1.1.2.3. The Structon and Vitron Theories

In order to obtain a better understanding of the structure of glass, Huggins [18] developed the structon theory, which analyses density based on the composition of a glass. Huggins [18] plotted measured density values, obtained by other researchers, versus composition and found that breaks occurred in the curves for certain compositions. These breaks were attributed to structons (structural elements) in the glass structure and these structural units are atoms/ions with their respective coordination. [8]. For example, for vitreous silica, the only atoms present are Si and O which are coordinated with 4O and 2Si, respectively thus these two structons are designated Si (4O) and O (2Si). If a modifier, such as sodium (Na_2O), is introduced into vitreous silica, the following structons are assumed: Na (6O), O (2Si, Na) and O (Si, 3Na). The relative proportions of the individual structons change with glass composition and can be calculated. The usefulness of this theory is questionable and tends to be regarded more as a hypothesis. Nonetheless, this hypothesis proposes a method for the nomenclature of structural units which aids in understanding properties based on composition.

The fundamental idea behind Tilton's vitron theory [19] is that the tetrahedron(such as SiO_4) is the basic 'building block' of a glass. In crystals, the tetrahedron form six-membered rings while in glasses five-membered rings are found. In a glass, these rings form regular pentagonal dodecahedra from the tetrahedra which are called vitrons [19]. Tilton affirms that further growth of these 'building blocks' is possible only with the distortion of the closest five membered rings, such that the individual components are linked together across irregular regions. A symmetry of five in crystals is impossible and this is said to be the cause of glass formation with SiO_2. Although Tilton succeeded in calculating the density of vitreous silica on the basis of this perception, his

structure proposal has neither been proven for SiO_2 glass nor is it transferable to other glasses. This model does, however, deserve recognition for its fundamental idea which has been employed by Robinson [20], who assumed a model based on pentagonal dodecahedra in order to explain the structure of vitreous silica.

1.1.3. The structure of silicate glass

In pure vitreous SiO_2, all of the oxygen (O^{2-}) ions represent bridges between two neighbouring Si^{4+} ions, and are called bridging oxygens. The incorporation of an alkali or alkaline-earth metal into SiO_2 breaks these bridges and as a result, neighbouring Si^{4+} ions are formed which contain singly bonded O^{2-} ions such that no direct bonding among the silicon ions occurs. These oxygens are known as non-bridging oxygens. Silicate glasses are therefore, comprised of a disordered three-dimensional silicate network which is randomly modified by the presence of the alkali or alkaline earth metals. The limit of formation of these glasses is reached when every SiO_4 tetrahedral unit is shared only at three corners. For example, in the case of lead (R=Pb), the limit of formation would be reached at the composition $RO{\cdot}2SiO_2$. As the concentration of RO increases to the composition $RO{\cdot}SiO_2$, the three dimensional network continues to break down into infinitely long chains. Since the connection of the tetrahedra is not perfectly uniform, the chains will also be crosslinked among one another. At even higher alkali concentrations, the chains continue to break down, until at the composition $2RO{\cdot}SiO_2$, isolated tetrahedra, which no longer have any connection across Si-O-Si bridges, are present.

The basis of glass formation is therefore, the network formed by the SiO_4 tetrahedron. The average Si-O interionic distance is 1.62 Å and the average O-Si-O bond

angle is found to be 110° [21], which is indicative of the well defined short range order in the glass. The Si-O-Si bond angle has a broad distribution ranging from 120° to 180° with a maximum at 144°. The broad distribution for $\phi_{Si\text{-}O\text{-}Si}$ is due to the introduction of randomness incurred by the typical disorder of corner-sharing tetrahedra [21].

The cations which form this network building polyhedron are called *network formers* (such as Si, Ge, B, As, P), while the cations which break down the network are called *network modifiers* (alkali and alkaline earth metals). This terminology is illustrated in Figure 1.1.3.1. by a three-dimensional representation of $PbO{\cdot}SiO_2$ glass.

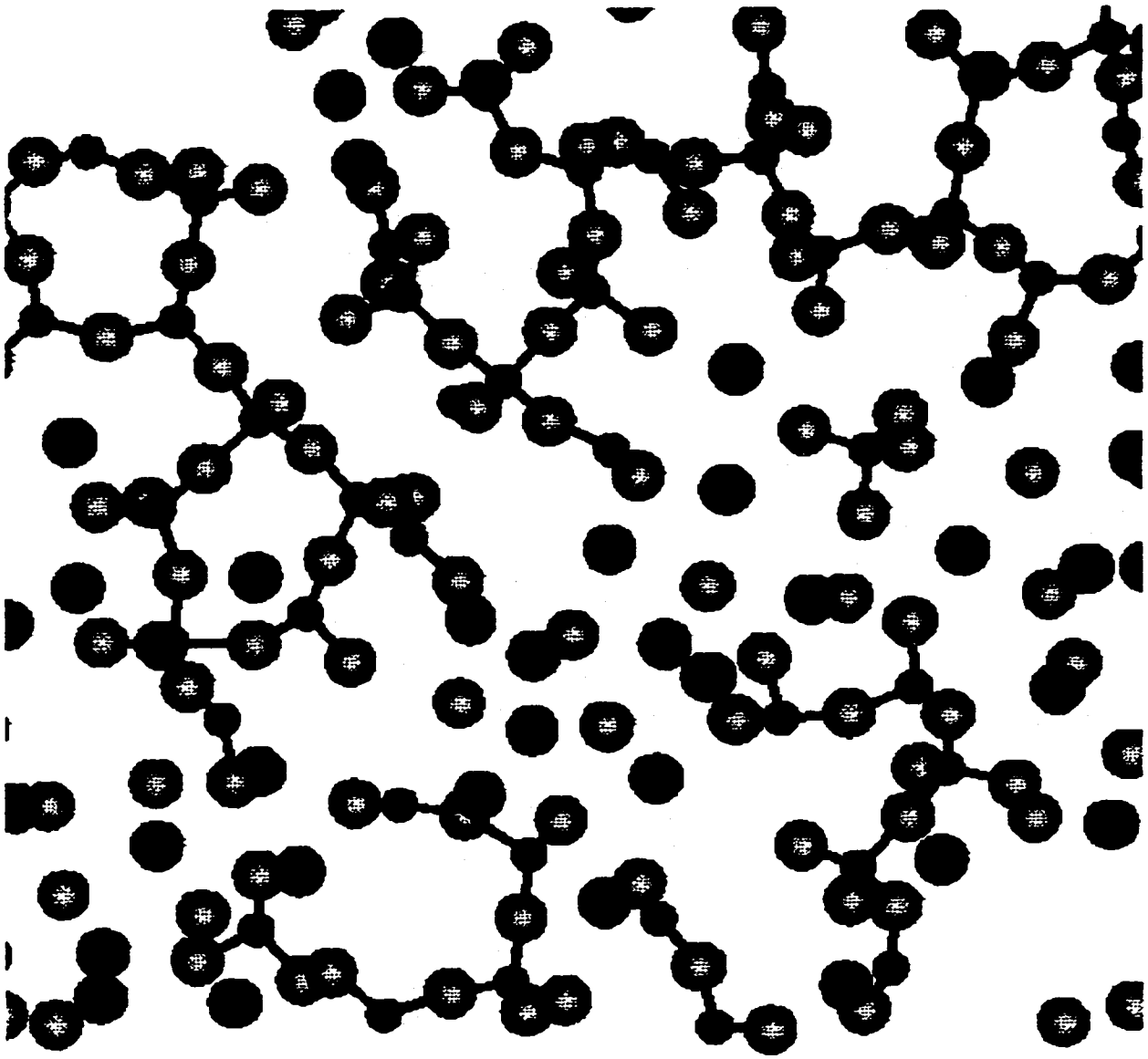

Figure 1.1.3.1. Computer graphics of a slice (xy) of the simulated $PbO{\cdot}SiO_2$ glass. The large red spheres represent the lead modifier ions while the small black spheres represent the silicon ions (network formers), and the large blue-gray spheres represent the oxygen ions.

1.1.4. Lead in silicate glass

Lead containing glasses are used extensively in numerous industrial and technological applications such as glass lasers, underwater optical communication devices, and biomedical sensors. In addition to the more conventional industrial applications, low-melting glasses and glass ceramics have also been widely used in the field of electronic technology as electron multipliers and micro-channel plates. [22]. This is due to the specific properties of the lead ion (such as large polarizability, high non-linear index of refraction and low coordination), which results in the ability to prepare stable glasses containing a composition range up to 95 mol% PbO [23]. In contrast to other traditional modifiers, lead has also been recognized for its glass forming capabilities, which are attributed to the high polarizability of divalent lead. At PbO concentrations below 30 mol%, lead behaves as a classical modifier. However, at higher concentrations, PbO is more of a network former displaying PbO_3 and PbO_4 structural units. Moreover, the presence of a high concentration of PbO in the random network can drastically influence the spectroscopic behavior of the impurity ion, either by forcing the impurity ion to be placed in an uncommon coordination geometry, and/or by affecting its transition probabilities [24]. In recent years, high technology applications such as nuclear scintillators and upconversion laser devices have demanded a greater understanding and control over these and other structurally related optical properties. Rabinovich [25], in an excellent review article, summarized the behavior of PbO in a variety of different glasses. This next section will review some of the more relevant studies on lead silicate glass pertaining to this thesis.

1.1.4.1. Bulk characterization of lead silicate glass

One of the first researchers to take interest in lead silicate glasses was Bair [26]. Using X-ray diffraction, he studied binary glasses with the PbO concentration ranging from 10-60 mol%. Bair used the trial and error method to interpret his results and reported Pb-O and Pb-Si interionic distances of 2.5 Å and 3.80 Å, respectively, which showed a good agreement between the observed and calculated distances. Depending on the composition of the glass, the Pb-Pb interionic distance varied between 4.00Å and 6.50Å. Bair concluded that the Pb-Pb distance was variable, and assumed that the distribution of lead atoms was of the gas type and as a result it was impossible to determine a lead-lead coordination number. He suggested that the structure of lead silicate glass was identical to that of soda-silica glass [25,26] except that two sodium ions were replaced by a lead ion. Thus, according to Bair, these glasses would consist of a continuous, randomly oriented silicon-oxygen network with the lead behaving as a pure modifier.

Krough-Moe [25,27] performed an X-ray diffraction study on $PbO{\cdot}0.7SiO_2$ which corresponds to a PbO composition of 58.8 mol%. Results for the Pb-O and O-O interionic distances were in agreement with those obtained by Bair, however, the Pb-Pb distance differed dramatically. The author reported a Pb-O interionic distance of 2.27 Å, which corresponds to a lead-oxygen coordination ranging between 6 and 10. Krough-Moe reported a value of 3.90 Å for the Pb-Pb interionic distance as well as a lead-lead coordination of 6. In contrast to Bair [26], Krough-Moe[27] believed that the structure of lead silicate glass with high lead content could not be described by the random network theory but rather by an arrangement of disordered cubes with the lead ions in the corners.

The edge length of the cube corresponds to the 3.90 Å found for Pb-Pb and the shortest Pb-O bond distance is 2.27 Å. In addition, each cube could accommodate one SiO_4 tetrahedral unit. According to this structural arrangement, a glass containing 60 mol% PbO, approximately 30 mol% of the lead cubes would be empty, which Krough-Moe attributed to the relatively large molar volume of 65.3 Å for lead silicate glass.

Bagdyk'yants and Alekseev [25,28] examined a series of lead silicate glasses with varying PbO concentration using electron diffraction techniques. The glasses studied contained 20 to 60 mol% PbO. The authors report a Pb-Pb interionic distance of 4.2 Å and a lead-lead coordination of 9. In the case of glasses with low lead content, the lead ions behave as classical modifiers and are randomly distributed throughout the glass in between the three-dimensional silicate network, with each lead being connected via two oxygens. Bagdyk'yants and Alekseev postulated that as the concentration of lead increases, the lead oxygen coordination number increases to 6, as reported by Krough-Moe [27], and the three dimensional silicate network begins to break down to a point where it no longer exists.

A conclusive study by Brosset [25,29] showed that the position of the Pb-Pb peak at 3.9 Å is independent of the PbO content. This implies that the lead groups have a definite structure with the possibility of covalent bonding between Pb-Pb at 3.9Å. Similar results for the Pb-Pb peak were also observed by Mydlar et al. [30].

Mydlar et al. [30] performed an X-ray diffraction study of $2PbO{\cdot}SiO_2$, $PbO{\cdot}SiO_2$ and $PbO{\cdot}2SiO_2$ glasses. An important observation in their studies was that the Pb-Pb peak at 3.8 Å for both the $PbO{\cdot}SiO_2$ and $2PbO{\cdot}SiO_2$ glasses was sharp, indicating that the distribution of lead in these glasses cannot be completely random. With respect to

the lead-lead coordination, they reported one closest neighbour at 3.6 Å, two more leads at 4.15 Å and a fourth lead at 4.8 Å. For $PbO{\bullet}SiO_2$, the Pb-O interionic distance was found to be within a range of 2.15 Å and 2.50 Å, with the lead ion coordinated by 4 oxygens, the first two at 2.2 Å and the other two oxygens at 2.53 Å and 2.8 Å. Furthermore, this distribution of distances is similar to that found in red PbO and crystalline $PbSiO_3$. A similar structure was reported for $2PbO{\bullet}SiO_2$ glass with the primary lead-lead peak at 3.8 Å as well as a lead-oxygen coordination of 8, with four nearest neighbours, and four more distant neighbours, resembling yellow PbO, which also has a lead-oxygen coordination of 8. The resemblance between the structures of vitreous and crystalline lead silicates has also been shown by infrared [31] and NMR spectroscopy [32].

Morikawa et al. [33] used X-ray diffraction analysis to investigate the structure of $2PbO{\bullet}SiO_2$ glass. The authors report a Pb-O interionic distance of 2.35 Å and a coordination of 4 (the number of oxygens surrounding a lead ion). These values are in good agreement with those reported for red PbO [33,34]. In contrast to Mydlar et al.[30], Morikawa et al.[33], believed that the atomic arrangement of red PbO is not a suitable structural model for $2PbO{\bullet}SiO_2$, due to the fact that chemical shifts of ^{207}Pb indicate that the lead ion in the glass is more ionic than the lead ion in red PbO. This point has been the subject of controversy by several researchers [30,33,35-38] and in attempt to clarify the contradiction, Montenero et al. [39] performed and EXAFS investigation on lead ions in $(PbO)_x{\bullet}SiO_2$ glasses ranging in composition from 38.6 to 83.7 mol% PbO. They found that no chemical shift in the Pb absorption edge was observed as the concentration of PbO was increased to high lead silicate glasses, thus indicating that the

nature of the chemical bonds does not change from the crystalline lead oxide to the glasses of different compositions. Montenero et al. [39] also state that they found no significant change of the average local structural parameters between red PbO and the glass.

Morikawa et al. [33], also report that most of the lead ions form covalent PbO_4 pyramids and subsequently, dimeric or trimeric PbO_4 pyramids form zigzag chains acting as glass formers. They suggest that these zigzag PbO_4 chains could be bridged by units such as $[Si_2O_7]^{6-}$ dimers, $[Si_3O_{10}]^{8-}$ trimers, $[Si_4O_{12}]^{8-}$ tetrameric rings, $[SiO_3]^{2-}$ chains and ionic PbO_6 octahedra.

Information on the degree of polymerization and distribution of low-molecular weight silicate anions in binary lead silicate glasses was reported by Götz et al. [37] using organic derivitization/chromatographic techniques. Employing various chemical methods, the authors quantified the type and percentage of silicate groupings present in a number of lead silicate glasses. These techniques permit the separation and identification of silicate anions in the range monomeric, $[SiO_4]^{4-}$, to the linear and branched hexameric anions, $[Si_6O_{19}]^{14-}$. They have also reported a quantification of various classes of silicate anions, namely, (i) polysilicate chains $[SiO_3]_n^{2-}$, (ii) two- and three dimensional silicate units, (iii) phyllosilicates and (iv) higher molecular silicates. For $PbO{\cdot}SiO_2$ glass, Götz et al. [37] report that approximately 85% of the silicate anions are in the form of phyllosilicates and higher molecular silicates. The remaining 15% were attributed to unidentified low-molecular anions. However, the authors ascribe a substantial error on the quantification of any species present at concentrations lower than 30%. In addition, the authors suggested that glasses containing low concentrations of PbO (increasing percentages of SiO_2), promotes the formation of higher polymerized silicate groupings, while glasses with high

PbO content are characterized by the presence of few low-molecular weight silicate anions. Similar results were reported by Imaoka et al. [35] using X-ray diffraction data and the pair function method to analyse $PbO{\cdot}SiO_2$ and $2PbO{\cdot}SiO_2$ glasses.

Yamada et al. [23] showed by neutron scattering techniques that the short range order in the lead silicate $(PbO)_x{\cdot}(SiO_2)_{1-x}$ glasses are well described by $PbSiO_3$ and $Pb_3Si_2O_7$ crystals but not by crystalline Pb_2SiO_4. The implication of this study is that for glasses, the short range configuration can be accurately described by tetrahedral chains containing isolated monomeric or double tetrahedra rather than with ring structures, which would require middle range atomic order. The authors also state that it is the polarizability of Pb^{2+} which causes the asymmetric coordination of oxygen ions around the lead ions, leading to the chain structure observed in the absence of the Si-O network.

In agreement with Yamada et al. [23], several subsequent studies [22,31,32,40] using techniques such as XPS, NMR and IR spectroscopy have attributed the behavior of lead in lead silicate glasses, of varying concentrations, to its polarizability. The polarizability of lead is concentration dependent and increases as the concentration of PbO increases in the glass. This results in an increase in the covalency of Pb-O which accounts for the fact that at higher concentrations, PbO is more of a network former displaying polymeric chains of PbO_3 and PbO_4 structural units. The presence of this secondary lead network has also been observed computationally by Cormier et al. [41] in at detailed molecular dynamics study of undoped and doped Yb^{3+}-lead silicate glass.

The main conclusion derived from all of the above studies on lead silicate glasses is that the interaction between lead ions is a very important structural factor. Moreover, at high lead concentrations the three-dimensional silicate network is broken down and PbO

becomes the main glass former. Consequently, the backbone network structure of the glass consists of PbO_4 pyramid polymeric chains connected together through SiO_4 tetrahedra.

1.2 IONIC DOPING

The absorption and/or emission of light by optically active materials is one of the most ubiquitous phenomena in modern technology. In one way or another, such processes are responsible for fluorescent lighting, cathode ray tubes, lasers, optical amplifiers and photochromic sunglasses, to name just a few. The manner, in which the constituent materials function, however, depends on subtle and often poorly understood factors at the molecular and atomic level.

To obtain a clearer insight on the function of these constituent materials, spectroscopists have examined the local structure of the optically active dopant ions (rare-earths, transition metals). The focus of their work has been the study of the luminescence of inorganic materials. Luminescence is the ability of a material to emit light when properly excited. Thus, viewed in the most general sense, emission of light has been the basis of all knowledge with respect to atomic and molecular structure since a great deal of information regarding the structure of the material, the symmetry, the energy levels, the role of defects and internal happenings such as energy transfer can be obtained. However, due to the disordered nature of glass, detailed information on the atomic structure has been difficult to acquire and only some effective averages over the distribution of different physical environments has been obtained.

Research on the local structure of dopant ions in insulating glasses is of particular interest because it aids in the interpretation of the optical properties of rare-

earth ions in disordered systems. This is due to the fact that optical properties of a glass or crystal can be drastically altered by the addition of small quantities of an ionic impurity.

Lead silicate glasses have been shown to possess interesting spectral properties when acting as hosts for transition metals, lanthanide and actinide ions [24]. Lead glasses continue to be studied extensively due to the fact that lead oxide is one of the primary components of optical glasses.

1.2.1. Rare-earth ions as dopants

The term rare-earths or lanthanides are assigned to the fifteen elements, atomic numbers 57 through 71 in the periodic table which represent the 4*f*-transition elements. The 4*f* elements form the longest continuous series of chemically similar elements in the periodic table. Starting with La($4f^0$) and continuing along the group to Lu($4f^{14}$) an electron is successively added to the 4*f* shell until a total of 14 is reached. The neutral atoms have a ground state electronic configuration of a Xe core ($1s^2 2s^2 2p^6 3s^2 3p^6 3d^{10} 4s^2 4p^6 4d^{10} 5s^2 5p^6$) with two or three outer electrons ($6s^2$ or $5d^1 6s^2$). The +3 oxidation state is the most common and in this case, all the 5d and 6s electrons are removed and the 4f shell is left partially occupied with the ground state configurations of the form $[Xe]5s^2 5p^4 4f^n$.

The luminescence of rare-earth ions in glass has been the subject of renewed interest since, unlike other luminescence centers in glasses, their optical spectra consist of a series of sharp lines, which closely resemble the corresponding free-ion spectra. In the rare-earth ions, the electronic transitions occur among the inner, shielded 4*f* electrons, and as a result, both the absorption and emission bands are relatively sharp and are not greatly

influenced by their surroundings [3]. Therefore, large shifts in the emission bands are not expected for glasses of varying compositions.

The spectral characteristics of rare-earth ions are strongly host dependent, and the crystal-field splitting will vary from host to host, reflecting the different symmetries and strengths of different local environments. Rare-earth ions enter into a glass as network modifiers [1] and thus exhibit variations in coordination. Levin and Block [42] deduced that the trivalent rare-earths may have coordination numbers of 6, 7, 8 and 9 depending on the ionic radii, which ranges across the group from 1.06 Å and 0.85 Å for La^{3+} to Lu^{3+}, respectively. The rare-earths of interest in this study are Eu^{3+}, Er^{3+} and Yb^{3+} ions doped in lead silicate glass. Since the optical spectra of rare-earths are dependent on the local environment of the ions, the following section will be devoted to reviewing models, based on spectroscopic studies, to describe the structure of these and other dopants in oxide and fluoride glasses.

1.2.1.1. Europium

The Eu^{3+} ion has a relatively simple energy level structure with a non-degenerate ground state ($^7F_0$) and a non-degenerate emitting level ($^5D_0$) which makes it an ideal probe for crystal-field analysis for both crystalline and vitreous materials. Although a europium doped glass is not a laser medium, the absorption and emission from the singlet (J=0) levels of Eu^{3+} facilitate the study of linewidths and positions without the complications of overlapping lines [43]. These spectral features of europium provide a stepping stone towards the analysis of other rare-earth ions in glass.

In 1963, Kurkjian et al. [44] performed an extensive study of the effect of glass composition on the luminescence of the Eu^{3+} ion in various alkali and alkaline earth silicate glasses. They studied glasses of the series $xNa_2O\cdot(1-x)SiO_2$:1mol%Eu_2O_3, where x=0.15 to 0.45. The authors observed a shift in the position of the $^5D_0 \rightarrow {}^7F_0$ transition as the concentration of sodium increased. This behavior is explained on the basis of the increased interaction between europium and oxygen as a result of the breakdown of the silicate network with increasing modifier content [3]. The authors adopted a model whereby for a given glass composition, the Eu^{3+} ion is in a network-modifying position and is surrounded by seven oxygens, which are both bridging and non-bridging. As the concentration of the network modifier increases, more non-bridging oxygens surround the Eu^{3+} ion, thus increasing the crystal-field strength due to an increase in the ionic character of the Eu-O bond [45].

Gallagher et al. [46] measured the absorption and emission spectra of trivalent europium in borate glasses. The behavior of Eu^{3+} was found to be similar to that in silicate glasses, however, the intensity of the absorption peak increases and the peak broadens. The Eu-O interaction was found to be less in the borate glass than in the silicate glasses, as indicated by the increase of the emission wavelength of the $^5D_0$ -> $^7F_0$ transition. From a series of studies involving (i) a two-component borate glass containing Na_2O or BaO and (ii) a complex borate glass containing equimolar amounts of Na_2O, K_2O, CaO, SrO and BaO as modifiers, the authors were able to draw conclusions concerning the symmetry, non-uniformity and crystal-field of the europium sites. The trends observed with the network modifiers indicated the presence of europium in clusters, which implies that the europium is situated in sites of relatively high symmetry and

uniformity. The authors reported a direct relationship between the structure and modifier content whereby the structure tends to become disrupted with increasing modifier concentrations of 10 to 20 mol%, thus decreasing the symmetry and uniformity. Higher modifier concentrations of 30 to 35 mol%, resulted in an increase in the symmetry, uniformity and bonding due to the formation of the maximum number of boron ions in fourfold coordination. [46]. As the concentration of modifier increased and subsequently the number of non-bridging oxygens, the Eu-O interaction was found to increase in the same manner as in silicate glasses.

Rice and Deshazer [43,47] investigated the relationship between the absorption and emission spectra of europium ions in a borosilicate glass and europium in monoclinic gadolinium sesquioxide. The authors concluded that there is a great deal of similarity between the optical properties of the rare-earth glasses and rare-earth sesquioxide crystals. They postulated that Eu^{3+} is found in two, and possibly three environments (sites) in the glasses, which are synonymous to the three distinct sites for europium in the monoclinic form of europium sesquioxide [47]. Another important point in their work was the confirmation of temperature independent inhomogeneous broadening of the spectral lines. Rice and Deshazer [43] attribute the inhomogeneous broadening to the heterogeneity of the ion environment in glass. The heterogeneity of an ion environment can be described as a distribution of different environments about an 'average' environment. Spectral studies were performed on a neodynium doped glass [48] and similarities in the number of possible sites and in the splitting pattern to neodynium sesquioxide were observed.

Brecher and Riseberg [49,50] using fluorescence line narrowing (FLN) measurements, derived energy level assignments and crystal-field parameters for the Eu^{3+}

ion in a NaBaZn silicate glass. Employing even B^k_q values and by placing reasonable physical constraints such as packing densities, the authors developed a geometric model for the Eu^{3+} ion in both a highly modified silicate glass and in a fluoroberyllate glass. The model consists of eight oxygens, which are equidistant from the europium in a geometric arrangement of an elongated Archimedean antiprism. The inclusion of a ninth oxygen along the C_2 axis causes the structure to rearrange itself to accommodate the oxygen until all nine oxygens are equidistant from one another. This process is continuous and is described by a distortion parameter, which spans the limits set by the model. The crystal-field parameters, using a point charge model, were calculated with respect to the distortion parameter and compared to those derived from the measured splittings of the $^7F_1$ and $^7F_2$ manifolds obtained from the FLN experiment.

Brawer and Weber [51-55], using molecular dynamics and Monte-Carlo techniques, simulated Eu^{3+}-doped fluroberyllate glasses. Both simple BeF_2 glass and fluoroberyllate glasses with alkali and alkaline earth modifiers were analyzed. The simulations were carried out using a Born-Mayer-Huggins potential model which takes into account electrostatic interaction between atomic pairs. Results of the simulations revealed that the Eu^{3+} ions were coordinated by 6 and 7 F^- ions in BeF_2 and between 8 and 9 for the fluoroberyllate glasses. The local environments of the europium ion were found to have site to site variations and no local symmetry elements. In addition, simple BeF_2 glass was found to have greater structural variations than the alkali-modified BeF_2 glasses.

Brawer and Weber [51] used a point charge model to examine the range and distribution of energy-level splittings of the ground state energy level of the Eu^{3+} ion. Their model used a calculation which employs only second order crystal-field parameters, excluded J-mixing, treated only nearby ligands (within 2.75 Å) and only the $^7F_0$ and $^7F_1$ manifolds were considered. The range and distribution of the crystal-field energy levels for Eu^{3+} were in agreement with observations of both FLN and inhomogeneously-broadened spectra. Inhomogeneous linewidths and average energy splittings were predicted to be smaller in alkali-modified glasses than in BeF_2. The linewidth of the dopant was found to increase with increasing field strength of the cation modifier. Brawer and Weber [54] concluded that in order to predict the behavior of the average properties, summation over many sites was necessary to predict small changes in spectral properties.

Hirao and Soga [56] used molecular dynamics (MD) simulations to generate several Eu^{3+}-doped sodium borate glasses and employed the point charge model used by Weber and Brawer [51] to perform a crystal-field analysis of local environment of the Eu^{3+} ions. The primary aim of their study was to illustrate that with the appropriate pair potentials, Weber and Brawer's model could be applied to oxide glasses. The simulations were performed using a modified Born-Mayer-Huggins potential for all the atomic pairs. Results of the MD simulations revealed that the Eu^{3+} ions had an average coordination between 7.5 and 8.6 depending on the composition of the glass as well as large site to site variations in the europium local environment. In addition, a change in modifier concentration resulted in large variations of the inhomogeneous linewidth, which the authors attribute to the variation of the Eu-O and B-O interionic distances.

Cormier et al. [45] published a series of articles [57-59] on europium doped silicate and phosphate glasses. The authors employed molecular dynamics techniques to simulate the local structure of Eu^{3+} ions doped in amorphous silica (SiO_2:Eu^{3+}) and sodium disilicate glass(Na_2O•$2SiO_2$:Eu^{3+}). The corresponding optical absorption and emission spectra were simulated using a point-charge crystal-field model. Results of the MD simulation reveal a site to site variation in the local environments of the europium ion for both glasses. The authors report that the Eu^{3+} ions exist as quasimolecular complexes and have an average Eu-O coordination of 4 for SiO_2:Eu^{3+} and 6 for Na_2O•$2SiO_2$:Eu^{3+}. Moreover, the local structure of the Eu^{3+} ion was found to be more significantly influenced by "bonding and energetic requirements than by the topology of the silicate framework"[57]. In order to simulate the optical absorption and emission spectra of the Eu^{3+} ion, a full treatment, including J mixing, of the point-charge crystal-field method developed for doped crystalline materials was used. This method resulted in simulated spectra with correct energies and relative intensities, and a good agreement was obtained between the simulated and experimental spectra. An important development in their research was that the authors found no distinguishable correlations between the excitation energy and the coordination and average distances of the oxygen ligands surrounding the simulated Eu^{3+} ions [57]. Cormier et al. [57] concluded that the local environment of the europium ion is a continuous distribution of local fields which satisfy the energetic bonding requirements of the Eu^{3+} ions.

Chaussedent et al. [60-62] are the only group of researchers to have studied the hydration of Eu^{3+} using molecular dynamics techniques. The absorption and emission spectra were calculated using the point-charge crystal-field model employed by Cormier et

al. [57]. The europium ions were introduced into solution by the dissolution of a europium salt. The calculations were carried out using effective pair potentials to describe all interactions, and no parameterization of the ions or water molecules was performed. The Eu^{3+} ions were found to have an average of 8 water molecules in the first coordination shell arranged in a square antiprismatic geometry. Cormier et al. [57], in their simulation of the emission spectra of the Eu^{3+} doped glasses, were unable to properly reproduce the asymmetric peak shape of the electric dipole transitions. In order to rectify this problem, Chaussedent et al. [62] employed C_1 symmetry in their calculations instead of the C_{2v} symmetry used by Cormier et al. [57]. In addition, convolution of the spectra was performed by assigning a Lorentizian band shape; in contrast to the Gaussian band shape used by Cormier et al. [57]. The resulting spectra were in good agreement with those obtained experimentally and showed significant improvement to those generated by Cormier et al. [57] for Eu^{3+} in the silicate glasses.

1.2.1.2. Erbium

Er^{3+} has a ground state configuration of $[Xe]4f^{11}$ which is split by the Coulomb and spin orbit interactions into a number of multiplets. According to Hund's rule, the ground state is $^4I_{15/2}$ and the excited states are as follows: $^4I_{13/2,11/2,9/2}$, $^4F_{9/2,7/2,5/2,3/2}$, $^4S_{3/2}$, $^2H_{11/2,9/2}$ and so forth.

Numerous studies have been carried out on Er^{3+} due to the fact that it exhibits metastable intermediate levels which are readily accessible with red and near infrared radiation [24]. Moreover, the $^4I_{13/2} \rightarrow {}^4I_{15/2}$ transition of Er^{3+} ion at approximately 1.54 μm is of particular interest because of its applicability to telecommunications.

Renuka et al. [63] studied the optical properties of Er^{3+} ions in lithium borate glasses as well as performed a comparative energy level analysis of Er^{3+} ion in various glasses. The spectral characteristics of Er^{3+}:lithium borate glasses closely resembled the absorption of Er^{3+} ions in other systems (such as garnets, aquo-ion and phosphates). A slight variation, however, was reported in the relative positions and intensities of the bands due to variations in glass compositions between borate and other glasses. The authors also provide a detailed summary on the behavior of Er^{3+} ions with respect to changing environments. The electrostatic and spin-orbit interaction parameters were used to calculate the relative magnitudes of interactions experienced by Er^{3+} ions in various environments. Renuka et al. [63] also found that no systematic decreasing or increasing trends in the optical parameters were observed when the Er^{3+}:glass network is modified with alkaline earth ions with respect to either atomic weight and /or ionic radius of alkaline earths.

Reisfeld et al. [64] measured the absorption and emission spectra of Tm^{3+} and Er^{3+} in phosphate and borate glasses. Based on the inital studies by Rice and DeShazer [43,47] and subsequently by Reisfeld et al. [65], for europium in borosilicate glass, it was expected that a rare earth ion doped in a glass would occupy a symmetry site similar to that occupied in the corresponding sesquioxide. The authors proposed a model for Tm^{3+} and Er^{3+} in phosphate or borate glasses similar to that of Fournier and Bartram [66] for Yb^{3+} in glass. Each rare-earth ion would be coordinated by four MO_4 tetrahedra such that each of the coordinating tetrahedra contributes two non-bridging oxygens to the rare-earth ion. As a result, the eight-coordination of the rare earth ion by nonbridging oxygens was preserved and the average point symmetry of Tm^{3+} and Er^{3+} in the glasses would be

C_2. The inhomogeneous broadening due to the large number of sites was found to be larger than the broadening due to crystal-field splitting.

Robinson [67] using low temperature absorption or emission spectra postulated that the principle environment in Er^{3+}-doped alkali silicates is a sixfold distorted polyhedron. In a subsequent paper [68], Robinson postulates, based on spectral evidence, the existence of an additional three sites for Er^{3+} in binary alkali silicate glasses. In addition, models were proposed for two of the new sites based upon the spectral characteristics and compositional dependence. A summary of the results are as follows: Site A is the principal site and is present in all glasses regardless of the size of the alkali ion. In this site the Er^{3+} ion is sixfold coordinated in a near octahedral geometry. Site B occurs only in Li and Na binary silicate glasses and appears to be sixfold coordinated with Er^{3+} found at more than one edge of the SiO_4 tetrahedra. In contrast to site A, this site is sensitive to the size of the alkali ion and thus the spectrum associated with it does not appear for the larger alkali ions. Site C is present only in the K, Rb, and Cs silicate glasses. The identifiable peaks in the spectrum, with the exception of a band at 984 nm, are in good agreement with those for Er^{3+} in Er_2O_3, which suggests that this site may be similar to the C_2 site of Er^{3+} in Er_2O_3. Site D, was observed in K and Cs silicate glasses and is not expected to appear in Rb glasses. This site is postulated to be a variation of the B site whereby a smaller number of rare earth ions appear at the edges of the SiO_4 tetrahedra, thus resulting in a spectrum more similar to that of the A site.

Wolf et al. [69] used a combination of X-ray diffraction studies and molecular dynamics simulations to calculate crystal-field parameters for three different Na^+-Er^{3+} β"-alumina glass compositions (26, 72 and 100% of Na^+ were exchanged for Er^{3+} ions). The

authors postulated that Er^{3+} behaves differently in the β"-alumina matrix than other rare-earth ions studied. The behavior of Er^{3+} was attributed to its smaller radius in comparison to the other rare-earth ions studied as well as to the different Er^{3+} distributions in the conduction band. Analysis of the absorption spectrum of Na^{+}-Er^{3+} β"-alumina revealed that the intensities of the peaks were found to be independent of the Er^{3+} concentration and the spectral widths were 20-50% smaller. This could be due to the fact that the two Er^{3+} sites were found to be alike and thus the ions experienced similar crystal-fields. Using molecular dynamics, Wolf et al. [69] generated a number of configurations which were subsequently used in the point charge model to calculate the crystal-field parameters needed for the Judd Ofelt (JO) analysis of the optical spectra. The MD-based JO parameters were determined for different concentrations and temperatures and found to be in good agreement with experimentally obtained absorption intensities.

Employing EXAFS and photoluminescence techniques, Marcus and Polman [70] presented a brief study on the local structure of Er^{3+} ions doped or implanted in silicate and sodium silicate glasses. Their interpretation of the EXAFS results, following a qualitative study of model compounds, indicates that, in the sodium silicate sample, the Er^{3+} ions are surrounded by an average of 6.3 oxygens in the first coordination shell.

1.2.1.3. Ytterbium

$Yb3^{+}$ has a ground state configuration of $[Xe]4f^{13}$ with only one electron missing from the complete *4f* shell. The ground state level is $^{2}F_{7/2}$, which splits into four sublevels and a unique excited state level $^{2}F_{5/2}$, which splits into three sublevels, this occurs when the ion is in a low symmetry environment (C_{2v} or lower). Ytterbium is also

an ideal probe due to its relatively uncomplicated spectra.

Barber [71], from low temperature spectra of Yb^{3+} in quartz and sodium silicate glass, concluded that the rare-earth ion was surrounded by eight coordinating oxygens. The model was based on an arrangement of these eight oxygens atoms at the corners of a perfect cube with a Yb-O distance of 2.30 Å. The absorption spectra were found to show the full splitting for each manifold, and a highly symmetrical rhombohedral deformation was applied to the cube to lower its point symmetry from O_h to D_3. The crystal-field parameters were calculated using a distortion parameter, which was used to compute the absorption and emission spectra from the calculated energy splittings.

Robinson and Fournier [72,73] showed from the low temperature absorption and emission spectra of Yb^{3+} in phosphate, silicate and germanate glasses that the principal rare-earth site in these glasses is a sixfold coordination with near octahedral symmetry. The authors proposed that the Yb^{3+} ion is surrounded by three tetrahedra of the glass former ion, with each tetrahedra comprised of two oxygens which are adjacent to the Yb^{3+}. In this case, there would be six nearest oxygen neighbours to the ytterbium, thereby forming a site with D_3 symmetry. This site could also be described "as octahedral with a trigonal distortion caused by the necessity of displacing the tetrahedra in a radial direction away from the central rare-earth ion to provide space for this ion" [73].

1.2.1.4. Other rare-earth models

Mockovciak et al. [74], compared oscillator strengths calculated using a point charge model with values derived from the experimental absorption spectra of Nd^{3+}-doped silicate and borate glasses in an attempt to study the local environment of Nd^{3+}.

The models were chosen based on a neodynium sesquioxide and a neodynium ethylsulfate, since the coordination of the rare earth ions in the glass is similar to that in the corresponding crystalline compounds. Partial charges were used in order to reproduce more effectively the effect of non-bonding oxygens and only first neighbour oxygens were considered in the point charge model. However, in comparison to the experimental spectra, the authors found discrepancies in the oscillator strengths up to several orders of magnitude in their model, which they attributed to the presence of covalent bonding [74].

Lea et al. [75], tabulated numerical values of normalized eigenvectors and eigenvalues for cubic symmetry with no J-mixing, using the operator equivalent matrix elements tabulated by Stevens [76] and Elliott and Stevens [77]. The purpose of generating these tables and diagrams was to provide a method, which predicts spectroscopic energy level schemes and possible *g*-factors for rare-earth ions in cubic coordination.

Wolf et al. [78] simulated the polarized absorption spectra of Nd^{3+}-doped $Na^{+}B$"-alumina for five different neodynium concentrations. The crystal-field parameters were calculated based on molecular dynamics simulations of the Nd^{3+} doped glasses while oscillator strengths and Judd-Ofelt parameters were calculated using a point charge model at each time step in the simulation for each of the Nd^{3+} ions. The molecular dynamics simulations were performed using a modified Born-Mayer-Huggins potential for all atomic pairs. The simple point charge model yielded good qualitative and quantitative interpretations of the intensities of the absorption spectra for the Nd^{3+}-doped glasses. The authors attribute the success of their model to the following imposed criteria: (i) all possible environments experienced by the Nd^{3+} ions were taken into account, (ii) the

thermal motion of the ions in the conduction plane was included in the calculation, and (iii) the Ewald summation method was employed in the calculation of the $A_{t,p}$ parameters.

1.3 MOLECULAR DYNAMICS

One of the primary developments in both the physical and biological sciences during the last ten years has been the heightening ability of computer techniques to model the behavior of matter at the atomic level [79]. The field of computer simulations is developing towards an increasingly realistic and predictive description of complex systems; which are facilitated both by advances in computational techniques and by the continuing growth in computational power [79]. Significant advancements have been reported in the fields of molecular biology [79,80], polymer science [79,81], the physical chemistry of liquids [79,82], liquid crystals [79,83] and in the science of solid state materials [79,84].

Molecular dynamics (MD) is a computer based technique used to simulate the random constant motion of particles, at the microscopic level, from thermal excitation, and thus is able to describe and analyse dynamic processes in materials. Although the interionic forces used in the simulations are an oversimplification of the local quantum mechanical interactions, the motions of the atoms and/or molecules can still provide essential information of complex processes [85].

1.3.1. Interionic potentials - two versus three body interactions

Molecular dynamics simulations have shown that very simple pairwise additive interaction potentials reproduce many of the important structural features observed experimentally. Specifically, the short range repulsive part of the intermolecular potential

is the predominant factor in determining the short-range and to some extent the long-range order [86]. An effective method to test the results of a given pair potential, is to gradually augment the sophistication of the pair potential, and investigate features in the potential which give rise to specific observed effects. In most cases, simple spherical molecules can account for most of the bulk features. The fact that real intermolecular interactions are many-body interactions, exact agreement with experiment is often difficult to achieve and thus, a minimum of at least a three-body potential term is required to provide a more realistic treatment of a given material. Inclusions of many-body interactions into the potential function for MD simulations are often too computationally expensive. As a result, the pair potentials are often derived from experimental solid-state properties for which analytical expressions have been cast in terms of two-body potentials [86]. The pair potentials used in MD simulations are consequently termed "effective pair potentials", since only the average effects of many body forces are included.

Numerous simulations of oxide systems using two and three body intermolecular potential models are available in the literature [87]. The following section will review some of the more important studies relevant to this thesis, namely those which deal with silica and silicate systems and focus on the advantages and disadvantages of the potential model employed in the simulations.

1.3.1.1. Two-body potential models

Many new areas of investigation have evolved since the first reports of the MD technique in 1957 [88]. The first MD simulation of liquid fluoroberyllate was carried out by Rahman et al. [89] using a simple ionic model based on a spherical two-body Born-Mayer-Huggins potential. The simulation was able to successfully reproduce certain

structural features of vitreous BeF_2. Namely, the structure of the simulated BeF_2 glass consisted of BeF_4 tetrahedra joined at the corners with fluctuating Be-F-Be angles.

The first molecular dynamics simulation on silica was the pioneering work of Woodcock et al. [90]. Using a Born-Mayer-Huggins potential, the authors reported a four coordinated structure for silicon. An initial concern was the fact that the Si-O interaction is known to be covalent and employing an ionic potential was expected to result in large discrepancies. The authors demonstrated, however, that a simple electrostatic potential could accurately simulate a tetrahedral network structure. Furthermore, pair distribution functions derived from the simulations were found to be in good agreement with experimental X-ray diffraction data reported by Mozzi and Warren [21].

Soules [91] reported the first simulation of silicate glasses. A modified Born-Mayer Huggins two body potential was used in the simulations. The simulated glasses lacked short range order and as a result the structures generated by the simulations did not agree to a great extent with structural data obtained from experimental techniques.

Improvements on the simulated structure were made by Mitra et al. [92-94] by using a two body model with Coulombic interactions and a power-law repulsion term. The MD simulation parameters in the potential function were varied in order to obtain the correct glass structure at room temperature. The authors found that based on the potential energy function, the energy scale of the simulation was proportional to the square of the charges and the simulation results could be scaled for changes in temperature by varying the charges. The charges were chosen to yield a glass transition temperature lying within the experimental range of 1200-1800K. The radial distribution functions for the simulation were found to be in good agreement with experimental X-ray diffraction

data [21] with respect to peak position and coordination number but differences were found in the peak heights.

The main criticism of the above two-body potential models is the fact that the partial covalency present in the Si-O bond is not taken into account. As a result, more complex potentials have been developed to represent three-body interactions and a selected few are discussed in the next section.

1.3.1.2. Three-body potential models

It is well known that the partial covalency of the Si-O bonds introduces a bond directionality, which is closely related to the short range order in the silica/silicate structure.

Feuston et al. [95] introduced a three-body interaction term similar to that developed by Stillinger and Weber [96]. The authors found that by forcing the O-Si-O and Si-O-Si angle terms to 109.471°, the oxygen-oxygen pair distribution function was significantly narrowed while the Si-O-Si bond angle distribution was slightly broadened and shifted to smaller angles, in accordance with experimental results. As observed in the structure of ice, oxygen exhibits a tendency toward tetrahedral coordination due to the presence of the two electron lone pairs and to compensate for this, $\theta_{Si\text{-}O\text{-}Si}$ was set to 109.471° [95]. In addition, improvements to the short range order were reported by the elimination of the O-Si-O bond angle peak at 105° which was attributed to five-coordinated silicon ions.

Newell et al. [97] employed the three-body potential model developed by Feuston et al. [95] to investigate the structure of a sodium trisilicate glass. The structure

of the glass was analyzed and the results were compared to those found using two body potentials as well as to experimental results found using X-ray diffraction, XPS, NMR and EXAFS. The simulated glass showed vast improvements over the two body potential models and reported bulk structural features, which were in excellent agreement with experimental data. The overall structure closely resembled the modified network structure of glass proposed experimentally, with the silicon tetrahedra forming the backbone structure and sodium ions breaking up the network through the creation of nonbridging oxygens. Since this potential was so successful in describing the structure of sodium trisilicate, it was also used as the model to simulate the lead silicate glasses investigated in this thesis.

Vashista et al. [98] used a combination two/three body potential to simulate the crystalline forms of silica in the melt. The two-body contribution consisted of three terms, steric repulsion due to ionic sizes, Coulombic interactions to account for charge transfer and charge-dipole interaction to include the effect of electronic polarizability. The three body covalent contributions included O-Si-O and Si-O-Si angle dependent interactions, which are a function of the Si-O interionic distance. Bulk structural features of the simulation were found to be in very good agreement with neutron diffraction and NMR data.

The simulation of silicate glass was also performed by Vessel et al. [99] using a combination two/three body potential model. The two-body contribution to the potential consists of a long range Coulombic interactions while the Si-O short range interactions were modelled using a four range Buckingham potential. The O-O short range interactions were modelled using an *ab initio* potential derived by Pyper [99,100]. The three body interactions between the O-Si-O and Si-O-Si triads are modelled using angle

constraints of 109.28° and 144°, respectively. The structure obtained from the simulation did not agree well with experimentally determined structural features of silica glass, but rather appeared to have structural characteristics of high pressure silica glass. The authors concluded that the potential would probably be very useful for high pressure studies of vitreous silica.

Since it is impossible to discuss all of the available potential models and simulations performed, the reader is referred to several excellent review articles [101,102] in the literature which provide more detailed information on the simulations of silicates and other systems.

1.4 STATEMENT OF THE PROBLEM

The driving force behind the work in this thesis was to be able to use computer generated glasses to predict the optical spectra of rare-earth doped inorganic glasses. In order to achieve this, a model, which accurately represents the structure of these glasses and more importantly, the environment of the rare-earth ions, would have to be developed.

The starting point of this research was to obtain a better understanding of the structure of the undoped lead silicate glass using molecular dynamics simulations with a two-body (2-body) potential model and a combination two- and three-body (2/3-body) potential model. The parameters in the two-body potential model had been developed in a previous study [41] and thus did not require any modifications. The simulated glasses were compared to experimental EXAFS and XRD data of crystalline lead silicate in order to parameterize the combination two- and three-body potential model. EXAFS provide bond lengths and nearest neighbour coordination data, which can be used to alter the

potential energy function used in the MD simulation such that an appropriate effective potential can be generated. Bulk structural features of simulated glasses generated from the 2-body and 2/3-body are compared to experimental XRD, Neutron and NMR data in order to determine the validity of the potential function. Also a comparison between the two and two/three body potential models was made in order to determine the appropriate model for simulating lead silicate glasses.

A composition study was also performed on the undoped lead silicate glass. Namely, glasses of 22/78mol% $PbO{\bullet}SiO_2$, 50/50mol% $PbO{\bullet}SiO_2$, and 70/30mol% $PbO{\bullet}SiO_2$ were simulated using molecular dynamics techniques with a 2/3-body potential model. There are several reasons for simulating lead silicate glasses of different concentration. Firstly, information on the effect of PbO on the SiO_2 network at varying concentrations of PbO is provided. This is important since it may aid spectroscopists in interpreting and predicting the optical properties of such glasses. Secondly, it has been postulated that high lead glasses may possess spectral properties that may lead to an increase in the absorption cross-section of the glass. The crystal structure of these lead silicate glasses is known and some experimental data was available. A good agreement between the real and simulated glasses would reinforce the validity of the potential model.

Once a clear description of the base glass was attained, three different rare-earth doped glasses, $PbO{\bullet}SiO_2{:}Eu^{3+}$, $PbO{\bullet}SiO_2{:}Er^{3+}$ and $PbO{\bullet}SiO_2{:}Yb^{3+}$ were simulated using molecular dynamics and the 2/3 body potential model. The parameters for the rare-earth ion were developed using, whenever possible, experimental EXAFS and XRD data. A detailed investigation on the local environment of these rare-earth ions was performed. A concentration study on the Er^{3+} doped lead silicate glasses was also performed in order to

investigate erbium-erbium clustering. It has been shown experimentally that high concentrations of Er^{3+} ions (10% Er^{3+}) result in concentration quenching.

The trivalent rare-earth ions are attractive to probe the optical properties of materials since the crystal-field splitting varies from host to host, thus reflecting the different symmetries and strengths of the different local environments.

The Eu^{3+} ion has a relatively simple energy level structure whereby both the ground state($^7F_0$) and the excited state($^5D_0$) are non-degenerate and thus simpler to analyze. Moreover, since there is no splitting of these levels due to the crystal-field, any observed splitting or inhomogeneous broadening results from dissimilar Eu^{3+} bonding environments [103] making europium an ideal probe for crystal-field analysis for both crystalline and vitreous materials.

Er^{3+} is an ideal ion since it emits in the visible and absorbs in the near infrared around 800 and 980 nm, both excellent diode-laser wavelengths. Er^{3+} also lases at 1.55 μm and substantial room-temperature upconversion from infrared to visible radiation has been observed in lead silicate glasses [24].

The main reason for studying the Yb^{3+} ion is the beneficial influence it has on the upconversion efficiency in a Er^{3+}/Yb^{3+} co-doped lead silicate system. Moreover, Yb^{3+} has an excellent absorption co-efficient while Er^{3+} has a good emission co-efficient thus providing an ideal medium for investigating the energy transfer phenomenon.

In order to generate the electronic spectra of these glasses, a point-charge crystal-field model was used to calculate the electronic energy levels and transition probabilities. The experimental emission spectrum of the Eu^{3+}- and Er^{3+}-doped lead silicate glasses was also determined. Assuming a reasonable agreement exists between the

spectral features of these simulated glasses and the real glasses, it can be concluded that the simulated models are a valid representation of the real structure. This is a very powerful tool since the simulated structure reveals information on the local environments of these rare-earth ions. This allows for the direct study and isolation of individual environments, which could be responsible for specific spectral features found in the absorption and emission spectra of these rare-earth doped glasses.

CHAPTER 2

2.0 MOLECULAR DYNAMICS

2.1 COMPUTATIONAL PROCEDURE

Molecular dynamics (MD) is a computer simulation technique that can be used to model structural representations at the atomic level and calculate average structural, thermodynamic and transport properties of a given glass. For a system containing N particles, MD computations are accomplished by direct numerical integration of the Newtonian equations of motion. A MD calculation begins with an initial arbitrary set of positions and momenta for a small representative number of atoms and solves the equations of motion such that the atomic trajectories are determined as a function of time [104]. In general, simulations are conducted from picoseconds to nanosecond time periods.

For a system of N particles in three dimensions, there are 3N coupled second order partial differential equations that must be solved numerically by using finite difference methods [85]. Since calculation speed is very important, the number of available numerical algorithms is limited. Two methods most commonly used are the Verlet algorithm and the Predictor-Corrector method, both of which calculate the positions and velocities of the ensemble of particles at fixed time intervals.

The N ions are simulated within a box, the volume determined by the pre-described density, which contains periodic boundary conditions, hence eliminating surface effects associated with very small systems. Each ion in the central box has images of itself at all combinations of unit translations by the box along its edges. If during the course of a MD simulation, an ion moves out of the central box, a corresponding image moves into

the box at the opposite face [104]. There are no walls at the boundaries of the central box nor any surface molecules. The purpose of creating such a box is simply to serve as a convenient axis system for determining the coordinates of the N molecules [82].

The stability of the system is verified by performing runs of several thousand timesteps and calculating the total energy fluctuation and the temperature variation. The total energy is the sum of the kinetic energies of all the particles and the potential energies calculated from the force function selected [85]. The temperature is calculated from the kinetic gas theory as follows:

$$\frac{3}{2}NkT = \sum_i \left[\frac{1}{2} m_i v_i^2\right] \qquad 2.1.1.$$

The initial conditions are prescribed at high temperatures, in order to allow a rapid equilibration of the initial system. Either a constant volume or a constant pressure is assumed in cooling to the solid phase [85]. All MD simulations performed in this thesis assume constant volume conditions, such that the Hamiltonian is the sum of the kinetic energy and the potential energy of the system. The final temperature is reached by lowering the temperature of the system in steps of a few hundred degrees Kelvin at a time while adjusting the volume of the system to yield the desired density, then allowing the system to thermodynamically equilibrate at each state. Thus, the sequence of configurations generated during the MD simulation corresponds to a finite ensemble of micro-resonance structures in terms of statistical thermodynamics. Since the positions and velocities of all particles are known throughout the quench procedure, thermodynamic, structural, transport and mechanical properties of the system may be calculated.

2.2 INTERIONIC POTENTIAL MODELS

The predictive ability of a MD simulation is only as accurate as the applied potential energy function. The following sections will review the potential models chosen for the simulations performed in this thesis.

2.2.1. Two-body potential model

The two body interionic potential used in the present calculations was developed by Mitra et al. [92-94] for silica and sodium silicate systems. The associated interionic potential contains a steep repulsive part as well as a Coulombic attractive potential and can be described by the following expression:

$$V(r_{ij}) = \frac{q_i q_j e^2}{4\pi\varepsilon_0}\frac{1}{r_{ij}}\left[1 + sign(q_i q_j)\frac{(\sigma_i+\sigma_j)^n}{n+1}\frac{1}{r_{ij}^n}\right] \qquad 2.2.1.1.$$

The force law derived from the pairwise (two-body) ionic potential, which includes Pauling repulsive term is found to be:

$$F(r_{ij}) = \frac{q_i q_j e^2}{4\pi\varepsilon_0}\frac{1}{r_{ij}^2}\left[1 + sign(q_i q_j)\left(\frac{\sigma_i+\sigma_j}{r_{ij}}\right)^n\right] \qquad 2.2.1.2.$$

where q_i and q_j are the ionic charges, σ_i and σ_j are the ionic radii of the atoms i and j, r_{ij} is the distance between atoms i and j, and n is a parameter representing the hardness of the

repulsive part of the atomic pair interaction. The *sign* function returns a value of +1 or -1 depending on the sign of the operand (q_iq_j). The values for the charges, radii and n were previously developed by Mitra et al. [93,94] for silica and sodium silicate. The aforementioned potential was also used previously to investigate various oxide-base glasses, both undoped and doped with trivalent rare-earth ions with much success [45,57,105].

Over a certain separation distance, all force functions eventually become negligible and thus only those particles within a specific range from each particle should be considered [85]. The instantaneous force, for solving the Newtonian equations of motion, was determined for each ion over the set of atomic neighbours within a sphere of 5.5 Å using a screened Coulombic force. The benefit of a truncated force function is that by limiting the number of particles with which an atom interacts, the computational time is greatly reduced. The length of 5.5 Å is large enough to include neighbours of importance (approximately 700 atoms) and small enough to avoid the formation of odd coordinated defects. In order to ensure that there is no discontinuity at r_c = 5.5 Å, the force is decreased monotomically by the following scaling factor:

$$F'(r_{ij}) = F(r_{ij}) \cdot \left[1 - \left(\frac{r_{ij}}{r_c}\right)^3\right] \qquad 2.2.1.3.$$

Once the instantaneous force on each atom *i* was computed, the computer updated the configuration at each timestep (Δt = 1.0fs). The general objective of the simulation is to maximize the yield of molecular dynamics in real time relative to that of machine time

within acceptable limits for conservation of energy and momentum. Whereas increasing Δt would enhance the former, additional cycles in the algorithm would increase the computational time per time increment. Verlet [106] noted that since the repulsive forces between colliding molecules are steep, it was necessary to have a small value of Δt, and therefore introduced a simple finite-difference formula for the second order derivative of his algorithm.

The Verlet algorithm is one of the most popular methods for calculating particle trajectories [85]. The algorithm uses a combination of Taylor series expansions to calculate the position of the particle in terms of its two previous position according to the following equation:

$$x(t+\Delta t)=2x(t)-x(t-\Delta t)+\left[\frac{d^2x(t)}{dt^2}\right](\Delta t)^2+0[(\Delta t)]^4 \qquad 2.2.1.4.$$

The local truncation error varies as $(\Delta t)^4$, and is third order although there is no third order derivative term [107]. The velocity is commonly calculated for the middle of the interval (at the half-step) as follows:

$$v\left(t+\frac{\Delta t}{2}\right)=\frac{x(t+\Delta t)-x(t)}{\Delta t} \qquad 2.2.1.5.$$

or

$$v(t)=\frac{x(t+\Delta t)-x(t-\Delta t)}{2\Delta t} \qquad 2.2.1.6.$$

The Verlet algorithm is simple and stable for moderately large time steps, and requires only three vectors per particle.

2.2.2. Combination two- and three-body potential model

The MD calculations were performed using a three-body potential in order to take into account the partial covalency of the Si-O and Pb-O bonds. The multibody potential used was developed by Feuston et al. [95]. The two-body potential term, which governs the interaction between ion pairs, consists of a modified form of the Born-Mayer-Huggins (BMH) ionic potential and is of the form:

$$V_2 = A_{ij}\exp\left(-\frac{r_{ij}}{\rho}\right) + \frac{Z_i Z_j e^2}{r_{ij}} erfc\left(\frac{r_{ij}}{\beta_{ij}}\right) \qquad 2.2.2.1.$$

where A_{ij} is the short range coefficient for repulsion used to determine interionic distances, β_{ij} and ρ_{ij} are constants for the different ion pairs and are adjustable parameters, r_{ij} is the distance between ions i and j and Z is the formal ionic charge of the ions.

The three-body potential energy term is:

$$V_3(r_{ij}, r_{ik}, \theta_{ijk}) = \left[\lambda_i \exp\left(\frac{\gamma_i}{r_{ij} - r_i^c} + \frac{\gamma_i}{r_{ik} - r_i^c}\right)\left(\cos\theta_{jik} - \cos\theta_{jik}^c\right)^2\right]$$

$$\text{if } r_{ij} < r_i^c \text{ or } r_{ik} < r_i^c \qquad 2.2.2.2a.$$

and

$$V_3(r_{ij}, r_{ik}, \theta_{ijk}) = 0, \quad \text{if } r_{ij} \geq r_i^c \text{ or } r_{ik} \geq r_i^c \qquad \text{2.2.2.2b.}$$

where i is the central atom with covalent near neighbours j and k and λ_i, γ_i, r^c_i, and θ^o_{jik} are constants and θ_{jik} is the angle subtended by r_{ij} and r_{ik} with the vertex at i. To allow for differences in the local order of the bonding configurations under consideration, O-Si-O, Si-O-Si, O-Pb-O and Pb-O-Pb, the following conditions must be met, $\gamma_{Si} \neq \gamma_O$, $\gamma_{Pb} \neq \gamma_O$, and $r^c_{Si} \neq r^c_O$, $r^c_{Pb} \neq r^c_O$. The three-body potential decreases the total binding energy of the system whenever the bond angle θ_{jik} differs from the preferred angle θ^c_{jik}. In order to impose a tetrahedral geometry about the silicon ions, $\theta^c_{O\text{-}Si\text{-}O}$ is set equal to the tetrahedral angle of 109.471° and $\cos\theta^c_{O\text{-}Si\text{-}O} = -1/3$ [95]. In ice, oxygen has a tendency toward tetrahedral coordination, due to the presence of its two electronic lone pairs. To account for this, Feuston et al. [95] also set $\theta^c_{Si\text{-}O\text{-}Si}$ equal 109.471°. The differences in the three-body interactions of the O-Si-O and Si-O-Si bonding contributions are attributed to the values of λ_{Si}, λ_O, γ_{Si}, γ_O, r^c_{Si} and r^c_O. Since the tendency toward tetrahedral coordination is much lower for oxygen than for silicon in v-SiO_2, λ_O was defined to be much less than λ_{Si}.

The interactions between Pb-O and RE-O were described by using an additional 12-8 Lennard-Jones pair potential interaction term:

$$VLJ_{ij} = 4\varepsilon\left[\left(\frac{\sigma_{ij}}{r_{ij}}\right)^{12} - \left(\frac{\sigma_{ij}}{r_{ij}}\right)^{8}\right] \qquad \text{2.2.2.3.}$$

where ε is the depth of the potential well between the two ions, σ_{ij} is the ionic radius and r_{ij} is the separation between the two ions.

Integration of the Newtonian equations of motion for an N-particle ensemble was accomplished by using a fifth order Nordsieck-Gear predictor corrector algorithm with a timestep of 1.0fs. The Predictor-Corrector methods used a variety of higher order derivatives to calculate the Taylor series approximations for the particle positions and their derivatives. The particle positions and velocities are corrected by the use of corrector expressions associated with the specific predictor chosen.

Nordsieck's method [108] for Newton's equation describes the integration of five time derivatives of the position vector according to the following equations:

$$r_1(t) = (d\,r_0/dt)(\Delta t) \qquad \text{2.2.2.4a.}$$

$$r_2(t) = (1/2)(d^2 r_0/dt^2)(\Delta t)^2 \qquad \text{2.2.2.4b.}$$

$$r_3(t) = (1/6)(d^3 r_0/dt^3)(\Delta t)^3 \qquad \text{2.2.2.4c.}$$

$$r_4(t) = (1/24)(d^4 r_0/dt^4)(\Delta t)^4 \qquad \text{2.2.2.4d.}$$

$$r_5(t) = (1/120)(d^5 r_0/dt^5)(\Delta t)^5 \qquad \text{2.2.2.4e.}$$

The predicted values for the r_n at some time $(t+\Delta t)$ are obtained through a Taylor series expansion:

$$r_0(t+\Delta t)=r_0(t)+r_1(t)+r_2(t)+r_3(t)+r_4(t)+r_5(t) \quad \text{2.2.2.5a.}$$

$$r_1(t+\Delta t)=r_1(t)+2r_2(t)+3r_3(t)+4r_4(t)+5r_5(t) \quad \text{2.2.2.5b.}$$

$$r_2(t+\Delta t)=r_2(t)+3r_3(t)+6r_4(t)+10r_5(t) \quad \text{2.2.2.5c.}$$

$$r_3(t+\Delta t)=r_3(t)+4r_4(t)+10r_5(t) \quad \text{2.2.2.5d.}$$

$$r_4(t+\Delta t)=r_4(t)+5r_5(t) \quad \text{2.2.2.5e.}$$

$$r_5(t+\Delta t)=r_5(t) \quad \text{2.2.2.5f.}$$

The displacement vectors are calculated according to the following relationship:

$$x(t)=\left[\frac{1}{2}\frac{F_i}{m_i}\Delta t^2-r_2(t+\Delta t)\right] \quad \text{2.2.2.6.}$$

where r_2 is the second derivative of the position vector r as described by the Taylor expansion series [108]. The corrected values of r_n are then evaluated using the following corrector scheme, and the new displacement vectors are calculated using the six constants ($c_0..c_5$) described by Nordsieck.

$$r_0^c(t+\Delta t)=r_0(t+\Delta t)+c_0 \quad \text{2.2.2.7a.}$$

$$r_1^c(t+\Delta t)=r_1(t+\Delta t)+c_1 \quad \text{2.2.2.7b.}$$

$$r_2^c(t+\Delta t)=r_2(t+\Delta t)+c_2 \quad \text{2.2.2.7c.}$$

$$r_3^c(t+\Delta t)=r_3(t+\Delta t)+c_3 \quad \text{2.2.2.7d.}$$

$$r_4^c(t+\Delta t) = r_4(t+\Delta t) + c_4 \qquad 2.2.2.7e.$$

$$r_5^c(t+\Delta t) = r_5(t+\Delta t) + c_5 \qquad 2.2.2.7f.$$

where c_0=3/16, c_1=251/360, c_2=1, c_3=11/18, c_4=1/6 and c_5=1/60.

It is important to note that these constants are only valid for fifth order methods. The Predictor-Corrector method is more accurate than the Verlet algorithm, but usually requires the storage of six or more vectors per particle.

2.3 DATA ANALYSIS METHODS

2.3.1. Pair and cumulative distribution functions

The pair distribution function (PDF), $g_{ij}(r)$, is a measure of the local structure of atomic pairs and is proportional to the probability of finding two atoms separated by a distance, $r \pm \Delta r$. Since molecular dynamics simulations provide time-averaged positions of individual atoms, the PDF can be calculated directly from the atomic trajectories according to the following equation [107]:

$$g_{ij}(r) = \frac{1}{4\pi \rho_j r^2} \frac{d\langle N_{ij}(r) \rangle}{dr} \qquad 2.3.1.1$$

where $N_{ij}(r)$ is the number of atoms of type j inside a sphere of radius (r) around a selected atom of type i, ρ_j is the bulk density of the atoms of type j and $d\langle N_{ij}(r) \rangle$ is the number of atom type j found in thin spherical shells of radii of (r) and (r+dr) around atom type i. An average value of $g_{ij}(r)$ is ensured by performing the calculation over thousands

of timesteps [9].

The cumulative distribution function (CDF) is defined as the average number of atoms of type j surrounding an atom of type i in a sphere of radius r and can be calculated by integrating the PDF to a distance r_0 as follows:

$$C_{ij}(r) = 4\pi \rho_j \int_0^{r_o} g_{ij}(r) r^2 dr \qquad 2.3.1.2.$$

2.3.2. Bond angle distribution function

The distribution of bond angles can be defined as follows:

$$a_{ikj}(r_{ij}, \theta) = \frac{1}{n_o 2\pi^2 \sin\theta} \frac{d\langle n(r_{ij}, \theta)\rangle}{dr_{ij} d\theta} \qquad 2.3.2.1.$$

where $a_{ikj}(r_{ij},\theta)$ is the probability of finding a third ion k in a volume element $2\pi^2 \sin\theta dr_{ij} d\theta$, r_{ij} is the distance between atoms i and j and the angle, θ, between three adjacent atoms, *i*, *j* and *k*, can be defined by the following equation:

$$\cos\theta = \frac{\vec{r}_{ik} \cdot \vec{r}_{jk}}{\left|\vec{r}_{ik}\right| \left|\vec{r}_{jk}\right|} \qquad 2.3.2.2.$$

where $\vec{r}_{ik}$ and $\vec{r}_{jk}$ are the directionality vectors between atom k and two of its neighbours i and j [45]. Figure 2.3.2.1. is a schematic representation of the angle, θ_{ikj}.

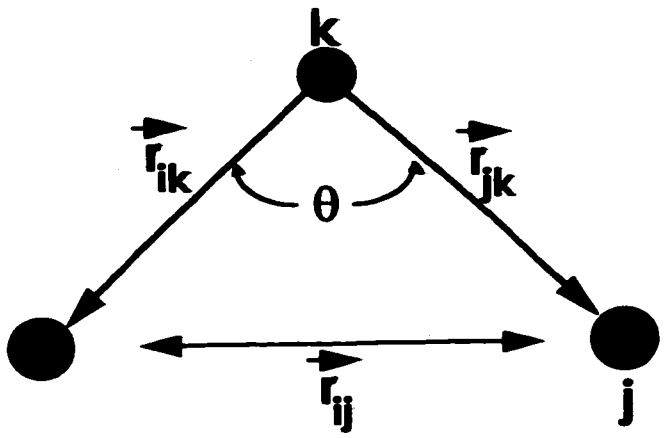

Figure 2.3.2.1. Angular arrangement of atoms i, k and j with directionality vectors $\vec{r}_{ik}$ and $\vec{r}_{jk}$ [45].

2.3.3. Computer graphics

The computer graphics were generated using a software program, *placenewest*, developed by the Interfacial Surface Science Laboratory at Rutgers University, NJ. The software reads the atomic configurations saved throughout the MD simulation using proper box lengths and periodic boundary conditions. The atom sizes and bond cutoff distances are entered manually to the data file. This technique allows for the representation of the glass structure as well as calculates distances, coordination and bond-angles between atom pairs. The software is mouse driven thus for any given configuration individual atoms or atom sets can be isolated and analyzed.

CHAPTER 3

3.0 CRYSTAL-FIELD THEORY

The fundamental objectives of crystal-field theory are to determine the modifications to the electronic properties of an optically active ion due to the presence of a crystal-field. The crystal-field is considered to be external to the ion and possesses a definite symmetry. Using group theory and the appropriate symmetry of the ion, it is possible to predict the splitting of the energy levels and the eigenfunctions representing the states.

The first theoretical considerations of the crystal-field theory were introduced by Bethe [109] using a point charge model, and has since been expanded and refined to include the effects of bonding and the presence of intrinsic excitations by the surrounding medium [1]. In this section, the most pertinent aspects of the crystal-field theory pertaining to the thesis will be reviewed and for a more in-depth investigation, the reader is referred to various sources on the subject [110-112].

3.1 THE RARE-EARTH IONS

The rare-earth ions (RE) in solids are either divalent or trivalent and can have partially filled $4f$ electron shells that are shielded from external fields by the $5s$ and $5p$ electronic shells. The $4f$ electrons are only weakly perturbed by the surrounding ligands and behave as inner electrons. As a result, the optical spectra of rare-earth ions doped in solid state materials consist of a series of very sharp lines that closely resemble the free-ion spectra. The nature of the wave function of the free ion, prior to its introduction into the host material, is only known to some approximate extent [1]. In an ionic medium, the

electrons occupy orbitals that are highly localized about the ions such that any electron can still be associated with a particular ion, and each electron will still feel the repulsion from the electrons of the other ions and an attraction to their nuclei. The degree of perturbation produced on the optically active electrons by the static electric fields of these neighbouring ions depends on the nature of the electrons themselves. The result of the perturbations is the shifting of energy levels, removal of degeneracies and alteration of radiative transition probabilities.

There are three main interactions that control the properties of the *f*-electrons of a rare-earth ion doped in a solid, the electrostatic interaction between electrons, the spin-orbit interaction and the crystal-field [110]. The inter-electronic Coulomb interaction leads to an initial splitting of states and to the formation of LS terms (orbit and spin angular momenta, respectively). Spin-orbit coupling causes the electronic terms to be perturbed and the LS terms split further into J-multiplets. The multiplets are denoted using the Russell-Saunders terminology, $^{2S+1}L_J$. Thus, the matrix causes the free-ion electronic levels to split into a series of multiplets, with the center of gravity of each of these multiplets located within a few hundred wavenumbers of the free-ion levels.

Trivalent rare-earth ions have immense scientific appeal due to the fact that the spectral characteristics of these ions are strongly host dependent [110], and the crystal-field splitting will vary from host to host, reflecting the different symmetries and strengths of different local environments. The rare-earth ions of interest in this study are trivalent europium, erbium, which will be investigated in great detail, and trivalent ytterbium.

3.1.1. Europium

Trivalent europium (atomic number 63) has a ground state electronic configuration [Xe]$4f^6$ ($1s^2 2s^2 2p^6 3s^2 3p^6 3d^{10} 4s^2 4p^6 4d^{10} 5s^2 5p^6 4f^6$) and is split by the Coulomb and spin orbit interactions into a number of multiplets. Figure 3.1.1.1. shows the energy level diagram of Eu^{3+} with effects caused by the different Hamiltonians. As mentioned previously, Eu^{3+} has a relatively simple energy level structure with a non-degenerate ground state ($^7F_0$) and a non-degenerate emitting level ($^5D_0$). The absorption and emission from the singlet (J=0) levels of Eu^{3+} facilitate the study of linewidths and positions without the complications of overlapping lines [43], which makes it an ideal probe for crystal-field analysis for both crystalline and vitreous materials.

3.1.2. Erbium

Atomic number 68 represents trivalent erbium which has a ground electron state electronic configuration [Xe]$4f^{11}$ ($1s^2 2s^2 2p^6 3s^2 3p^6 3d^{10} 4s^2 4p^6 4d^{10} 5s^2 5p^6 4f^{11}$). Figure 3.1.2.1. shows the multiplet structure of the Er^{3+} ion split by Coulomb and spin-orbit interactions. Er^{3+} is one of the most popular rare-earth ions since its laser oscillation at 1.55 μm is utilized as a fiber amplifier in doped silica. Moreover, it exhibits three fluorescences, blue, green and red, in the visible region as well as green-upconversion emission at 0.5 μm, which has been observed in oxide glasses by infrared III-V diode laser pumping [113].

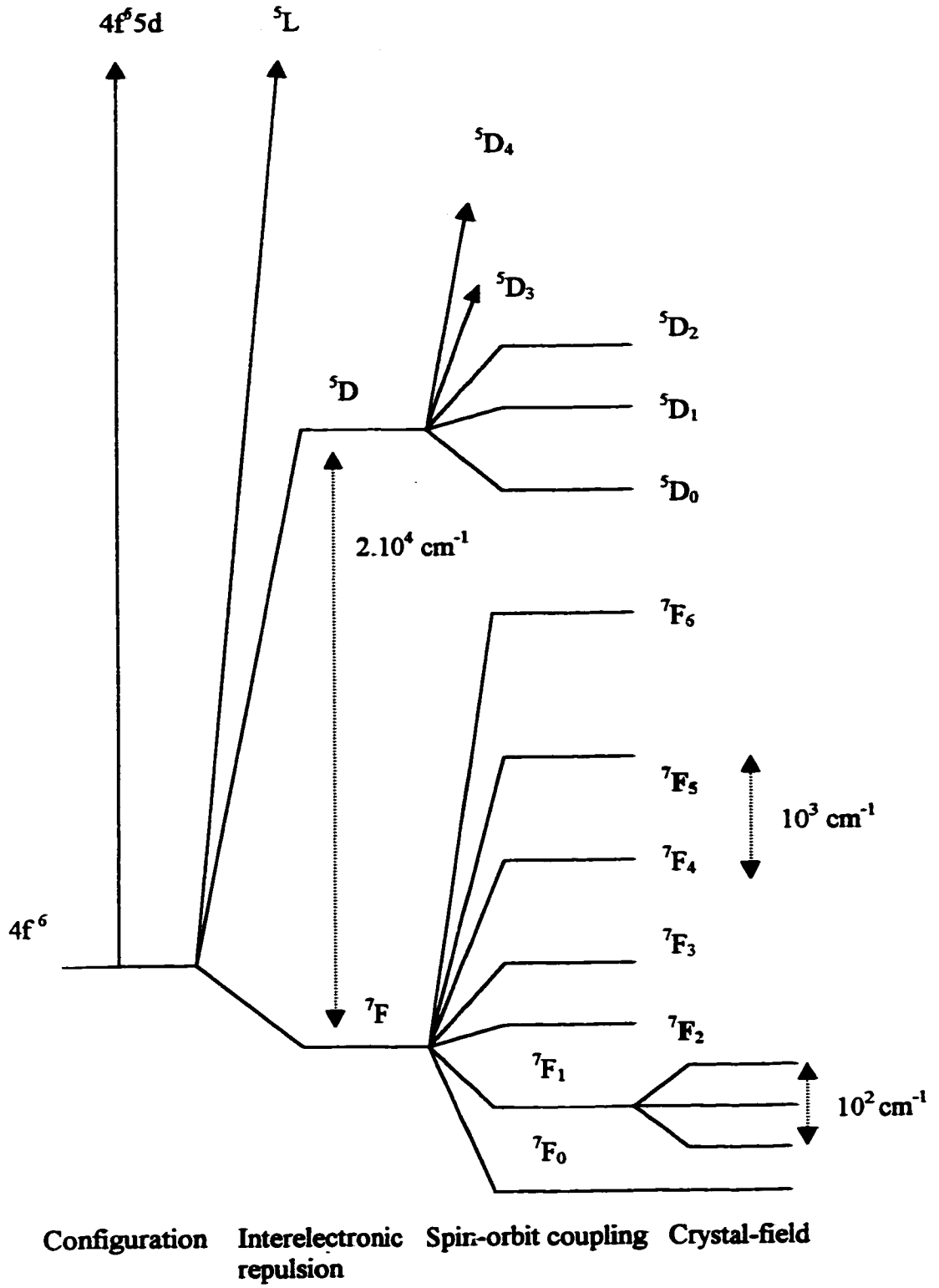

Figure 3.1.1.1. Energy level diagram for the Eu^{3+} ion.

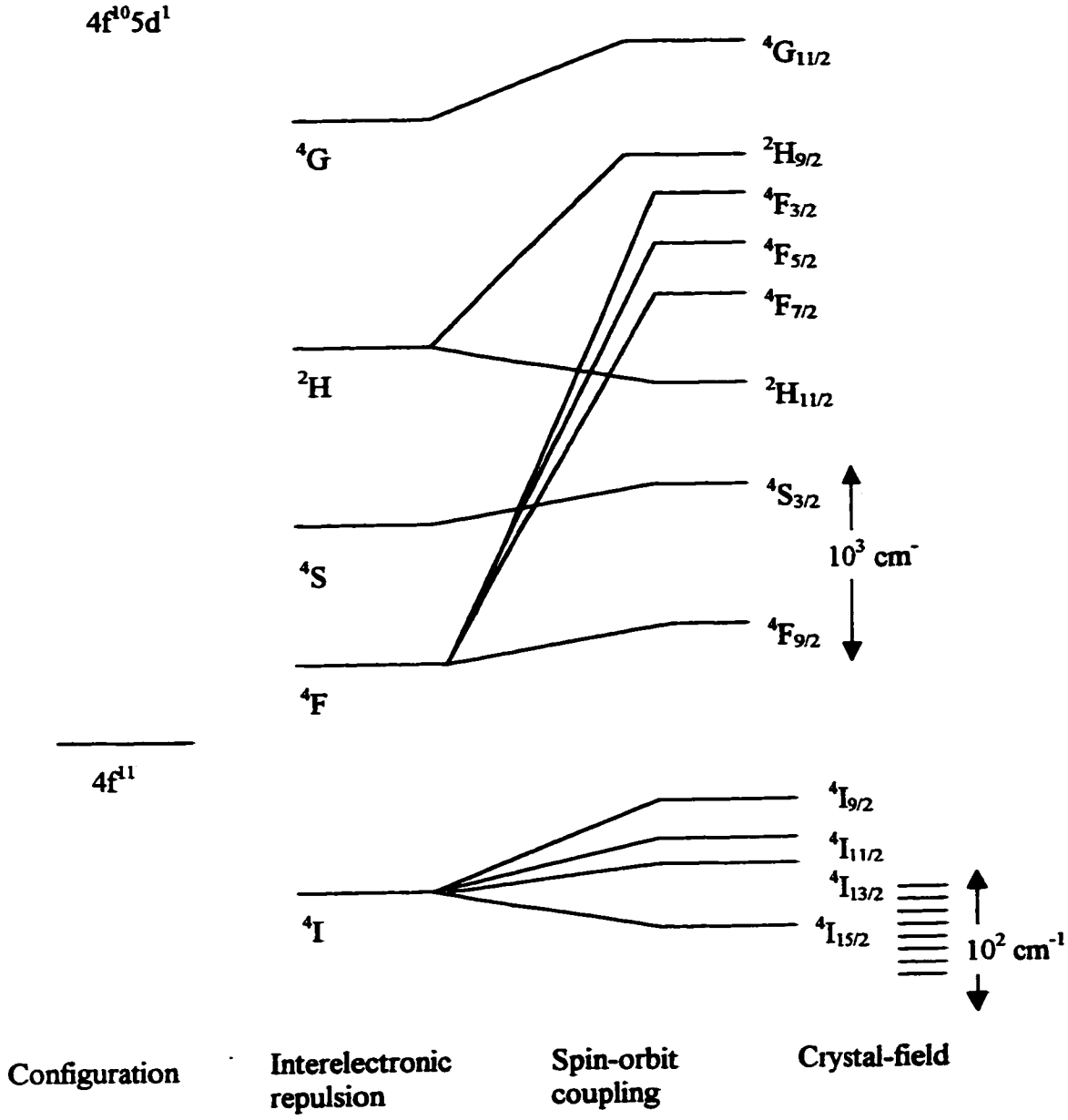

Figure 3.1.2.1. Energy level diagram of the Er^{3+} ion.

3.1.3. Ytterbium

The ground state electronic configuration of trivalent ytterbium, atomic number 70, is [Xe]$4f^{13}$ ($1s^2 2s^2 2p^6 3s^2 3p^6 3d^{10} 4s^2 4p^6 4d^{10} 5s^2 5p^6 4f^{13}$). The $4f^{13}$ ground state configuration of Yb^{3+} gives rise to $^2F_{7/2}$ (lowest level) and $^2F_{5/2}$ levels that are separated by 10 500 cm^{-1} [66]. Figure 3.1.3.1. shows the J-levels that are split through interaction with the crystal-field.

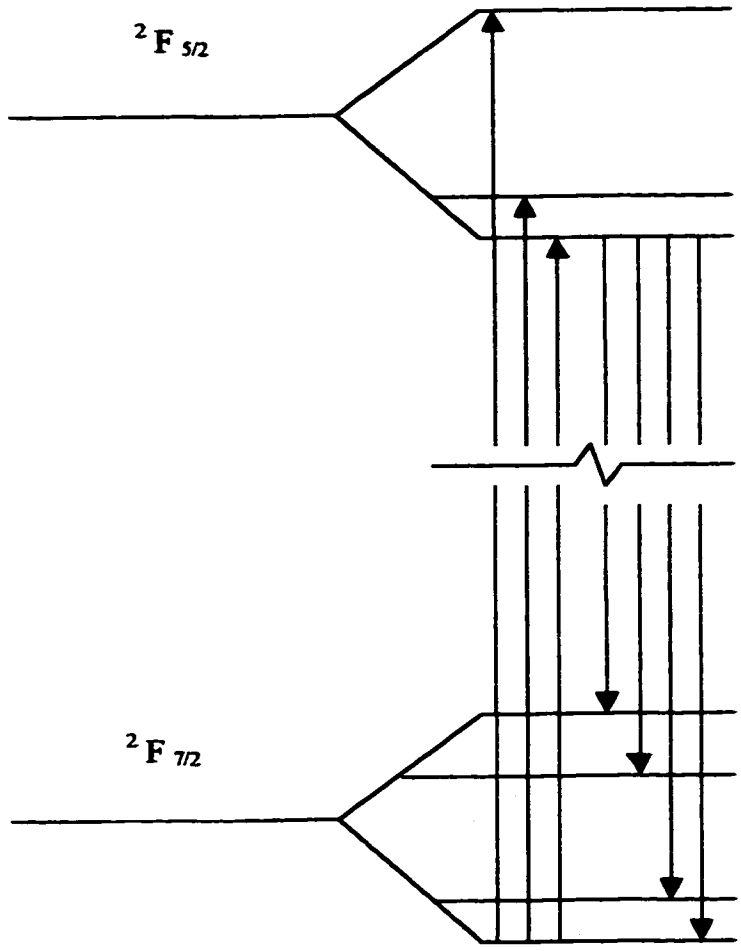

Figure 3.1.3.1. Energy level diagram of the Yb^{3+} ion [66].

3.2 THE FREE ION HAMILTONIAN

The Hamiltonian that describes the free ion states can be written as a sum of various individual Hamiltonians as follows [110]:

$$H_F = -\frac{\hbar^2}{2m}\sum_{i=1}^{N}\nabla_i^2 - \sum_{i=1}^{N}\frac{Z^* e^2}{r_i} + \sum_{i>j=1}^{N}\frac{e^2}{|r_i - r_j|} + \zeta\sum_{i=1}^{N} s_i \cdot l_i \qquad 3.2.1.$$

where N =1,...14 is the number of 4*f* electrons of mass m, Z^*e is the screened electronic charge, ∇_i is the Laplacian operator relative to the i^{th} electron, $|r_i - r_j|$ is the distance between the electrons i and j and ζ is the spin-orbit coupling parameter.

In equation 3.2.1, the first term, H_0, represents the potential of a 4*f* electron due to the presence of the nucleus and the inner electronic shells. In this approximation, the 4*f* electrons are completely independent of one another and contributions involving electrons in closed shells are neglected, thus H_0 can also be expressed by the following equation:

$$H_0 = \sum_{i=1}^{N} -\frac{\hbar^2}{2m}\nabla_i^2 + U(r_i) \qquad 3.2.2.$$

where N is the number of 4*f* electrons of mass m, $\hbar\nabla_i$ is the momentum of the i^{th} electron and $U(r_i)$ is the spherical average potential energy function of the i^{th} electron in the field of the nucleus and all other electrons.

The second term in equation 3.2.1., H_Z, along with H_0, represents the Coulombic interaction with the nucleus. Excluding the 4*f* shell, all electronic shells are

spherically symmetric and do not contribute significantly to the relative positions of the 4*f* energy levels. The real charge of the nucleus is replaced by screened charge since the interaction of the 4*f* electrons with the closed shells modifies only the magnitude of the term and not its symmetry. The aforementioned two terms of the Hamiltonian are spherically symmetrical and as a result do not remove any of the degeneracies within the configuration of the 4*f* electrons [110].

The last two terms in equation 3.2.1. are responsible for the energy level structure of the 4*f* electrons. The third term, H_{CI} represents the mutual Coulombic interaction of the 4*f* electrons that splits the energy level of the 4*f* electronic configuration into a number of LS terms. The final term in equation 3.2.1. is the spin orbit coupling, H_{SO}. This interaction results with only J as a good quantum number since it mixes levels of different L and S [45,114,115]. The spin-orbit coupling parameter, ζ can therefore be represented as a series of radial integrals as follows [110]:

$$\zeta = \frac{\hbar^2}{2m^2c^2}\int_0^\infty R_{4f}^2(r)\cdot\frac{1}{r}\frac{dU(r)}{dr}dr \qquad 3.2.3.$$

where $R_{4f}(r)$ is the radial wavefunction of the 4f electrons and U(r) is the potential in which the i^{th} electron is moving (see equation 3.2.2.).

In the case of the rare-earth ions, the H_{CI} and H_{SO} are approximately equal in magnitude and thus the two terms cannot be considered separately and a coupling calculation is required. It is convenient to perform the calculation in a set of basis functions, where the Coulomb and spin orbit Hamiltonian are diagonal. The basis function used is the total angular momentum function, $|JM_J>$, where the total momentum operator

is given by:

$$\vec{J} = \vec{L} + \vec{S} \qquad 3.2.4.$$

The values of J are restricted to:

$$|L - S| \leq J \leq |L + S| \qquad 3.2.5.$$

and the matrix elements can be obtained using the following relation:

$$< J', M', L', S' | H_{CI} + H_{SO} | J, M, L, S, >= \delta_{JJ'} \delta_{MM'} \qquad 3.2.6.$$

It is very difficult to obtain the true energies of the free-ion experimentally, however, solutions to the free-ion Hamiltonian for the RE^{3+} ions have been reported based on a theoretical analysis of the spectra of RE^{3+} in aqueous solutions. For the case of rare-earth ion in solids, the positions of the electronic energy-level barycenters are insensitive to the host material [116] and closely resemble those of the free-ion. Table 3.2.1a. and Table 3.2.1.b. show the free-ion energy-level barycenters of Eu^{3+} [117] and Er^{3+} [117], respectively. These values will be used as the initial free-ion parameters for the crystal-field calculation, which will be described in the following chapter.

Table 3.2.1a.

Free-ion energy levels for the Eu^{3+} ion

J-level	Level (cm^{-1})
$^7F_0$	0.0
$^7F_1$	381.0
$^7F_2$	1049.5
$^7F_3$	1911.9
$^7F_4$	2897.9
$^7F_5$	3958.7
$^7F_6$	5060.2
$^5D_0$	17316.6
$^5D_1$	19057.3
$^5D_2$	21529.8
$^5D_3$	24420.7
$^5L_6$	25406.3

Table 3.2.1b.

Free-ion energy levels for the Er^{3+} ion

J-level	Level (cm^{-1})
$^4I_{15/2}$	109.0
$^4I_{13/2}$	6609.7
$^4I_{11/2}$	10219.7
$^4I_{9/2}$	12380.7
$^4F_{9/2}$	15245.2
$^4S_{3/2}$	18461.7
$^2H_{11/2}$	19258.1
$^4F_{7/2}$	20421.9
$^4F_{5/2}$	22074.4
$^4F_{3/2}$	22421.7
$^2G_{9/2}$	24509.0
$^2G_{11/2}$	26500.1
$^2K_{15/2}$	27800.4
$^2G_{7/2}$	27981.0

3.3 CRYSTAL FIELD HAMILTONIAN

The simplest method used to calculate the crystal-field is a point-charge model where the ions surrounding the rare-earth ion are described as point charges. This model neglects both the finite spatial extent of the ligand charge density and the wavefunction overlap of the optically active $4f$ electrons with the ligands [118]. Since the optical transitions characteristic of the rare-earth ions doped in solids correspond mostly to intra f^N transitions of predominately electric dipole character [119], and only the f electrons are affected by the crystal-field, it is assumed that the crystal-field acts as a perturbation of the free-ion energy levels. The total Hamiltonian of the rare-earth ion doped in a solid can therefore be described as the sum of the free-ion Hamiltonian and the crystal-field Hamiltonian:

$$H = H_F + H_{CF} \tag{3.3.1.}$$

where H_F is the free ion Hamiltonian described in Section 3.2 and H_{CF} is the crystal-field Hamiltonian.

The crystal-field Hamiltonian used to describe the interaction of the rare-earth ions with the host matrix can be written in terms of spherical harmonics as follows:

$$H_{CF} = \sum_{k,q} B_q^k C_q^{(k)}(\theta,\phi) \tag{3.3.2.}$$

where the summation is over all electrons, k is the rank of the tensoral operator C, q is the relevant component of that operator ($-k \le q \le k$) and B_q^k is the expansion coefficient that

contains all the radial information. The crystal-field parameter, B_q^k, can be regarded as the coefficients of expansion, which are determined empirically from the magnitude of the splitting ΔE. B_q^k can also be written as B_{kq} and is equivalent to the following relation:

$$B_{kq} = -e\int(-1)^q \rho(R) C_{k-q} \frac{r_<^k}{r_>^{k+1}} d\tau = A_{kq}\langle r^k \rangle \qquad 3.3.3.$$

where A_{kq} is the spatial integral of the charge distribution and is given by:

$$A_{kq} = -\frac{e^2}{4\pi\varepsilon_0}\sum_i q_i \frac{C_{kq}(\sigma_i,\phi_i)}{R_i^{k+1}} \qquad 3.3.4.$$

The angular C_{kq} (θ_i ϕ) spherical tensors in equations 3.3.2.-3.3.4. are directly related to the spherical harmonics Y_{kq} (θ_i ϕ) [120] by:

$$C_q^{(k)}(\theta,\phi) = \sqrt{\frac{4\pi}{2k+1}} Y_k^q(\theta,\phi) \qquad 3.3.6.$$

The crystal-field parameter, A_{kq}, can be obtained by using the atomic configurations generated from the molecular dynamics simulations and by selecting the appropriate ionic charges for each type of ion. Employing the three-parameter theory proposed by Leavitt et al. [121], the crystal-field parameters, B_{kq}, are related to the crystal-field components according to the following relation:

$$B_{kq} = \rho_k A_{kq} \qquad 3.3.7.$$

The ρ_k are ion and host independent parameters defined by the following expression:

$$\rho_k = \left\langle r^k \right\rangle_{HF} \cdot (1 - \sigma_k) / \tau^k \qquad 3.3.8.$$

where the $< r^k >_{HF}$ parameters are the Hartree-Fock radial expectation values for the rare-earth ion [122] and σ_k are linear shielding factors known as Sternheimer shielding factors [123]. In order to account for the inadequacy of the bare Hartree-Fock wavefunction and the expansion of the free-ion wavefunction, a scaling factor, τ, was included into equation 3.3.8. The value τ, is approximately a linear function of the number of 4*f* electrons in the rare-earth ions, $\tau = 0.767 - 0.00896N$, where N = number of electrons in the 4*f* shell of a given rare-earth ion. [124]. Table 3.3.1. shows the ρ_k values for Eu^{3+} [125] and Er^{3+} [125].

Table 3.3.1.

Values of ρ_k parameters with k=2,4 and 6 for the Eu^{3+} and Er^{3+} ions used to convert lattice sums A_{kq} to crystal-field parameters B_{kq}.

	ρ_k (Å^k)	
	Eu^{3+}	Er^{3+}
ρ_2	0.1666	0.1706
ρ_4	0.4836	0.4053
ρ_6	1.2503	0.9649

The B_{kq} crystal-field parameters are directly related to the point symmetry of the local environment of the rare-earth ions. The relationship between the point-symmetry and the non-vanishing B_{kq} parameters is shown in Table 3.3.2. In the case of the *f* electrons, only the terms with $k \leq 6$ are nonzero and due to the odd parity components of the crystal field, the odd k terms do not contribute to the matrix elements and are thus omitted in the crystal-field Hamiltonian [119]. In other words only the terms with k = 2, 4 or 6 provide the matrix elements of H_{CF} and have effect in the calculation of the energy levels. The "site symmetry" of the ions of interest (Eu^{3+} and Er^{3+}) governs which terms are permitted in the crystal field Hamiltonian and the number and type of crystal field energy levels that arise from the (2J+1)-fold degenerate free ion levels. The crystal field calculations reported herein were carried out using a C_1 point group symmetry for the rare-earth environment. The reasons are discussed in Section 5.2 of this thesis.

Table 3.3.2.

Independent non-vanishing B_{kq}* parameters for the 32 point-symmetry groups

Point Group	Non-vanishing B_{kq} parameters
C_1, C_I	All B_{kq} (B_{21} real)
C_2 Cs C_{2h}	B_{20},ReB_{22},B_{40},B_{42},B_{44},B_{60},B_{62},B_{64},B_{66}
D_2 C_{2v} D_{2h}	B_{20},ReB_{22},B_{40},ReB_{42},ReB_{44},B_{60},ReB_{62},ReB_{64},ReB_{66}
C_4 S_4 C_{4h}	B_{20},B_{40},ReB_{44},B_{60},B_{64}
D_4, C_{4v} D_{2d}, D_{4h}	B_{20},B_{40},ReB_{44},B_{60},ReB_{64}
C_3, S_6	B_{20},B_{40},ReB_{43},B_{60},B_{63},B_{66}
D_3 C_{3v} D_{3d}	B_{20},B_{40},ReB_{43},B_{60},ReB_{63},ReB_{66}
C_6, C_{3h} C_{6h}, D_6 C_{6v}, D_{3h} D_{6h}	B_{20},B_{40},B_{60},ReB_{66}
T, T_d, T_h O, O_h	B_{40},ReB_{44},B_{60}, ReB_{64}

*Note: With the exception of B_{k0}, all the B_{kq} parameters are complex numbers.

3.4 SELECTION RULES

The intensity of absorption or emission accompanying a transition is related to the probability of the transition, such that the more probable transitions yield absorption or emission of very high intensity [126]. The requirements of absorption of light by the matrix can be described based on the selection rules [126]. Transitions that are possible according to these rules are referred to as allowed transitions, while those which are not possible, are referred to as forbidden transitions.

Optical transitions in trivalent rare-earth ions occur due to perturbations caused by the interaction between the electrons in the $4f$ shell and the electromagnetic field. In order for transitions to occur from one state to another, the presence of the electromagnetic field is essential to produce coupling between different states. The interaction Hamiltonian between the electrons and the radiation field is comprised of two terms, the electric dipole interaction and the magnetic dipole interaction. In general, there are two radiative processes that may occur when these electrons interact with the electromagnetic field, absorption and emission.

The selection rules are determined based on group theory such that the components of the electric and magnetic field vectors transform according to definite representations of the point group of the local rare-earth environment. If a particular transition is either allowed or forbidden depends upon whether the irreducible representation of the final state is, or is not, contained in the product of the initial state representation, and the representation of the appropriate component of the electric field, E or the magnetic field, B [127]. Whether or not a radiative transition between two states is allowed and, if allowed, how strong the transition is depends on the value of the following matrix element.

$$\langle b|\vec{\mu}\cdot\hat{\varepsilon}|a\rangle \qquad 3.4.1.$$

where, $\vec{\mu}\cdot\hat{\varepsilon}$ is the appropriate dipole operator between states a and b.

Laporte's selection rule states that the only allowed transitions are those in which the parity of the final state is different than the parity of the initial state, that is $\Delta l = \pm 1$. Therefore, transitions should not be observed in rare-earth ions due to the fact that $f \leftrightarrow f$ transitions should be forbidden since, for both the initial and final states, $l = 3$. This, however, is not the case as there is a relaxation of Laporte's rule due to admixing of the odd parity *f*-states with even-parity states, usually *5d* or *5g* configuration states or charge transfer [106].

The selection rules on S and L are valid in the limit of Russell-Saunders coupling, but since transitions are between linear combinations of Russell-Saunders states they are not rigidly adhered to and S and L are no longer good quantum numbers [128]. The selection rules on J, however, are more rigorous and can only be broken by 'J-mixing', which is a weak effect.

A set of selection rules can therefore be written for both electric and magnetic dipole transitions [106,128].

The electric dipole operator is given by the following expression:

$$\vec{\mu}_e = \sum_i e\vec{r}_i \qquad 3.4.2.$$

where Σex_i, Σey_i, Σez_i, transform like translations such that linear combinations of these components may be obtained to from an irreducible tensor operator of the first

order [129].

For electric dipole transitions of the $4f$ electrons, the following selection rules apply:

$$\Delta l = \pm 1 \qquad 3.4.3.$$

$$\Delta S = 0$$

$$|\Delta L| \leq 6$$

$$|\Delta J| \leq 6 \text{ unless } J \text{ or } J' = 0, \text{ then } |\Delta J| = 2,4,6$$

$$|\Delta M_J| = p+q$$

where p is determined by the particular point group symmetry.

For magnetic dipole interactions, the dipole operator is represented as follows:

$$\vec{\mu}_m = \sum_i \frac{-\hbar}{2mc}(l_i + g_e s_i) \qquad 3.4.4.$$

The selection rules for the magnetic dipole interactions are given by:

$$\Delta l = 0 \qquad 3.4.5.$$

$$\Delta S = 0$$

$$\Delta L = 0$$

$$\Delta J = 0, \pm 1 \text{ (not } 0 \leftrightarrow 0)$$

$$\Delta M_J = 0 \ (\sigma \text{ polarization})$$

$$\Delta M_J = \pm 1 \ (\pi \text{ polarization})$$

In the case of rare-earth ions, the valid rules are determined by the site symmetry, however, due to the weak crystal field, the selection rules of the free ion are still relevant. As previously mentioned, electric dipole transitions within a f^n configuration are allowed only due to environmental perturbation. Consequently, the selection rules are determined strictly by the local field site-symmetry of the ion. For point groups of very

low symmetry such as C_2, C_s or C_1, all $f \leftrightarrow f$ transitions are allowed, therefore the only consideration is the relative magnitude of the contribution from each of the dipole processes.

3.5 INTENSITY CALCULATIONS

The crystal-field model may also provide a calculation scheme for the transition probabilities between levels perturbed by the crystal-field. According to Condon and Shortley [130], the line strength, S_{ab}, of a radiative transition is given by the square of the following matrix elements:

$$S_{ab} = \left| \langle b | P | a \rangle \right|^2 \qquad 3.5.1.$$

where P is the appropriate electric or magnetic dipole operator ($\vec{\mu} \cdot \hat{\varepsilon}$).

Electric dipole intensity calculations were performed using the "full" Judd-Ofelt theory. The Judd-Ofelt theory is useful in estimating the probability of the forced electric dipole transitions of rare-earth ions in various environments. According to the Judd-Ofelt theory, the electric dipole transitions between two states of $4f^N$ configuration of rare-earth ions, which are forbidden when the ions are free, become allowed in the crystal-field by mixing into the $4f^N$ configuration another configuration having opposite parity. Judd [131] postulated that the possible configurations to be mixed into $4f^N$ are those of the type $4f^{N-1}nl^1$ ($n \geq 5$, $l \neq 3$). Moreover, the matrix elements of the electric dipole operator are calculated by considering the crystal-field as a first-order perturbation. This calculation is simplified by setting the following four approximations [113]. First, the states of $4f^N$ configurations are taken as linear combinations of Russell-Saunders coupled states.

Second, all M_J levels of the ground state are assumed to be equally populated. Third, the energy of the states of the configurations mixed into $4f^N$ configurations is assumed to be much larger than that of $4f^N$ configuration. Fourth, the local field approximation is employed. The effective electric dipole operator used in the present calculations has been proposed by Morrison et al. [132] and can be expressed as:

$$P^{ED} = -2\sqrt{\frac{7}{3}}\sum_{k,t}(2t+1)N_k(t)\left(A^{(k)}U^{(t)}\right)^{(1)}_{\alpha} \qquad 3.5.2.$$

where the sums run over the order values of k=1,3,5,7 and t=2,4,6. The value of $\left(A^{(k)}U^{(t)}\right)^{(1)}_{\alpha}$ represents the coupling of the irreducible tensors $A^{(k)}$ and $U^{(t)}$, and $N_k(t)$ contains the Clebsch Gordon coefficients [132,133] and the radial matrix elements of R_k. The parameters for $N_k(t)$ are defined as follows [132,133]:

$$N_k(t) = \sum_{t=2,4}(2l+1)\begin{Bmatrix}1 & t & k\\ 3 & l & 3\end{Bmatrix}\begin{pmatrix}3 & 1 & l\\ 0 & 0 & 0\end{pmatrix}\begin{pmatrix}l & k & 3\\ 0 & 0 & 0\end{pmatrix}R_k(l) \qquad 3.5.3.$$

Subsequently, calculation of the induced electric-dipole line strength, S_{ab}^{ED}, can be accomplished through the methods proposed by Krupke [134] and Leavitt and Morrison [132].

Within the electronic configuration $4f^N$, magnetic dipole transitions are parity allowed, and the magnetic dipole line strength, S_{ab}^{MD}, can be obtained by means of the proper dipole moment operator, which involves the total orbital and spin angular momentum operators. The magnetic dipole operator is therefore given by:

$$P^{MD} = -\frac{\hbar}{2mc}(L + g_e S) \qquad 3.5.4.$$

where L and S are the total vibrational and spin angular momentum operators. It is important to mention that J-mixing of the eigenstates is included in the calculation of both the electric and magnetic dipole line strengths.

In calculating the intensity of line-to-line transitions in the simulated emission spectrum, the transition probability between the individual components a and b, A_{ab}^{emiss}, was calculated as follows:

$$A_{ab}^{emiss} = \frac{32\pi^2 e^2 \sigma_{ab}^3}{3\hbar 4\pi \varepsilon_0}\left[\left(\frac{n(n^2+2)^2}{9}\right)S_{ab}^{ED} + n^3 S_{ab}^{MD}\right] \qquad 3.5.5.$$

where n is the refractive index at the wavelength of the emitted or absorbed light, σ is the energy difference between the initial and the final states and S_{ab}^{ED} and S_{ab}^{MD} are the electric and magnetic dipole line strengths, respectively. The individual components a and b belong to the initial and final electronic manifolds of the electronic transition under investigation.

CHAPTER 4

4.0 EXPERIMENTAL METHODS

4.1 PREPARATION OF THE LABORATORY GLASSES

Three samples of RE^{3+} doped lead silicate glasses were prepared by Prof. Marco Bettinelli, of the Sezione di Chimica, Istituto Policattedra, Facoltà di Scienze MM. FF. NN., Università di Verona,Verona, Italy. The compositions of the Eu^{3+}, Er^{3+} and Yb^{3+} glasses expressed in mol% for a "50/50" sample are as follows respectively: (i) 48.5 PbO·50.5 SiO_2·1 Eu_2O_3 (ii) 48.5 PbO· 50.5 SiO_2·1 Er_2O_3 and (iii) 48.5 PbO· 50.5 SiO_2·1 Yb_2O_3. Appropriate quantities of PbO, SiO_2 (both Carlo Erba RPE) and RE_2O_3 (Janssen Reagent Grade) were melted in platinum crucibles and quenched in a brass mould. The samples were melted at 1000 °C for 4 hours and annealed at 250 °C for 12 hours. The samples, having a thickness of about 3mm, were carefully polished for the optical measurements. The nominal RE^{3+} concentration was 0.84 mol·L^{-1} in the all of the 50/50 glass samples.

4.2 PREPARATION OF THE SIMULATED GLASSES

4.2.1. Glasses simulated using the two-body potential model

The simulated glass was prepared using a MD program written in FORTRAN. The original program was obtained from Dr. Thomas Soules of the General Electric Company, Cleveland, Ohio. The program was extensively modified by Dr. Guy Cormier [45] for the specific problem of generating and analyzing doped glasses. The modifications included implementing Mitra's potential, addition of a subroutine to generate configurations at a given series of timesteps, removal of unnecessary parameters which required extra computational time as well as the addition of output parameters

which aided in the bulk structural analysis of the doped glasses.

The simulations were performed using the two-body potential model developed by Mitra et al. [94] described in Section 2.2.1 of this thesis. The parameterization of the potential was taken as determined from previous studies [45,57]. The parameters for oxygen and silicon were determined by Mitra et al. [92-94], while those for lead were determined by Cormier et al. [41]. The charges, radii and n were determined empirically in order to reproduce the short-range order observed in the experimental glasses. The potential was scaled in order to arrive at a simulated glass transition temperature within the experimental range of 1200-1800K. Table 4.2.1.1. presents the ionic parameters, the glass compositions and other relevant parameters used in the simulation.

Table 4.2.1.1.

Simulation parameters for $PbO{\cdot}SiO_2$ glass

Element	Ionic Radius, σ (Å)	Ionic Charge (q)	Number of ions
O	1.200	-1.136	3024
Si	0.237	2.272	1008
Pb	0.990	1.136	1008

Hardness parameter, n:	10
Simulated density (g/cm^3):	5.98
Oxygen molar volume (cm^3/mol O^{2-}):	15.80
Length of box side (Å):	42.97

In order to perform an initial validation of the parameterization of the pair potentials, the structural features of the simulated glass were verified to reproduce the short range order of the parent crystalline compound, lead metasilicate [135].

The initial set of coordinates for the atomic ensemble of the undoped glass was derived from the unit cell of crystalline lead metasilicate, alamosite $PbSiO_3$ [135]. This initial atomic ensemble was melted by heating from 300K to 15000K in a total of 56000 timesteps of 1 fs ($1X10^{-15}$ s). The subsequent quench procedure for the glass was as follows. The melt was thermalized at 15000K for 50000 timesteps (500 ps). The ensemble was then slowly cooled from 15000K, in five successive temperature steps to 7500, 5000, 2500, 1200, 600 and 300 K, each for 80000 timesteps for a total quench time of 0.5 ns at a quench rate of $3X10^{13}$ K/s.

The simulations were carried out at constant volume for each temperature step. The size of the box at 300K was adjusted to give the correct room temperature density for $PbO{\cdot}SiO_2$ glass, which has been determined to be $\rho = 5.98$ g/cm^3. The size of the box was increased at higher temperature steps in order to simulate thermal expansion.

The simulation of the glass was performed using a Hewlett Packard Workstation. The simulation takes an average of three weeks of "real" time per glass depending upon the number of interactive users and the number of background processes.

4.2.2. Glasses simulated using the two and three-body potential model

The FORTRAN program used to carry out the MD simulations was obtained from Professor S.H. Garofalini, at Rutgers University, NJ, USA. The multibody potential used in the simulation was the same as that described in Section 2.2.2 of this thesis.

The initial set of coordinates for the atomic ensemble of the undoped lead silicate glass, $50PbO{\cdot}50SiO_2$ "50/50", was derived from crystalline lead metasilicate, alamosite ($PbSiO_3$) [135]. To generate the undoped glasses of varying PbO

concentrations, the initial configurations were obtained from the respective crystalline structures, ($PbSi_2O_4$) for the $22PbO{\cdot}78SiO_2$ "22/78" glass and lead silicate (Pb_2SiO_4) for the $70PbO{\cdot}30SiO_2$ "70/30" glass.

As a first approximation, EXAFS and XRD data were used to alter the potential energy function, which is achieved by adjusting the atomic force pair interactions to yield the proper interionic distances. Table 4.2.2.1. shows the atomic force parameters for the ion-oxygen pairs of the undoped lead silicate glass. There were no adjustments made to the previously determined parameters for SiO_2, which were developed by Soules [91] and further modified by Feuston et al. [95], while for PbO the following procedure was executed. A parameter search was performed by allowing the respective crystalline compound to run with a given set of parameters at 300K. The radial distribution functions (RDF) of the simulated structure was obtained and compared with experimental results.

In the case of the doped glasses, the RE^{3+}-ion parameters were developed using the aforementioned procedure on the crystalline structures, namely, Eu_2O_3, Er_2O_3 and Yb_2O_3. To obtain the RE^{3+}-doped lead silicate glasses, the alamosite crystal was doped with 1.0% RE_2O_3. A concentration study was performed on the Er^{3+}-doped lead silicate glasses by doping the alamosite crystal with 0.2%, 2.0%, 5.2%, 11% and 24.8% Er^{3+} (Er_2O_3).

The two-body parameters used in the potential for the undoped glasses are listed in Table 4.2.2.1a. and the three-body parameters in Table 4.2.2.1b. The BMH parameters for the doped glasses are listed in Table 4.2.2.1c. and the LJ parameters in Table 4.2.2.1d. The compositions for the Er^{3+}-doped glasses are in Table 4.2.2.2. Both the doped and undoped crystal structures were subjected to the following melt-quench sequence.

The starting configuration was melted by heating the crystal from 300K to 8000K. The velocity was rescaled periodically during the simulation for the first 2000 time steps and the system was then allowed to run at constant energy for an additional 8000 steps. This step was performed in order to allow the system to reach internal equilibrium and to ensure randomization of the initial configuration. The system was then cooled to room temperature in seven successive temperature steps at 7000, 6000, 4000, 3000, 2000, 1000 and 300K. Throughout cooling, at each temperature step, the velocities were rescaled for 20 ps and then continued at constant energy for another 80 ps. At 4000 and 3000K, however, the system was run for 200 ps with an equilibration period of 4000 time steps in order to allow for further structural relaxation. The total quench time of the run was 1.2 ps for a quench rate equal to 6.5×10^{14} K/s.

Table 4.2.2.1a.

Simulation parameters for the undoped glasses

BMH pair potential parameters

Atomic pair	A_{ij} ($\times 10^{-8}$ erg)	β_{ij} ($\times 10^{-7}$ cm)	ρ_{ij} ($\times 10^{-8}$ cm)
O-O	0.0725	0.234	0.290
Si-O	0.2962	0.234	0.290
Pb-O	0.4500	0.224	0.140
Si-Si	0.1877	0.234	0.290
Si-Pb	0.0550	0.260	0.290
Pb-Pb	0.1642	0.260	0.290

Compositional parameters

	22/78*	50/50*	70/30*
No. of O ions	1152	1512	960
No. of Si ions	504	504	224
No. of Pb ions	144	504	512
Density (g/cm^3)	3.725	5.98	7.325

*Corresponding to $22PbO\text{-}78SiO_2$, $50PbO\text{-}50SiO_2$ and $70PbO\text{-}30SiO_2$, respectively

Table 4.2.2.1b.

Three-body potential parameters

Bond angle	r^c_i (Å)	λ_i ($\times 10^{-11}$ erg)	γ_i (Å)
O-Si-O	2.6	0.3	2.0
Si-O-Si	3.0	19	2.8
O-Pb-O	3.0	24	2.8
Pb-O-Pb	2.8	20	3.0

Table 4.2.2.1c.

Simulation parameters for the doped glasses

BMH pair potential parameters

Atomic pair	A_{ij} ($\times 10^{-8}$ erg)	β_{ij} ($\times 10^{-7}$ cm)	ρ_{ij} ($\times 10^{-8}$ cm)
Eu-O	0.4500	0.193	0.150
Er-O	0.4500	0.208	0.150
Yb-O	0.4500	0.202	0.150
RE-Si	0.1000	0.260	0.290
RE-Pb	0.1642	0.260	0.290
RE-RE	0.1642	0.260	0.290

Compositional parameters for RE^{3+}:PbO-SiO_2

No. of O ions	No. of Si ions	No. of Pb ions	No. of RE ions
1512	504	474	20
Density (g/cm^3)	5.98		

Table 4.2.2.1d.

Parameters used in the Lennard-Jones potential

Atomic Pair	ε_{ij} ($\times 10^{-12}$ erg)	σ_{ij} ($\times 10^{-8}$ Å)
Pb-O	2.375	2.323
Eu-O	9.650	2.130
Er-O	6.650	2.020
Yb-O	6.550	2.130

Table 4.2.2.2.

Compositional parameters for Er^{3+}:PbO-SiO_2 glasses

	Percentage of Er^{3+} ion in the simulated glasses				
No. of ions	0.2	2.0	5.2	11.0	24.8
O ions	1512	1512	1512	1512	1512
Si ions	504	504	504	504	504
Pb ions	501	474	429	354	204
Er ions	2	20	50	100	200
Density	5.98 g/cm^3				

The simulations of the glasses were performed using a Silicon Graphics R10000 INDIGO^2 Workstation. The simulation takes an average of 12 days of "real" time per glass depending upon the number of interactive users and the number of background processes.

4.3 SPECTROSCOPY OF THE LABORATORY GLASS

The room temperature luminescence spectra were recorded in the visible and NIR regions. Visible emission spectra were recorded by using a Jarrell–Ash 1–m Czerny–Turner double monochromator. The visible emission signal was monitored by an RCA–C31034–02 photomultiplier. The photomultiplier was thermoelectrically cooled so that its background dark rate was below 2 counts/s. The photomultiplier signal was processed by a preamplifier, model SR–440 (Stanford Research Systems). A two–channel gated photon–counter, Model SR–400 (Stanford Research Systems) was used as the data acquisition system. The signal was recorded under computer control using the Stanford Research Systems' SR–465 software data acquisition/analysis system. The near–infrared

emission spectra were recorded in the region 900 nm -1.8 μm using a Jarrell–Ash 3/4–m Czerny–Turner single monochromator. The signal was detected by a liquid nitrogen–cooled Northcoast EO–817P germanium detector connected to a computer–controlled Stanford Research SR510 lock–in amplifier. All the reported spectra were corrected for the response of the individual detectors.

4.4 SPECTROSCOPY OF THE SIMULATED GLASS

The calculation of the crystal-field parameters of the simulated glass and the subsequent generation of the simulated emission spectra was performed using a series of programs developed at the Harry Diamond Laboratories, Adelphi MD [136]. These programs were modified by Dr. Guy Cormier to generate the absorption and emission spectra of Eu^{3+}-silicate and Eu^{3+}-sodium disilicate glasses. Further modifications were also made by Dr. Stephane Chaussedent in order to generate the emission spectrum of the Eu^{3+} ion in aqueous solution. The program used for the generation of the RE^{3+} emission spectra in this thesis is a combination of the latter two modifications and the procedure is outlined herein.

In order to correlate the energy levels with the structure and charge distribution at each of the rare-earth sites, a principal axis transformation of each of the 200 RE^{3+} ions was performed. The transformation starts by placing a RE^{3+} ion in the center of a Cartesian coordinate system representing the glass configuration [45,137,138]. This transformation will result in a diagonalization of the quadrupole moment tensor such that all the second-order crystal field parameters vanish except for A_{22} and ReA_{22}.

Once all the glass configurations are aligned, the crystal-field parameters are calculated using the positions of all ions with respect to the central RE^{3+} ion and the charges assigned to each ion type. The spherical tensors, C_{kq} are subsequently determined using a recursive method that calculates the associated Legendre polynomials. The C_{kq} parameters are then used to calculate the crystal-field components, A_{kq} according to equation 3.3.4. The odd-k A_{kq} crystal field components are used for the intensity calculations, while the even-k A_{kq} are transformed into crystal-field parameters, B_{kq} using the appropriate ρ_k values for the rare-earth ion of interest reported in Table 3.3.1. The energy level splittings are then calculated using the even-k B_{kq} crystal-field parameters. Moreover, transition probabilities, lifetimes and branching ratios for all excited states are also calculated.

In order to generate a graphic representation of the simulated emission spectra, the calculated energies are collated and sorted. A Lorenztian band shape is assigned to each of the energies. The spectral envelope, $\Xi(\sigma)$, is given by:

$$\Xi(\sigma) = \frac{\omega^2}{N_0} \sum_{k=1}^{N_0} \sum_{a,b} \frac{I_{k,ab}}{\omega^2 + 4\left(\sigma - \sigma_{k,ab}\right)^2} \qquad 4.4.1.$$

where the first sum is over all N_0 environments obtained from the MD simulations, the second sum is over all possible transitions. Each of the energies have an amplitude, $I_{k,ab}$, and a full width at half maximum, ω. The widths were chosen such that all the RE^{3+} ions in the simulated glass effectively represent the macroscopic ensemble of doped ions found in the experimental glass. The intensity (amplitude) is given by [57]:

$$I_{k,ab} = F_{J_1(ab)}(\beta_{k,ab}, A_{k,ab}) \qquad 4.4.2.$$

where F_J are scaling factors for each J multiplet and $B_{k,ab}$ are the radiative branching ratios. The $\beta_{k,ab}$ are radiative branching ratios for line-to-line fluorescence transitions, and are defined as the ratio of a specific radiative transition from an emitting state to a lower energy state divided by the sum of all the radiative transitions initiated from the emitting state of the k^{th} RE^{3+} configuration as follows [57]:

$$\beta_{k,ab} = \frac{A_{k,ab}^{emiss}}{\sum_{a,b} A_{k,ab}^{emiss}} \qquad 4.4.3.$$

where a represents a given emitting state and b represents the lower energy states. The $A_{k,ab}^{emiss}$ are the line-to-line radiative transition probabilities for the k^{th} configuration as defined by equation 3.5.5., and the sum is over all the possible lower states. The sum of all β_{ab} is necessarily 1.

CHAPTER 5

5.0 RESULTS AND DISCUSSION

5.1 STRUCTURAL ANALYSIS OF THE MD SIMULATED GLASS

5.1.1. Structure of undoped lead silicate glass

The general structure of the glasses was determined by calculating the pair (PDF) and cumulative (CDF) distribution functions as well as bond angle distributions (BAD). In addition, whenever possible a comparison to experimentally reported structural features with those obtained through the MD simulations will be performed.

5.1.1.1. Comparison of the two- and three-body potential models

The starting point in structural investigations of glasses is to examine the atomic structure of the crystalline stoichiometric counterpart. In the present case, the lead metasilicate stoichiometry presents three polymorphs, with the mineral alamosite being the stable phase [135]. The structure of alamosite (Figure 5.1.1.1.1) is comprised of zigzag chains of SiO_4 tetrahedra and screw chains of PbO_n polyhedra (n = 3 or 4). The chains of SiO_4 tetrahedra are arranged in parallel layers, and the screw chains of PbO_n polyhedra are perpendicular to the silicate layer. The lead atoms in this crystal are found at the apex of a PbO_3 trigonal or PbO_4 tetragonal pyramid. The three distinct lead atomic types found in the alamosite unit cell have a coordination of 3, 4 and 4, respectively. Such a coordination scheme is essentially due to the electronic structure of the divalent lead ion. The combined orbitals on Pb leave a non-bonded electronic pair of sp hybrid orbitals. Thus, the short Pb – O bond ($r_{bond} \leq 2.60$Å) is essentially covalent and the electronic lone pair is directed out of the pyramid and occupies the place of the missing ligands.

essentially covalent and the electronic lone pair is directed out of the pyramid and occupies the place of the missing ligands.

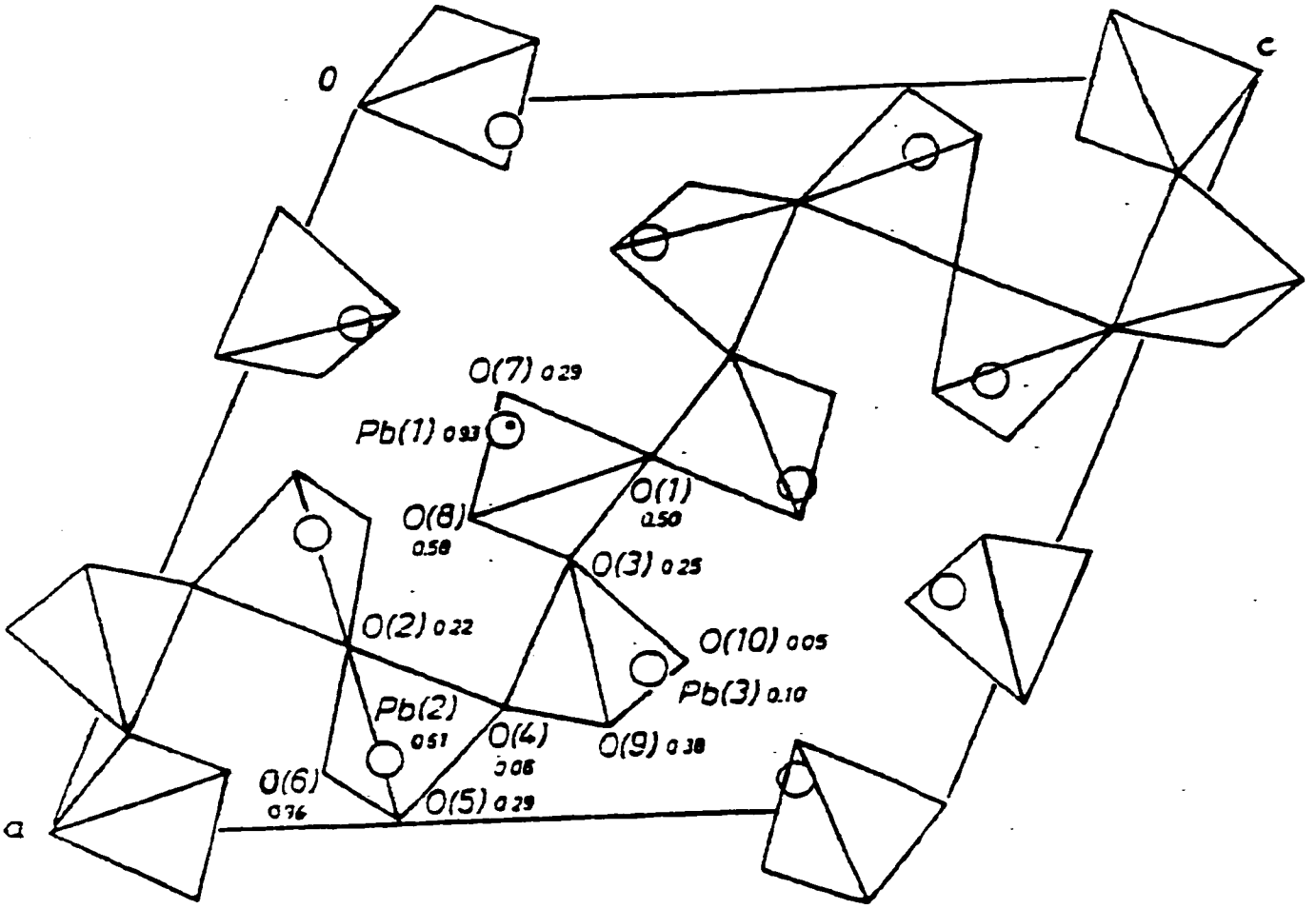

Figure 5.1.1.1.1. Projection of the structure of alamosite. Oxygens atoms are represented by tetrahedron vertices, and Pb atoms by circles [135].

This structure explains the low coordination of divalent Pb. This immediate covalent coordination shell has been defined by the presence of oxygen atoms within a 2.6Å distance from the lead atoms. Slightly beyond this distance, each of the three lead types will have additional oxygens in their environments. This conclusion has been derived from a calculation based on the crystallographic data of Boucher and Peacor [135], for the local environments of the 16 atom types found in the unit cell, up to a distance of 6.5Å. Examining the oxygens found within the first lead – cation distance, the coordination number increases substantially to 6, 6, and 8, respectively. In order to make a valid comparison between the crystalline and amorphous structures, this extended first coordination shell was found to be more representative of the local environment of the lead ions.

Due to the extensive structural information present, analysis of the undoped lead metasilicate glass will be separated into two main aspects, (i) the silicate backbone and (ii) the environment of the lead atoms with respect to the silicate backbone. For simplicity, the combination two/three-body potential model will be referred to as the three-body potential model for the remainder of this section.

(i) The silicate backbone

The room temperature equilibrated pair distribution functions for the silicon-oxygen pair from the two (dashed curve) and three-body (solid curve) glasses are illustrated in Figures 5.1.1.1.2a., while the cumulative distributions for the two glasses are shown in Figure 5.1.1.1.2b. The average Si-O interionic distance was found to be 1.60 Å with a full width half maximum (FWHM) of 0.13 Å for the two-body glass and 1.62 Å with a FWHM of 0.08 Å for the three-body glass.

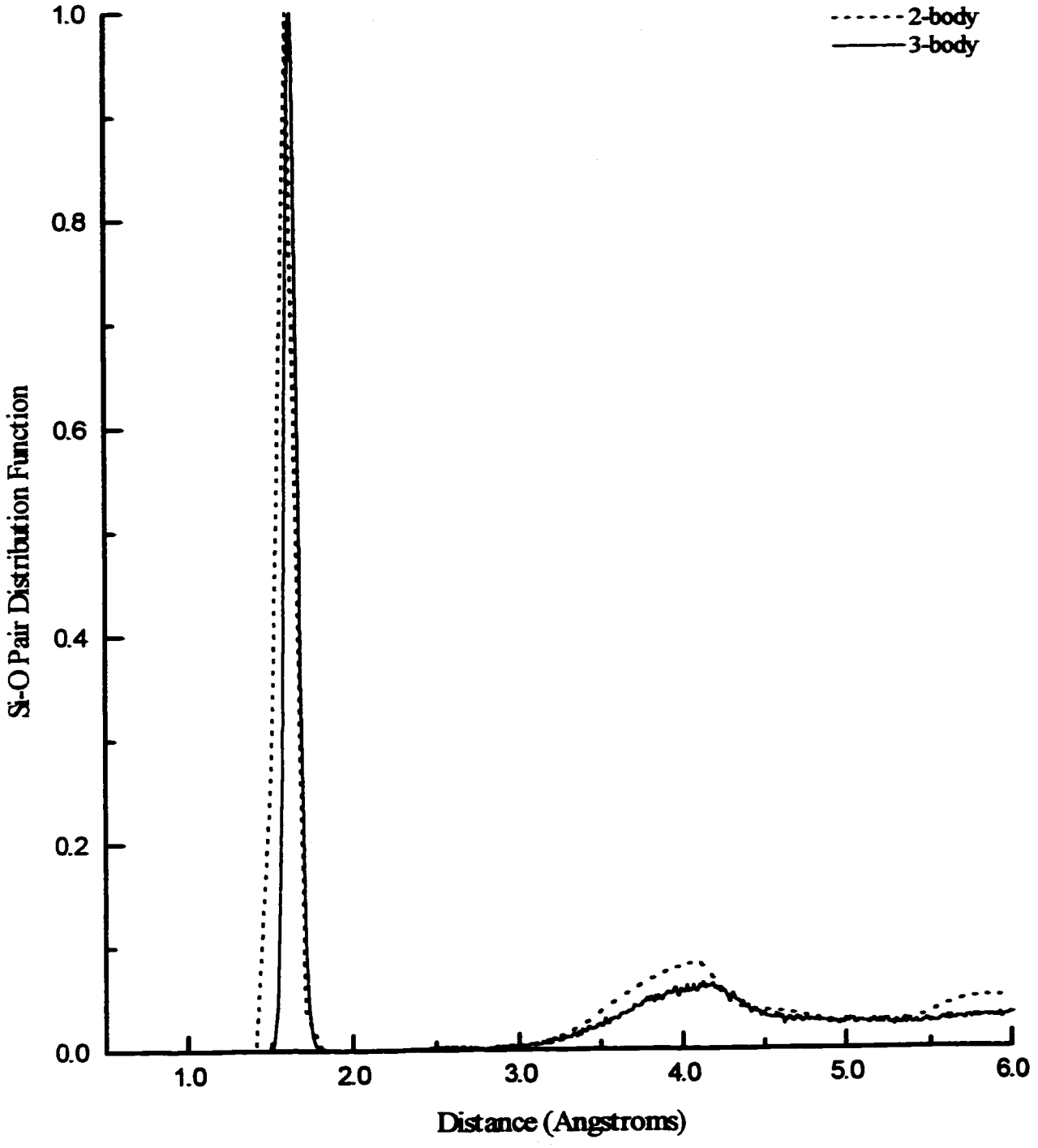

Figure 5.1.1.1.2a. Pair distribution functions of the 2-body (dashed) and 3-body (solid) Si-O interionic pair for the undoped $PbO{\cdot}SiO_2$ simulated glasses.

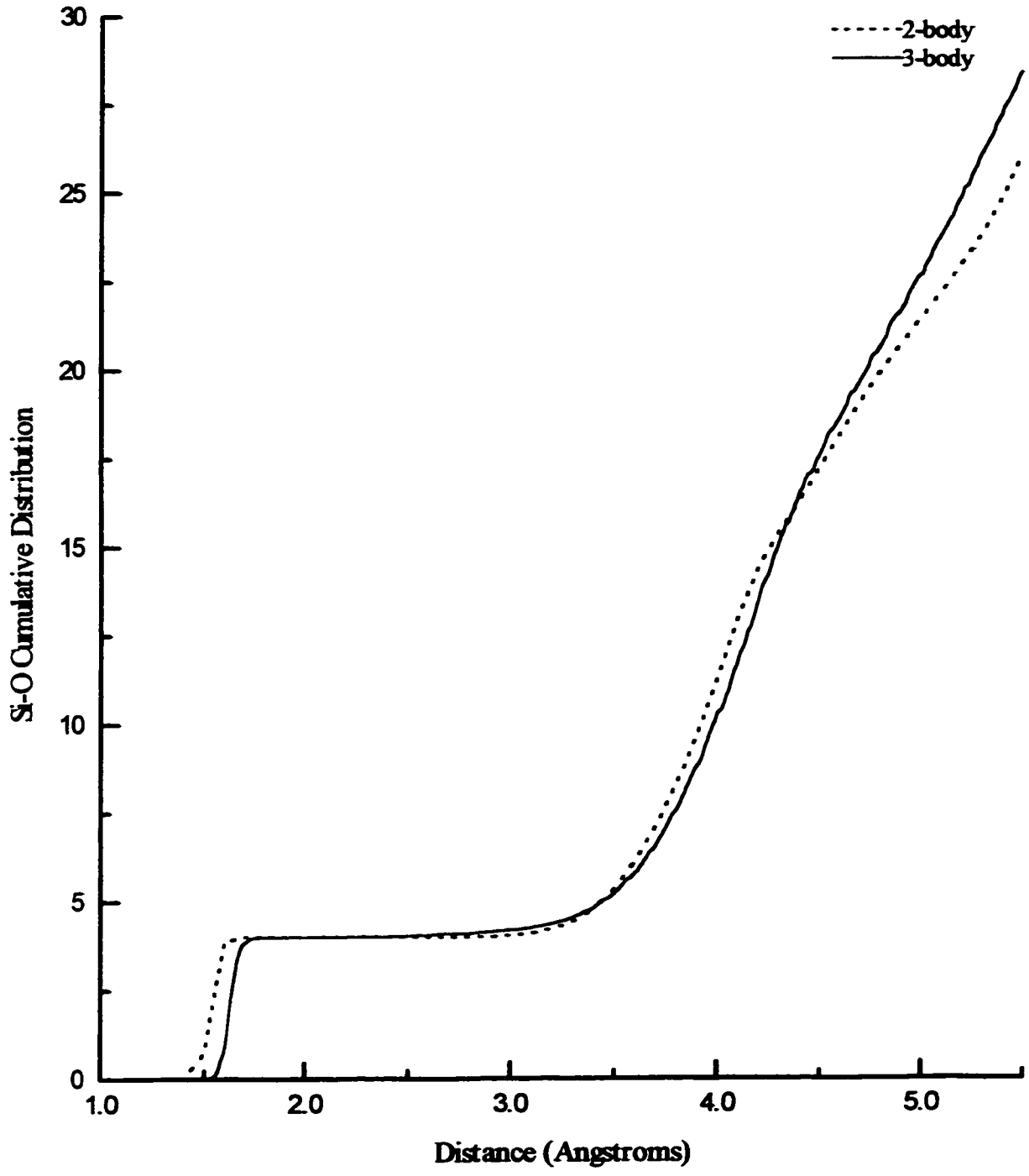

Figure 5.1.1.1.2b. Cumulative distribution functions of the 2-body (dashed) and 3-body (solid) Si-O interionic pair for the undoped $PbO\text{-}SiO_2$ simulated glasses.

Extrapolation of the CDF curve at a cutoff radius of 2.1 Å, indicated that for both the two- and three-body glasses, each silicon is tetrahedrally coordinated by 4.00 oxygens. Similar results for the silicate tetrahedra were observed experimentally by Mydlar et al. [30] and Yamada et al. [23].

The three-body potential model resulted in a significant narrowing of the first Si-O peak as seen by the reduction of the FWHM from 0.13 Å in the two-body glass to 0.08 Å in the three-body glass. Moreover, the number of odd coordinated species decreased for the glass modelled using the three-body potential as shown by the narrowing at the base of the first peak in the three-body PDF (solid) in comparison to that of the two-body PDF (dashed). The pair distribution functions return to a null value after the first peak indicating that a clear distinction exists between the first and second coordination shell. This is also observed in the cumulative distribution function (Figure 5.1.1.1.2b.) by the plateau which extends from 1.8 to 2.5Å. Further analysis of the Si-O connectivity indicated that all the silicate tetrahedra are connected through their corners and not by their edges or faces, which is characteristic of the high-energy arrangements. The well defined short range order is illustrated further by the determination of the bond angle distributions.

The O-Si-O bond angle distribution (Figure 5.1.1.1.3.) was found to be 109° with a FWHM of 8.5° for the two-body model (dashed) and 109.7° with a FWHM of 6.0° for the three-body model (solid). The O-Si-O bond angle distributions for both simulated glasses were found to be in excellent agreement with experimental results (104-115°) and the theoretical value (109.4°). The half-width of the O-Si-O angle distribution was calculated to be approximately 7° [94], based on electron spin resonance (ESR) data, confirming the improvement of the three-body model over the two-body model.

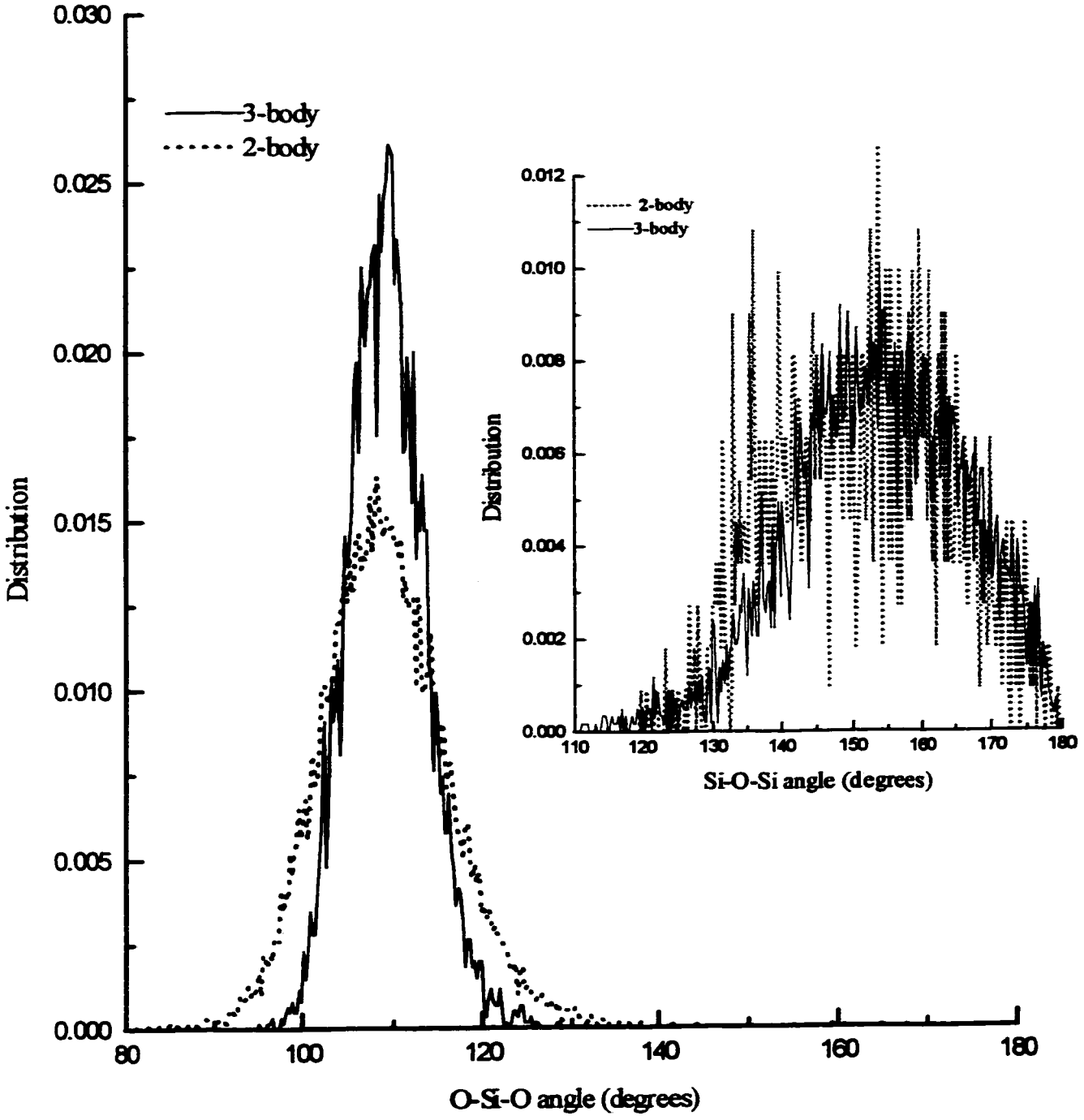

Figure 5.1.1.1.3. The O-Si-O bond angle distributions for the two-body (dashed) and three-body (solid) simulated lead silicate glass. Shown in the inset is the Si-O-Si bond angle distributions for the two-body (dashed) and three-body (solid) simulated lead silicate glass.

The bond angle distribution functions are not only an indication of the basic units (SiO_4 tetrahedra) which make up the silicate network but also allows the prediction of how these units are connected to form a three dimensional network. The most noteworthy of these angles is Si-O-Si, since it describes the connectivity of two SiO_4 tetrahedra. The average Si-O-Si bond angle (Figure 5.1.1.1.3.-inset) was found to be 153° with a FWHM of 28.5° and 154° with a FWHM of 14° for the two-body (dashed) and three-body (solid) simulated glasses, respectively. Based on neutron diffraction experiments [139], the Si-O-Si angle has a broad distribution between 120° to 180°, with the maximum extending from 144° to 156°. The broad distribution for $\phi_{Si\text{-}O\text{-}Si}$ is due to the introduction of randomness incurred by the typical disordered arrangement of corner-sharing tetrahedra [21].

The peak positions, peak widths and average coordination numbers for all atomic pairs, generated by the two- and three-body potential models, are listed in Table 5.1.1.1.1. The O-O and Si-Si distribution functions for both the two- and three-body glasses agreed well with reported experimental results [23,30,140]. The average interionic distance for the oxygen-oxygen pair was found to be 2.60 Å with a FWHM of 0.18 Å and 2.63 Å with a FWHM of 0.25 Å for the two- and three-body glasses, respectively. The average number of oxygen neighbours was found to be 4.03 for the two-body glass and 6.15 for the three-body glass, using a cutoff radius of 3.2 Å for both glasses. The results for the simulated glasses are in good agreement with neutron diffraction data obtained by Johnston et al. [140] for the O-O interionic distance, however, the average coordination number obtained for the two-body glass was found to be low. The O-O PDF of the three-body glass shows a small shoulder at 2.40 Å, suggesting the possibility of edge-sharing oxygens. This effect of edge-sharing has been reported previously in other studies [141] and arises due to the addition of modifiers (such as lead) in the silicate

network. In contrast, there is no shoulder present in the first O-O peak of the PDF for the two-body simulated glass, which could explain the narrower PDF peak and smaller FWHM value. The first peak in the silicon-silicon PDFs returned to a null value indicating a well-defined first coordination shell. The Si-Si interionic distance was found to be 3.10 Å and 3.18 Å with peak widths of 0.22 Å and 0.16 Å, for the two- and three-body glasses, respectively. The average number of silicon neighbours was found to be 2.20 for the two-body glass and 4.03 for the three-body glass (see Table 5.1.1.1.) Mozzi and Warren [21] report a Si-Si interionic distance of 3.12 Å, and an average coordination of approximately 4.0 nearest silicon neighbours.

Table 5.1.1.1.1.

Nearest neighbour distances and coordination numbers for undoped $PbO{\cdot}SiO_2$

Atomic Pair	First peak maxima (Å)		FWHM (Å)		Coordination* (N)	
	2-body	3-body	2-body	3-body	2-body	3-body
O-O	2.60	2.65	0.18	0.25	4.03(3.2)	6.15(3.2)
Si-O	1.60	1.62	0.13	0.08	4.00(2.1)	4.00(2.1)
Pb-O	2.40	2.43	0.41	0.19	5.78(3.2)	5.72(3.2)
Si-Si	3.10	3.18	0.22	0.16	2.20(3.5)	4.03(3.5)
Pb-Si	3.30	3.20				
	3.45	3.70	1.02	0.78	4.65(4.2)	3.21(4.2)
Pb-Pb	3.80	3.50	0.93	0.68	5.86(4.8)	8.98(4.8)

*Number in parentheses refers to the distance (in Å) at which the average coordination number was calculated.

The short range environment of the silicon ions was analyzed by identifying the different oxygen species present in the glass: bridging oxygens (BO), non-bridging oxygens (NBO) and non-silicate anions (NSA). For the purpose of this discussion, a bridging oxygen is bonded to two silicons, a non-bridging or non-bonding oxygen is bonded to one silicon and one lead, and a non-silicate anion is not connected to the silicate network. Results from the simulated models are presented in Table 5.1.1.1.2. The calculation is performed by counting the types of oxygens present within a Si-O coordination sphere of 2.1Å.

Table 5.1.1.1.2.

Types of oxygens (%) present within the first Si^{4+} coordination shell

Simulated Glass	BO (%)	NBO (%)	NSA (%)
Two-body	36.64	60.0	3.36
Three-body	50.33	33.33	16.34

Hannon et al. [142] have devised a scheme for alkali silicate glasses of composition $SiO_2 \cdot x(M_2O)$ to calculate the fraction of oxygens which are NBOs using the following formula, $f_{NBO} = 2x / (2 + x)$. Employing this formula to the simulated $PbOSiO_2$ glasses, and using x=0.5 for a 50 mole percent PbO composition (x=1 for a 50mol% M_2O), the fraction of NBO's (f_{NBO}) was found to be 0.33 which is in excellent agreement with the simulation results of the three-body glass (33.33%). Smets and Lommen [143] report a value of 40.0 ± 3.0% for the BO/ΣO (ratio between the number of BO and the total

number of oxygens) for a lead metasilicate glass studied using X-ray photoelectron spectroscopy.

In order to shed some light on this discrepancy, the distribution of Q_i species was determined in order to identify the types of bonded silicons for each individual oxygen atom. The Q_i species describe the concentration of tetrahedra, Q, with i bridging species. This labelling system was proposed by Lippmaa et al. [144] to characterize the silicon environment in a wide range of silicate minerals. The bridging oxygens are in the range from 0 to 4, where the Q_0 contains only non-bridging oxygens around an Si, and Q_4 represents four bridging oxygen species and no non-bridging species. In general, there are two types of distributions expected for silicate glasses, binary and statistical. In the case of a binary distribution, there is a maximum of two Q species present for any given composition. This type of distribution is believed to arise from the repulsion of NBO's which are randomly distributed in the glass. A statistical distribution is based upon Zachariasen's random network model [9], which implies that several different Q species may be present in the glass. In a magic angle spinning NMR (MAS-NMR) experiment, Dupree et al. [40] investigated the local environment of the ^{29}Si isotope of various $xPbO{\cdot}(1\text{-}x)SiO_2$ glasses. Analysis of the NMR spectra allowed the authors to suggest that the local environment around silicon is dependent upon the concentration of lead ions in the glass. In order to compare the results of the simulated glass to the experimental glass, only the experimental 48 mol% lead silicate glass will be discussed (see Table 5.1.1.1.3.). The Q_i speciation for the two and three-body simulated glasses as well as the predicted distributions calculated by Dupree et al. [40] are presented in Table 5.1.1.1.3.

Table 5.1.1.1.3.

Simulated and predicted Q_i distribution for undoped $PbO\text{-}SiO_2$ glass

	Q_0	Q_1	Q_2	Q_3	Q_4
Predicted distributions					
Binary model (%)			84.5	15.4	
Statistical model (%)	5	21	37	27	9
Simulated glass					
Two body (%)	2.28	19.05	41.76	30.36	6.55
Three-body (%)	2.4	8.6	20.7	34.7	33.6

Dupree et al. [40] were not able to fit their results to either the binary or statistical model. Using a four Gaussian fit, the authors obtained a skewed statistical distribution with unexpectedly high Q_1 species. A calculation of the BO/ΣO ratios for the experimental and predicted results yields a value of 28.10 and 34.55%, respectively, for a glass composition of 48 mol% PbO. The results presented in Table 5.1.1.1.3. show that the two-body simulated glass is in good agreement with the predicted statistical Qi distribution, whereas the three-body simulated glass does not agree with either of the predicted models but shows a statistical distribution with predominately Q_3 and Q_4 species. It is important to note that there is a substantial difference between the results derived from the experiments of Dupree et al. [40] (BO/ΣO =28%) and those by Smets and Lomman [143] (BO/ΣO =40%). Oddly enough, the simulated two-body glass agrees well with the predicted Q_i distributions of Dupree et al. [40] and the BO/ΣO obtained by Smets and Lomman [143]. Experimental data from an NMR experiment of lead silicate glass by

Fujiu and Ogino [32] offers a plausible explanation for the above discrepancies as well as for the results observed for the three-body simulated glass. The authors found that at concentrations between 50-60 mol% PbO the three dimensional SiO_2 network remains intact and the dominance of monosilicate tetrahedra, proposed by Zachariasen's theory for this composition range, are not found. This phenomenon is explained by assuming that a certain number of PbO_2 groups, which at higher lead concentrations act as network formers, are interconnected with SiO_4 tetrahedra. In accordance with the previous assumption, the high percentage of Q_3 and Q_4 species found in the three-body simulated model suggests the presence of two distinct networks in the glass. Due to the lack of a multibody Pb-O interaction term, the two-body potential model is not as sensitive and thus is not able to differentiate between the two networks. Smets and Lomman [143] also report that at 50 mol% PbO, it was difficult to describe the glass using the proposed models which calculate the $BO/\Sigma O$ ratio. They found that in glasses with less than 50 mol% PbO, the introduction of PbO results in the depolymerization of the silica network, but any further addition of PbO has only a moderate effect on the stability of the metasilicate network. At PbO concentrations greater than 50 mol%, the number of BO oxygens decreases more rapidly as a function of concentration, indicating that the metasilicate rings and chains are not stable at high lead contents.

In to order quantify the aforementioned results further, the oxygen atoms bonded to individual silicons atoms were examined with respect to the lead network (that is, at lead-oxygen cutoff distance of 2.8 Å) and the results are given in Table 5.1.1.1.4.

Table 5.1.1.1.4.

Percent speciation of oxygen in the first Si^{4+} coordination shell with respect to the lead network

Simulated Glass	$n_{Pb}=0$	$n_{Pb}=1$	$n_{Pb}=2$	$n_{Pb}=3$	$n_{Pb}=4$	$n_{Pb}=5$	$n_{Pb}>5$
Two-body	46.67	18.08	27.56	7.62	0.07	0.00	0.00
Three-body	61.57	15.79	11.54	10.33	0.74	0.03	0.00

Table 5.1.1.1.4. shows that approximately 47% of the oxygens bonded to silicons are free of lead neighbours in the two body glass, while 62% was calculated for the three-body glass. The high percentage of $n_{Pb}=0$ in the three-body simulated glass confirms the presence of two distinct regions in the glass, a lead-rich region and a silicon rich region. The two-body glass also shows a relatively high percentage of $n_{Pb}=0$, but a significant percentage of $n_{Pb}=2$ is also present indicating that approximately 28% of the oxygens bonded to silicons have two lead neighbours. This result is in good agreement with the predominance of Q_2 species and implies that in the two-body simulated glass the lead ions are interconnected with the SiO_4 tetrahedral chains acting as typical modifiers, and do not appear to be forming the secondary network observed in the three-body simulated glass. Since the above calculation involves the examination of the oxygens bonded to silicon ions, it is expected that results for $n_{Pb}=O$ will be in good agreement with the number of BO oxygens reported in Table 5.1.1.1.2. Any discrepancies that exist between the two sets of values are accounted for by the larger cutoff distance used (2.8 Å versus 2.1 Å) in the latter calculations. Figure 5.1.1.1.4a. illustrates the presence of the two distinct networks in the three-body simulated glass. Figure 5.1.1.1.4b. shows the lead ions interconnected within the silicate network acting as typical modifier ions.

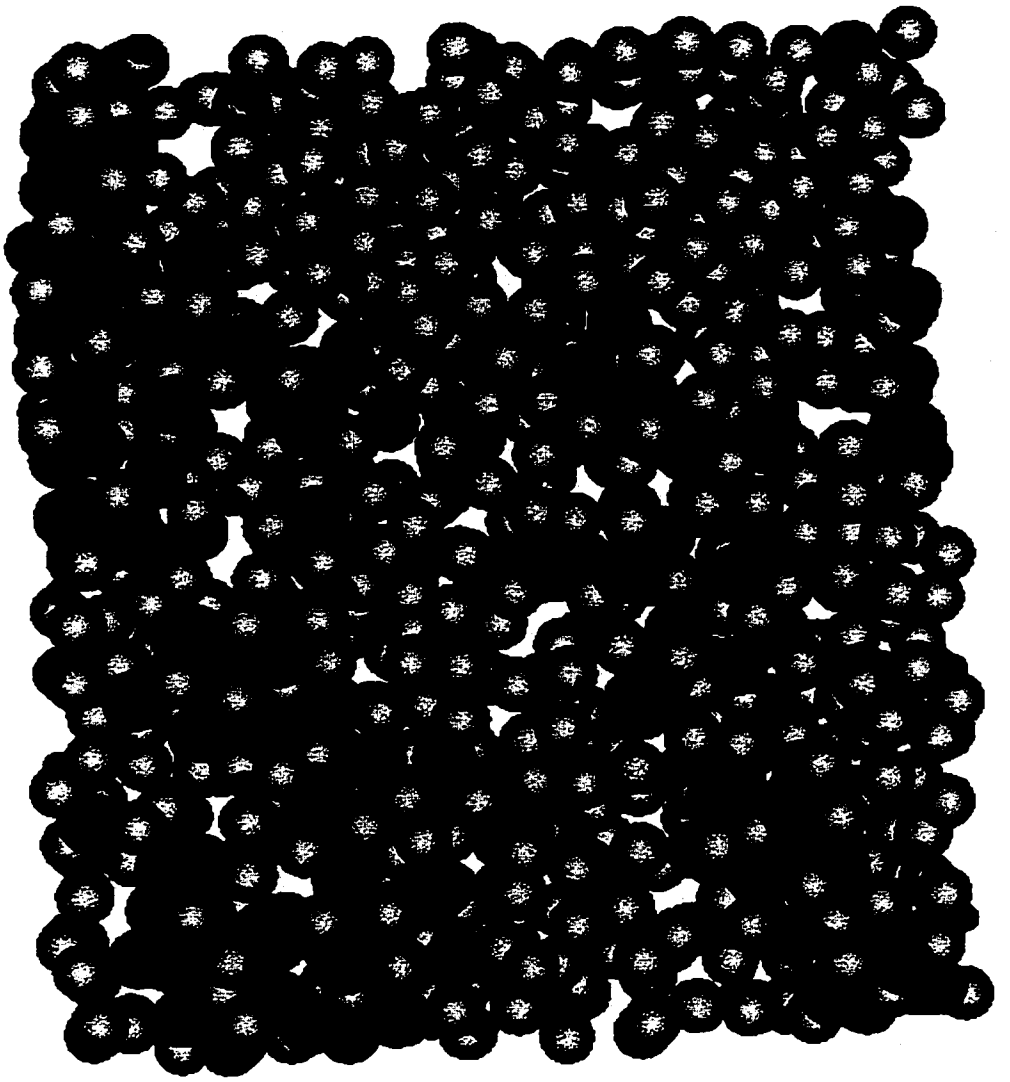

Figure 5.1.1.1.4a. Computer graphics of a slice (xy) of the two distinct networks in the three-body simulated lead silicate glass. The red spheres represent the lead ions, the black spheres represent the silicon ions, and blue-gray spheres represent the oxygen ions.

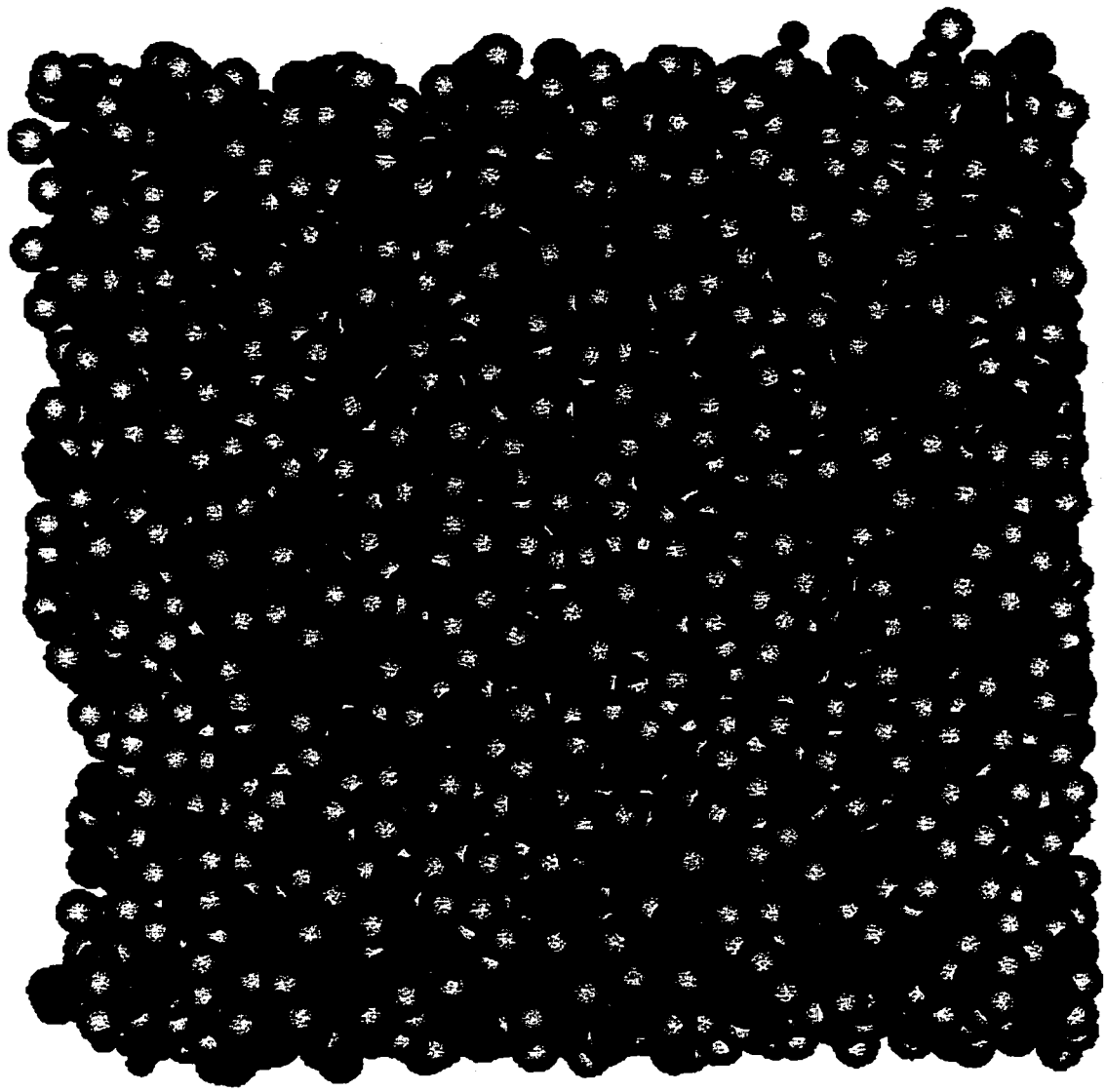

Figure 5.1.1.1.4b. Computer graphics of a slice (xy) of the two-body simulated lead silicate glass. The lead ions (red spheres) are behaving as typical cation modifiers. The black spheres represent the silicon ions and the blue-gray spheres represent the oxygen

A subsequent step in understanding and examining the environment of the silicon ions in the glass is to calculate the distribution of ring sizes. A ring of size *N* contains *N*-silicons (or *N*-tetrahedra). The oxygens, which connect the tetrahedra together in a ring, are all bonding oxygens. The two-body simulated glass is dominated by the presence of five-membered rings which is typical for glasses, whereas the three-body glass contains five-, six- and seven-membered rings which are found in approximately equal proportion. As shown by Rino et al. [145], in the larger rings, the peak position in the O-Si-O bond angle distributions are very close to 109° indicating that the larger rings consist of nearly perfect tetrahedra. The occurrence of larger ring structures in the three-body glass compared to the two-body glass is indicative of a longer range order. This is probably due to the fact that in the two-body glass the lead ions behave more as traditional modifiers and tend to depolymerize the silicate network to a greater extent. Moreover, it was found that for the two-body glass, the silicate network was comprised of a large number of chains connected to the five-membered rings. Less than 20% of the two-body glass and 30% of the three-body glass were comprised of small rings. Two-membered rings are formed by edge-sharing tetrahedra and this will be discussed in greater detail with respect to the lead network. The low percentage of three-membered rings in both of the simulated glasses is to due the fact that the Si-O-Si bond angle (Figure 5.1.1.1.3.-inset) is strained from the dihedral angle of 154° to 130° resulting in a less favorable structure. In contrast, rings of four silicon ions induce little strain and are formed in significantly higher proportion in both the two- and three-body simulated lead silicate glasses.

The present model for both the two- and three-body lead silicate glasses provides a detailed quantification of the silicate backbone, which is in good agreement with experimental data.

(b) The lead environment

Figure 5.1.1.1.5a. and Figure 5.1.1.1.5b. show the PDFs and CDFs for the lead-oxygen atomic pair. The PDF and CDF for the two-body simulated glass are represented by the dashed curves and those for the three-body simulated glass are represented by the solid curves.

As reported in Table 5.1.1.1.1., the average Pb-O interionic distance for the two-body glass was found to be 2.40 Å with a FWHM of 0.41 Å and 2.43 Å with a FWHM of 0.19 Å for the three-body glass. These results are in good agreement with experimental results obtained by pulse neutron scattering [23] and X-ray diffraction data [30,35] for lead metasilicate glass.

The PDFs (Figure 5.1.1.15a) do not return to a null value after the first maximum indicating that there is no clear distinction between the first and second coordination shell. Inclusion of the three-body interaction term to the Pb-O pair has resulted in a much narrower distribution of the first peak, as can be seen from the PDF (solid curve) and the reduction of the FWHM (from 0.41 Å in two-body to 0.19 Å in the three-body). At high lead-oxide concentrations the Pb^{2+} ions partake in the glass-forming network, which results in a much narrower distribution in the local environments of the lead ions [25]. The average coordination of lead, obtained by the extrapolation of the CDF at a cutoff distance of 3.2 Å for both the two and three body simulated glasses were found to be 5.78 and 5.72, respectively. It is important to mention at this point in the discussion, that the inclusion of a three-body term into the potential function optimizes the interionic distances without altering the overall structure. This fact was illustrated (Section 5.1.1.1 (a)) with respect to the Si-O interionic pair and has also been observed for Pb-O.

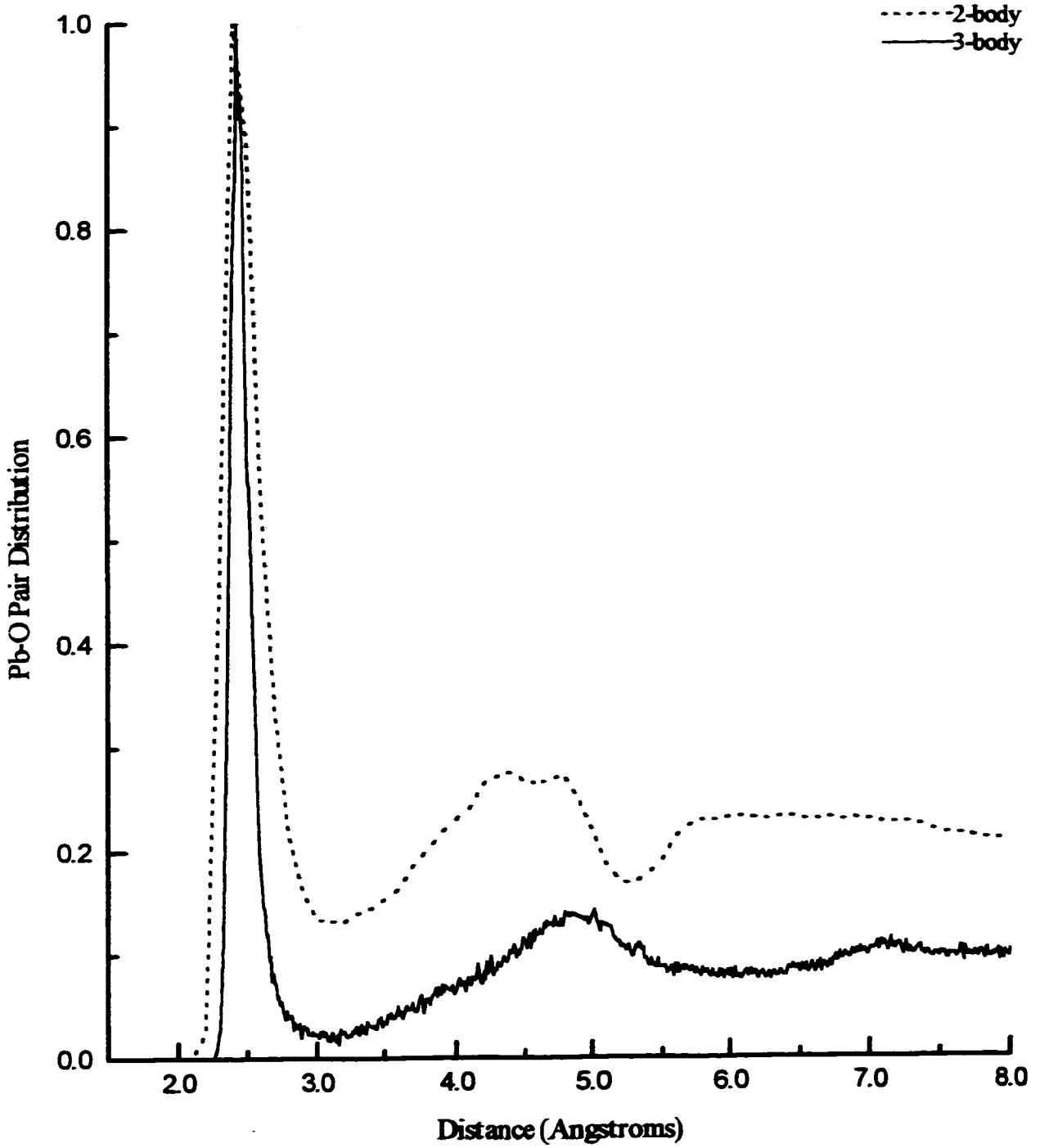

Figure 5.1.1.1.5a. Pair distribution functions of the 2-body (dashed) and 3-body (solid) Pb-O interionic pair for the undoped $PbO{\cdot}SiO_2$ simulated glasses.

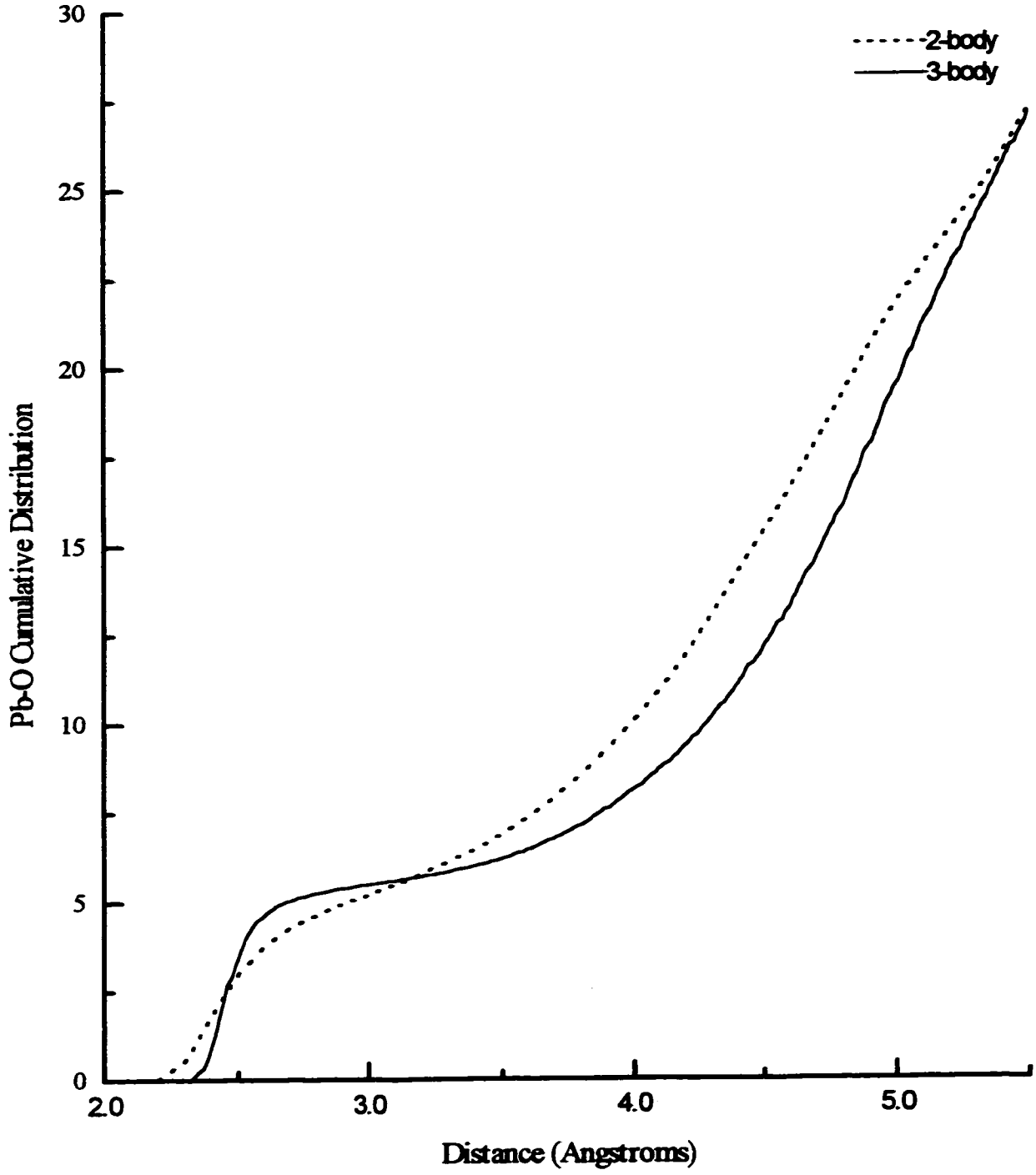

Figure 5.1.1.1.5b. Cumulative distribution functions of the 2-body (dashed) and 3-body (solid) Pb-O interionic pair for the undoped $PbO{\cdot}SiO_2$ simulated glasses.

In comparison, results for both the two- and three-body of the simulated lead silicate glasses agree well with the average structural values calculated for the alamosite crystal [135]. The average coordination of Pb in alamosite is 3.67 at a cutoff radius of 2.8 Å and 6.67 at a cutoff radius of 3.4 Å. The average interionic distance for the first coordinating shell of four oxygens is 2.39 Å with an additional two oxygens present at 3.19 Å. Lottici et al. [146] performed EXAFS and Raman studies on a variety of lead silicate glasses ($(PbO)_x \cdot SiO_2$) and reported an average Pb-O coordination number of 3-4 in $PbO \cdot SiO_2$. Any difference between the simulated and the experimental values is due to the fact that there is no clear distinction between the first and second coordination shell thus, the choice of a cutoff radius becomes somewhat ambiguous. The experimental data referenced above, with the exception of the results reported by Imaoka et al. [35] were fitted assuming a first coordination shell similar to that found for a PbO_4 tetragonal pyramidal arrangement. In contrast, Imaoka et al. [35] assumed that for lead silicate glass in the composition range of 50-66.6 mol% PbO only PbO_3 pyramidal structures existed which are interconnected to silicate anions. Hence, there is an increase in the number of oxygens surrounding individual lead ions. It is therefore important for both modelling and experimental techniques to indicate the cutoff radius chosen and in the case of the latter, the spatial extent of the fitting procedure used.

The Pb-Pb pair distribution functions were found to be broad and asymmetric for both the two- and three-body simulated glasses. The Pb-Pb interionic distances were 3.80 Å with a FWHM of 0.93 Å and 3.50 Å with a FWHM of 0.68 Å, for the two- and three-body simulated glasses, respectively (see Table 5.1.1.1.1). Average lead-lead coordination numbers of 5.86 and 8.98 were found at a cutoff distance of 4.8 Å for the

two- and three-body simulated glasses, respectively. The values reported for the Pb-Pb interionic distance, in both the two- and three-body simulated glasses, are in good agreement with those reported by Mydlar et al. [30] who performed an X-ray diffraction study of $PbSiO_3$ glass. The authors fitted the experimental radial distribution function with the relevant atomic pairs. For the first Pb–Pb interactions a total of three Gaussian distributions were identified at 3.6Å, 4.15Å and 4.8Å, which correspond to the contribution of one, two, and one lead neighbours, respectively. Thus, a total of four lead neighbours at an interionic bond distance of 4.8Å was reported for the experimental model. In the present MD model for the two-body glass a lead ion is surrounded by 5.86 lead neighbours at a distance of 4.8Å, whereas the three-body model shows 8.98 nearest lead neighbours at the same distance. The high lead-lead coordination in the three-body simulated model is due to the lead-rich regions as a result of the secondary network made up of the modifier lead cations linked by NBO atoms [30,147]. The asymmetry present in the Pb–Pb first neighbour distribution, may be attributed to a differentiation between intra-chain lead-lead interactions as opposed to inter-chain lead-lead interactions. Similar behavior has been previously observed in the zinc-zinc PDF calculated from the simulated model of a zinc trisilicate glass [141].

The Pb-Si first coordination peak was found to be at a maximum at 3.45 Å (FWHM=1.02 Å) in the two-body model and 3.70 Å (FWHM= 0.78 Å) for the three-body model. A small shoulder is present on both peaks at 3.30 Å and 3.20 Å, for the two- and three-body glasses, respectively. An average coordination number of 4.65 was calculated for the two-body glass and 3.21 for the three-body glass at a cutoff radius of 4.2 Å. At a cutoff distance of 4.2 Å, the average coordination number for the three lead sites in the alamosite crystal is equal to 5.0. The results from the two-body glass are in good

agreement with the crystal, while those for the three-body glass differ significantly. The difference between the three-body simulated model and the crystal may be attributed to the lead-rich and silicon-rich regions in the glass. These distinct regions would reduce the number of silicons surrounding the lead ion in the first Pb-Si coordination shell.

In order to investigate further the secondary lead network, a bond angle distribution analysis was performed to determine the connectivity of the lead units. Figure 5.1.1.1.6. illustrates the distribution of coordination number in percent for the first coordination shell of Pb, using the two- and three-body potential models.

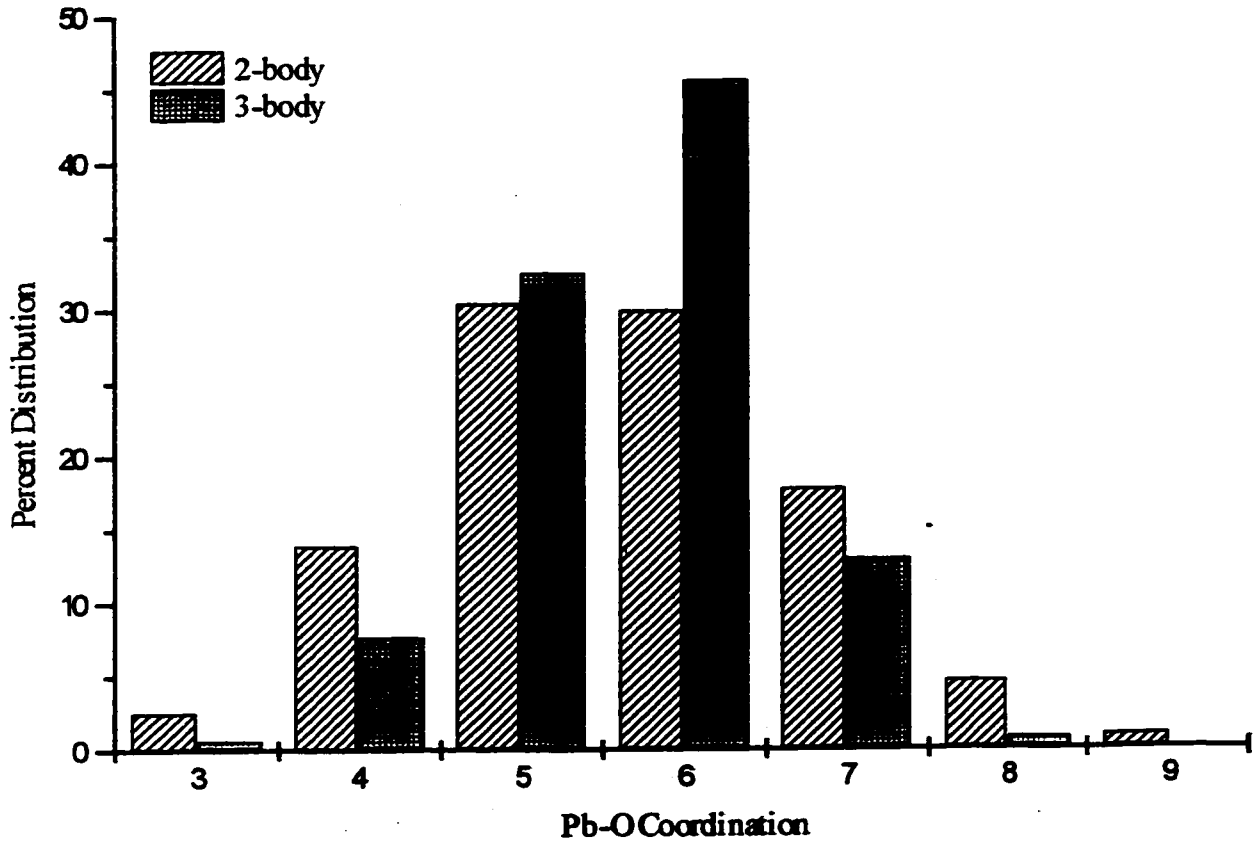

Figure 5.1.1.1.6. Histogram of the percent coordination distribution for the Pb-O ionic pair in the first coordination shell (cutoff radius = 3.2Å) for the two-body (dashed) and three-body (gray solid) simulated lead silicate glass.

The O-Pb-O bond angle distribution for the two-body simulated glass has three distinct peak at 55°, 87° and 127°. The three-body model also shows three distinct peaks at 57°, 90° and a broader less intense distribution at 135°. The major distribution for both the two- and three-body simulated glasses occurs at approximately 90° and can be explained by a sixfold coordinated octahedral type structure and the four coordinated species, which are probably PbO_3 pyramidal structures. Imaoka et al. [35] have postulated, using X-ray diffraction, that at PbO concentrations between 50-66.6 mol%, only PbO_3 pyramidal units are present in $PbO{\cdot}SiO_2$ glass. The bond angle distribution found at 127° and 135°, for the two- and three-body glasses, respectively, may be related to the five coordinated lead species (Figure 5.1.1.1.6.). The seven coordinated Pb species may have the following structures: a pentagonal bipyramid, a capped octahedron or a capped trigonal prism. All three of the above mentioned geometries would have bond angles in the range of the O-Pb-O and Pb-O-Pb distributions and it is therefore difficult to ascertain exactly which geometry is present. The Pb-O-Pb bond angle distribution for the two- and three-body simulated glasses show two peaks, one at 87° and 92° and the other at 121° and 160°, for the two-and three-body models, respectively. The major distribution for both glasses occurs at the smaller angles (87° and 92°) and the difference in the two structures could be due to the large percentage of five membered ring structures found in the two-body glass which may account for the peak seen at 121°. The Pb-O-Pb distribution found for the three-body model is typical of edge-sharing in glasses. In order to examine if edge sharing is present in the simulated glass, the Pb-O-Pb-O and Si-O-Pb-O linkages were calculated. As stated previously in the discussion of the oxygen-oxygen atomic pair, the shortened O-O bond at 2.40Å, in the three-body model, is an indication of edge-sharing in

the glass. The first peak maxima in the Pb-Si and Pb-Pb pair distribution functions are comprised of several local maxima and thus the lead ion can occupy a variety of environments in the glass. Similar results were observed by Rosenthal et al. [141] in a molecular dynamics study of amorphous zinc silicate. The only indication of edge-sharing in the two-body simulated glass is the shoulder at 87° in the Pb-O-Pb bond angle distribution, however, no further evidence in the glass structure was found to support this possibility.

The ability of an ion to behave as a network former depends upon the degree of covalency of the bond, the polarizability and the field strength of the ion. In order to quantify the strength of a bond, Dietzel [148] introduced the calculation of the field strength of an ion. Lead has a field strength in the range of 0.34-1.03 which classifies lead as having the ability to act as both a network modifier (< 0.35) and a network former (1 to 2). Therefore, the partial covalency of the Pb-O bond and the calculated field strength value of 1.03 enable the lead ions to participate in the glass forming network at high lead-oxide concentrations. This result in conjunction with those discussed previously is conclusive evidence for the existence of the secondary lead network postulated using the three-body potential model.

Structural features of the simulations of undoped $PbO{\cdot}SiO_2$ glass were found to be in excellent agreement with published experimental results. Nearest neighbour distances and average coordination numbers are in good agreement with those obtained from X-ray and neutron diffraction and EXAFS studies. The silicon coordination was found to be 4.0 and the tetrahedral angle was sharpened in the three-body simulated model compared to the two-body simulated model. It is clear from the PDF and bond-angle distribution functions that the three-body potential increased the local order around the silicon ions by

the well defined tetrahedral units, the improvements to the Si-O-Si bond angle distributions and the lowering of bond defects. In addition, the three-body potential model showed the presence of two networks, which has also been observed experimentally[149]. It can therefore be concluded that the simulated models are a good representation of the structure of $PbO{\cdot}SiO_2$ glass and that the three-body potential model produces a marked improvement over the two-body potential model.

5.1.2. A compositional study of undoped lead silicate glass

The structure of lead silicate glass has been studied extensively using various experimental techniques [23,30,35] as well by molecular dynamics, however, the results remain inconclusive and contradictory. This is due to the fact that these glasses are stable over a wide glass forming range with PbO composition ranging up to 95 mol% [23]. The silicon-oxygen three-dimensional network is broken up by the addition of most alkali or alkaline metal cations, which act as network modifiers. Lead is a network modifier yet it has been recognized for its glass forming capabilities, which are attributed to the high polarizability of divalent lead. At PbO concentrations below 30 mol%, lead behaves as a classical modifier. However, at higher concentrations, PbO is more of a network former displaying PbO_3 and PbO_4 structural units. Yamada et al. [23] state that it is the polarizability of Pb^{2+} which causes an asymmetric coordination of oxygen atoms around the lead atoms, leading to the chain structure observed in lead glasses in the absence of the Si-O network. The presence of a secondary lead network has been observed experimentally [149] as well as computationally [41,147] (and this study), however, none of the experimental investigations proposed an unequivocal description of the lead-based

unit. This is in contrast to the traditional network-formers such as silicon, phosphorous or boron, where all experimental investigations present definite results about the first-coordinating shell and the immediate connectivity of the network-former structural unit.

In order to obtain a better description on the effect of the lead ion in silicate glasses, we have employed the three-body potential model, which has been very successful in describing the structure of lead silicate glass (50mol% PbO), to simulate glasses with low and high lead-oxide content. Two glasses with the following composition, $0.22PbO{\cdot}0.78SiO_2$ (22/78) and $0.70PbO{\cdot}0.30SiO_2$ (70/30) were simulated using the three-body potential model described in Section 2.2.2. of this thesis. The results are compared to the aforementioned $0.50PbO{\cdot}0.50SiO_2$ (50/50) glass as well as to experimental data.

The structural parameters for the simulated glasses were derived obtained from the radial distribution functions (RDF), the pair and cumulative distribution functions of the individual atomic pairs as well as the bond angle distribution functions. Table 5.1.2.1. lists the interionic distances and average coordination numbers for the three simulated glasses.

Table 5.1.2.1.

Interionic distances and coordination numbers
for the 22/78, 50/50 and 70/30 glasses

	$22PbO\text{-}78SiO_2$		$50PbO\text{-}50SiO_2$		$70PbO\text{-}30SiO_2$	
Atomic Pair	First peak maxima(Å)	Average* Coord. (N)	First peak maxima(Å)	Average* Coord. (N)	First peak maxima(Å)	Average* Coord. (N)
O-O	2.63	6.3(3.2)	2.65	6.15(3.2)	2.60	7.28(3.2)
Si-O	1.63	3.99(2.1)	1.62	4.00(2.1)	1.62	4.13(2.1)
Pb-O	2.40	3.2(3.2)	2.43	5.72(3.2)	2.42	6.83(3.2)
Si-Si	3.22	4.45(3.2)	3.18	4.03(3.5)	3.14	5.2(3.5)
Pb-Si	3.24		3.20		3.22	5.32(4.2)
	3.84	0.83(4.2)	3.70	3.21(4.2)	3.81	
Pb-Pb	3.42	3.5(4.8)	3.50	8.98(4.8)	3.20	14.0(4.8)

*Number in parentheses refers to the cutoff distance (in Å) at which the average coordination has been calculated.

The RDFs for the three glasses shown in Figure 5.1.2.1. are indicative of the well defined short-range order and the lack of long range order characteristic of glasses. The three curves show a similar distribution for the first peak, which is representative of the Si-O interionic pair. It is with respect to the second peak that the structural difference between the three glasses becomes apparent. The RDF curves for the 50/50 and 70/30 glasses are similar to one another, which suggests a similarity in the arrangement of the lead ions [35]. The difference and similarities in all three glasses will be discussed further by analyzing the individual atomic pair and cumulative distribution functions.

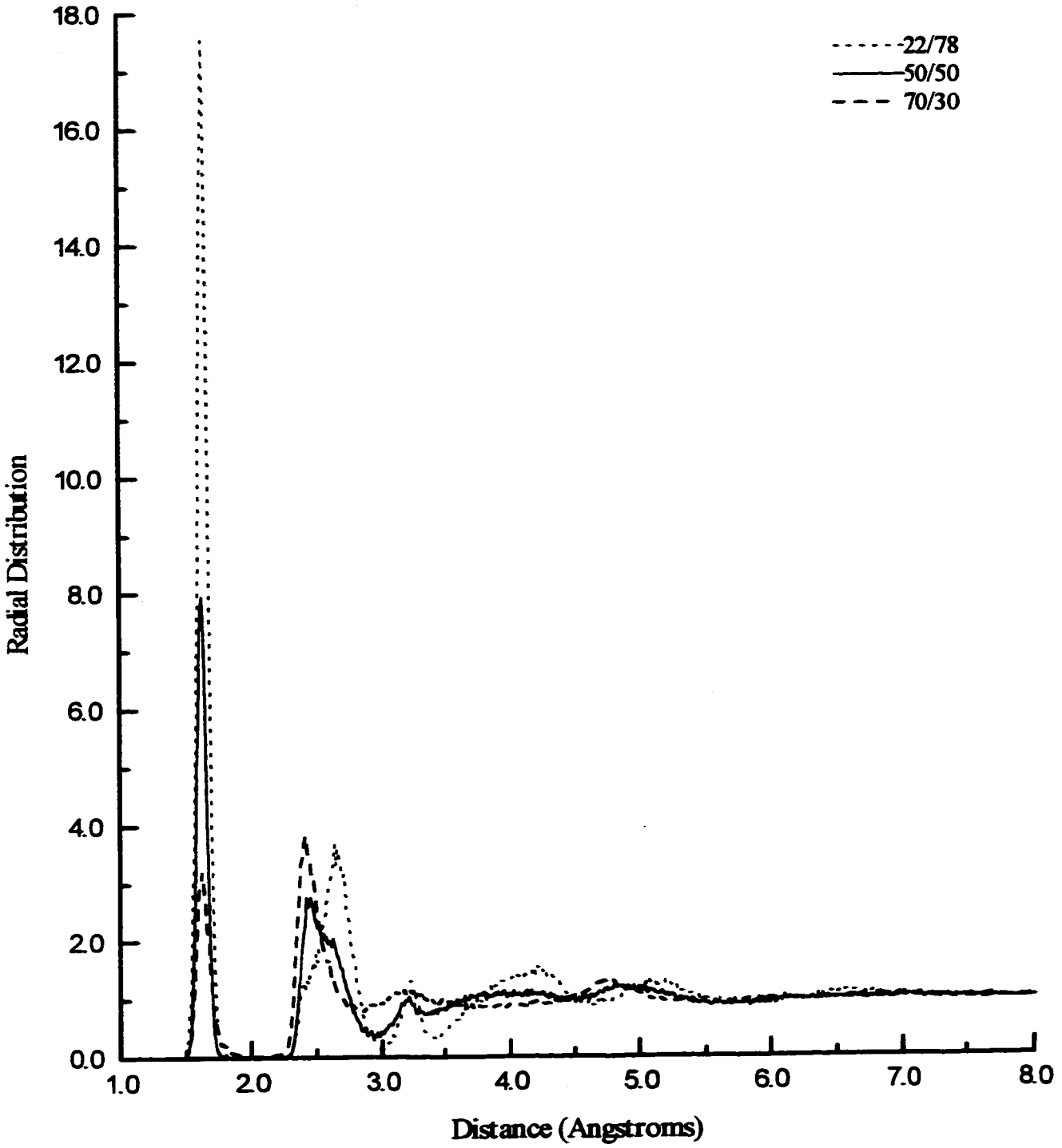

Figure 5.1.2.1. Radial distribution functions of the 22/78 (dotted), 50/50(solid) and 70/30 (dashed) lead silicate glasses.

The Si-O interionic distance (Figure 5.1.2.2.) was found to be 1.63 Å, 1.62 Å and 1.62 Å for the 22/78, 50/50 and 70/30 simulated lead silicate glasses, respectively. The average coordination number, at a cutoff distance of 2.1 Å, was found to be 3.99 for the 22/78 glass, 4.00 for the 50/50 glass and 4.13 for the 70/30 glass. The PDFs all return to a null value indicating a clear distinction between the first and second coordination shell. The fact that the interionic distance and average coordination numbers do not vary significantly from one another suggests that the individual tetrahedral environments are independent of PbO concentration. Similar results were observed experimentally by Yamada et al. [23]. The increase (minor) in coordination of Si in the 70/30 glass represents an increase in odd-coordinated silicon species (16%) [35].

The well-defined short range order of the silicate network is further exemplified by the bond angle distributions. The O-Si-O bond angle was found to be 110°, 109.7° and 103.6° for the 22/78, 50/50 and 70/30 simulated glasses, respectively. The 22/78 and 50/50 glasses have a narrow distribution with a FWHM of 5.5° and 6.0°, respectively, while the 70/30 glass has a broader distribution with a FWHM of 18°. In contrast to the other two glasses, the O-Si-O bond angle distribution in the 70/30 glass has a shoulder at approximately 90°, which is consistent with the greater percentage of odd coordinated silicons (usually 5 and/or 6 coordinated) present in the high lead-oxide glass. The Si-O-Si bond angle distribution has a range from 120° to 180° in both the 22/78 and 50/50 with an average angle of 159° and 154°, respectively. The 70/30 glass was found to have a significantly smaller bond angle in the range of 60° to 180° with an average angle at 96°. The smaller angle in the 70/30 glass is attributed to the significant increase in lead-rich regions surrounding the silicate network, compared to that of the 50/50 glass.

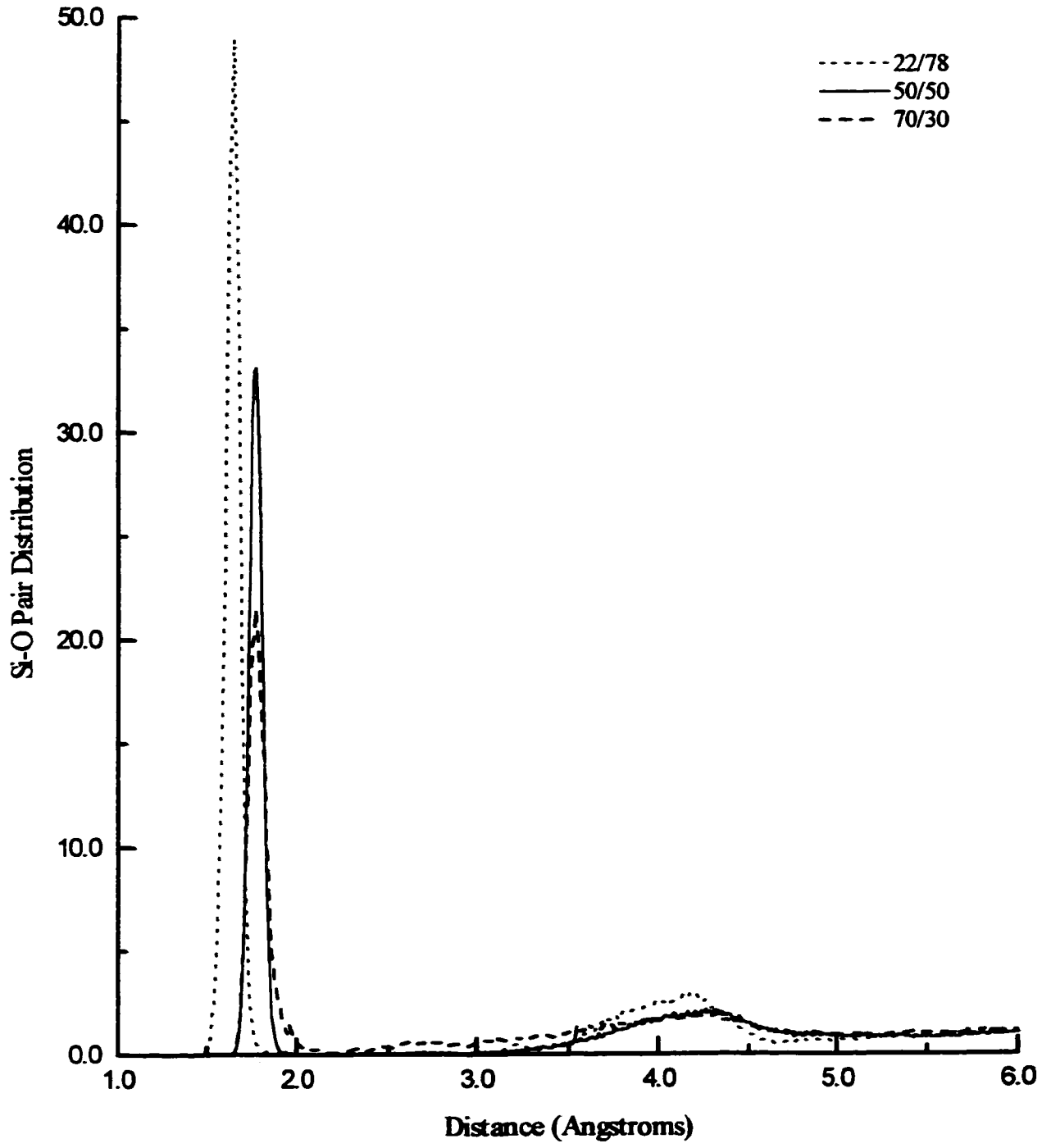

Figure 5.1.2.2. Pair distribution functions for the Si-O interionic pair of the 22/78 (dotted), 50/50(solid) and 70/30 (dashed) lead silicate glasses.

The average Pb-O interionic distance was found to be 2.40 Å, 2.43 Å and 2.45 Å for the 22/78, 50/50 and 70/30 glasses, respectively (see Table 5.1.2.1.). At a cutoff radius of 3.2 Å, the average number of oxygen neighbours to lead was found to be 3.2 for the 22/78 glass, 5.72 for the 50/50 glass and 6.83 for the 70/30 glass. There are various experimental studies [23,35,39] which report average Pb coordination numbers of 3-4 in lead silicate glasses, independent of the PbO concentration. The models all fit the experimental data assuming a first coordination shell identical to that found for a PbO_4 tetragonal pyramidal arrangement (corresponds to a cutoff distance of about 2.5 Å). The average Pb-O interionic distance was found to be 2.43 Å and thus such a short cutoff imposes certain constraints on the lead environment. In agreement, Mydlar et al. [30] report that the lead ion is coordinated by two closer atoms at 2.2 Å and two more oxygens at both 2.53 Å and 2.8 Å for the lead metasilicate glass (50/50). This distribution is similar to that found in the alamosite (see Section 5.1.1. for a detailed discussion). For the 22/78 the structural parameters are in good agreement with those reported by Yamada et al. [23] using neutron diffraction techniques. Morikawa et al. [33] calculated an average coordination of 4.5 for $2PbO{\cdot}SiO_2$ (66 mol% PbO). However, they stated that their model underestimated the coordination and the distribution is probably similar to that found in the corresponding crystal, that is, within a coordination sphere of 3.0 Å the Pb ions are coordinated by 4 to 6 oxygen neighbours. The average coordination number in the 70/30 glass was found to be slightly higher (6.83) than the value reported by Morikawa et al. [33]. This increase in coordination may be due to the fact that the glass is separated into lead-rich and silicon-rich regions at concentrations greater than 50 mol% PbO. This would result in the lead ions sharing oxygens within the same coordination sphere (3.2 Å). The modifier/former effect of PbO for the three lead silicate glasses in this study are in

agreement with the results reported by Wang et al. [22], however a substantial discrepancy was found with respect to the Pb-O coordinations. In an XPS study of lead silicate glasses of different compositions, the authors report that below 40 mol%, PbO plays the role of a glass modifier and gradually transforms towards a glass former as the concentration of PbO increases. The authors also state that at low PbO concentration the Pb-O interaction is completely ionic, however, as the concentration increases to the level where PbO acts more as former, the PbO interaction becomes more covalent. This increase in covalency at high lead-oxide concentrations is attributed to the high polarizability of divalent lead. Based on the aforementioned results, the authors postulate that an increase in PbO concentration should result in a decrease in the PbO coordination. At this point, no explanation can be offered for this discrepancy since the present potential model does not take into account "directly" the effect of polarizability.

Montenero et al. [39] have also reported the occurrence of the secondary network structure stating that "the compositional changes produce a different distribution of chains, but the short-range order within the chains is preserved". This point can be illustrated further by examining the Pb-Pb environments. The Pb-Pb interionic distance was found to be 3.42 Å for the 22/78 glass, 3.50 Å for the 50/50 glass and 3.20 Å for the 70/30 glass (see Table 5.1.2.1.). The values reported here are in good agreement with the results obtained by Mydlar et al. [30] for the $PbO{\cdot}SiO_2$ glass and the $2PbO{\cdot}SiO_2$ glass. The trends in the interionic distances can be explained by examining the distribution of the lead ions in the glass. In the 22/78 glass, the lead ions are behaving as traditional modifiers and thus are randomly distributed throughout the glass structure. As the concentration increases, the lead ions begin to form the secondary structure and at high Pb concentration (70 mol% PbO) the Pb-Pb interionic distance is shortened due to spatial constraints. The

average lead-lead coordination number, at a cutoff radius of 4.8 Å, was found to be 3.5, 8.98 and 14.4 for the 22/78, 50/50 and 70/30 simulated glasses (see Table 5.1.2.1). The 22/78 simulated glass is in good agreement with experimental data for an alkaline modifier in silicate glass [23]. Similar results were reported for calcium silicate glasses [150]. At low lead-oxide concentration, the behavior of lead ions is similar to that of the calcium ions in silicate glasses [150]. In the case of the high lead-oxide glasses, the lead-lead coordination is high and can only be explained by the presence of the lead-rich regions.

In order to examine further the environment of the lead ions, a speciation of the oxygen types surrounding individual lead ions with respect to the silicate network (Table 5.1.2.2a) and the lead network (Table 5.1.2.2b) was performed.

Table 5.1.2.2a.

Percent speciation of oxygen in the first Pb^{2+} coordination shell with respect to the silicate network

Mol% PbO	$n_{Si}=0$ (NSA)	$n_{Si}=1$ (NBO)	$n_{Si}=2$ (BO)	$n_{Si}>2$ (Anomalies)
22	0.8	84.8	14.4	0.0
50	15.5	81.8	2.7	0.0
70	29.4	65.8	4.8	0.0

Table 5.1.2.2b.

Percent speciation of oxygen in the first Si^{4+} coordination shell with respect to the lead network

Mol% PbO	$n_{Pb}=0$	$n_{Pb}=1$	$n_{Pb}=2$	$n_{Pb}=3$	$n_{Pb}=4$	$n_{Pb}>4$
22	83.9	9.8	6.0	0.3	0.0	0.0
50	61.6	15.8	11.5	10.3	0.7	0.1
70	24.2	24.1	20.0	13.1	12.2	6.4

Table 5.1.2.2a. shows that approximately 30% of oxygens bonded to lead are free of silicon neighbours in the 70/30 glass, whereas only 1% was calculated for the 22/78 glass. As the concentration of PbO increases, the presence of the two networks becomes more evident. This can be quantified by the number of NBOs ($n_{Si}=1$) present in each of the glasses. For the 22 mol% PbO, lead is behaving as a classical modifier and accordingly shows the highest percentage of NBO species. The number of NBOs decreases with increasing Pb concentration due to the formation of the secondary lead network. This effect is most evident in the 70/30 glass where the increase in the lead rich regions results in an increase in the connectivity between the lead and silicate networks thus decreasing the number of NBOs. The connectivity between the two networks can be quantified further by examining the environment of the silicons. Table 5.1.2.2b. shows that 84% of oxygens bonded to silicons were found to be free of lead neighbours in the 22/78 glass, decreasing to 62% in the 50/50 glass and to 24% in the 70/30 glass. The significant presence of $n_{Pb}=4$ and $n_{Pb}>4$ species in the 70/30 glass indicates that the lead rich regions are interconnected with the silicon rich regions via bridging oxygens. The connectivity via bridging oxygens can be further exemplified from the Pb-Si pair distribution functions.

The Pb-Si PDF for the 22/78, 50/50 and 70/30 lead silicate glasses are shown in Figure 5.1.2.3. The Pb-Si interionic distances were found to be 3.84 Å with a shoulder present at 3.24Å for the 22/78 glass, 3.70Å with a shoulder present at 3.22Å for the 50/50 glass and 3.21Å with a shoulder present at 3.81 Å for the 70/30 glass.

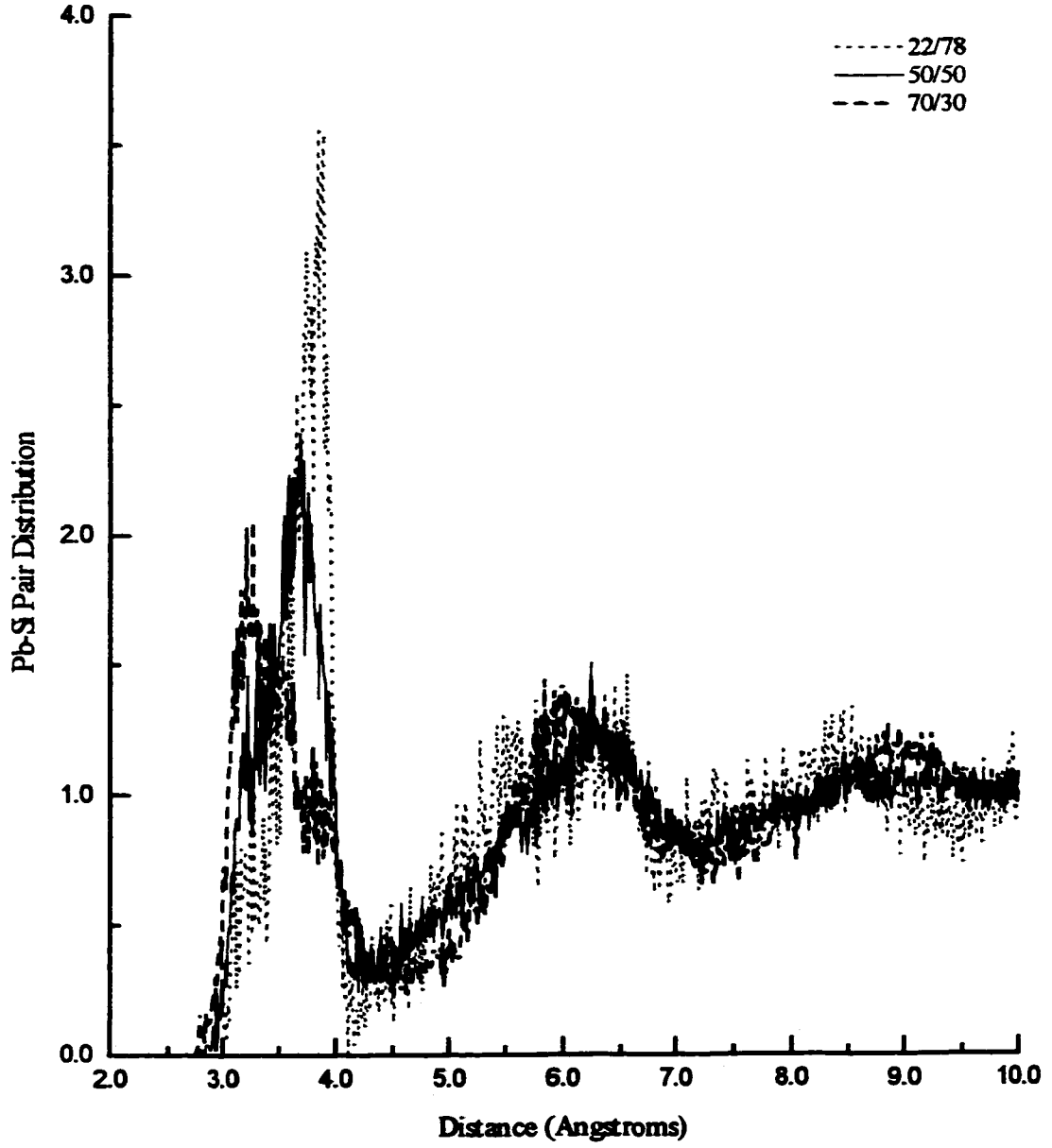

Figure 5.1.2.3. Pair distribution functions for the Pb-Si interionic pair of the 22/78 (dotted), 50/50(solid) and 70/30 (dashed) lead silicate glasses.

Both the 22/78 and 50/50 lead silicate glasses have similar PDFs with the maximum shifted to shorter distances in the 50/50 glass due the presence of the secondary lead network. In the 22/78 glass, the lead ions are behaving as traditional modifiers and are distributed throughout the silicate network, as indicated from the larger Pb-Si interionic distance. In the case of the 70/30 lead silicate glass, the Pb-Si PDF is the mirror image of the other two undoped glasses (22/78 and 50/50) with a first peak maximum at a significant smaller distance (3.22 Å). This decrease in the Pb-Si interionic distance is due to the interconnectivity of the two networks via the bridging oxygens, which has also been observed experimentally [30,33]. Information on the geometrical arrangement of these connecting lead and silicate units can be inferred by examining the bond angle distributions.

In the 22/78 glass, the Pb-O-Pb bond angle distribution shows a major peak at approximately 90° with a shoulder at 114° in good agreement with the observed three and four coordinated structural units present at low lead concentrations. The Pb-O-Si bond angle distribution is indicative of corner-sharing oxygens between the two networks with a broad distribution maximum at 135°. The shoulder at approximately 100° is representative of a small degree of edge-sharing units. The distributions of these two angles are to be expected if the lead ion is acting as a network modifier. In the 50/50 glass, the predominance of edge-sharing oxygens is more apparent. The Pb-O-Pb bond angle distribution shows a maximum at approximately 88° with a small shoulder at 157°. The smaller angle at 88° represents the connectivity of the secondary lead network via edge-sharing oxygens while the shoulder at 157° is characteristic of corner-sharing units. The Pb-O-Si bond angle distribution is broad and is comprised of two local maxima (98°

and 122°), in good agreement with the range of bond angles found for edge-sharing. Similar results were observed by Garofalini [141] in a molecular dynamics study of amorphous zinc silicate. In the 70/30 glass, lead is behaving predominately as a network former and in accordance with the Random Network Theory, the secondary lead network is comprised mainly of corner-sharing oxygens. The Pb-O-Pb bond angle distribution shows a major peak at 80° and a shoulder at 157°. The small angle at 80° is atypical for corner-sharing units, however, is to be expected due to the spatial constraints imposed by the increase in the lead rich regions of the glass. In contrast, the connectivity between the silicate and lead network occurs via edge-sharing oxygens as shown by the maximum at 97° in the Pb-O-Si bond angle distribution.

In conclusion, from the concentration study performed on lead silicate glass it was found that at low PbO concentrations, the lead ion behaves as a traditional modifier with the lead ions distributed throughout the glass and low lead-oxygen coordination. These results were found to be in good agreement with X-ray diffraction studies. As the concentration of lead increases to 50 mol% PbO, the lead ion behaves as both a modifier and a former with the formation of the two distinct networks; the silicate network and the secondary lead network. In the 70/30 glass, the presence of lead rich regions predominates in the glass and the two networks are connected via edge-sharing oxygens. The lead ion is behaving as a network former and an increase in PbO coordination is observed since the lead ions share neighbouring oxygens.

5.1.3. Structure of Eu^{3+}-doped lead silicate glass

Lead containing glasses are extensively used in numerous industrial and technological applications. Because of their high index of refraction, optical applications of such materials have been widespread for several centuries. Recently, high technology applications such as nuclear scintillators and up-conversion laser devices demand a greater understanding and control over various structurally related optical properties. The following section will present a simulated structural model of lead silicate glass, $PbO{\cdot}SiO_2$, containing an optically active species at a typical dopant concentration. The dopant present in the simulated glass is the trivalent lanthanide ion europium, Eu^{3+}. A glass composition of $48\%PbO{\cdot}51\%SiO_2{\cdot}1\%Eu_2O_3$ was simulated using the three-body potential model described in Section 2.2.2. of this thesis. Due to the low number of europium ions present in the 2% Eu^{3+}-doped lead silicate glass (20 Eu^{3+} ions), 10 different configurations at 300K were generated in order to ensure statistical reproducibility. The study of this ternary composition was motivated by the recent observation of substantial room-temperature up-conversion from infrared to visible radiation in Er^{3+} doped and Er^{3+}/Yb^{3+} co-doped $PbSiO_3$ glasses [24].

The general structure of the glass was determined by calculating the radial distribution functions (RDF), the pair (PDF) and cumulative (CDF) distribution functions as well as the bond angle distributions. The RDF for the 2.0% Eu^{3+}-doped lead silicate glass shown in Figure 5.1.3.1. is indicative of the well defined short-range order and lack of long range order characteristic of glasses. The average first coordination shell parameters (peak positions, peak widths, average coordination number of nearest neighbours at given distances) of the atomic pairs found in the 2.0% Eu^{3+}-doped lead silicate glass are listed in Table 5.1.3.1.

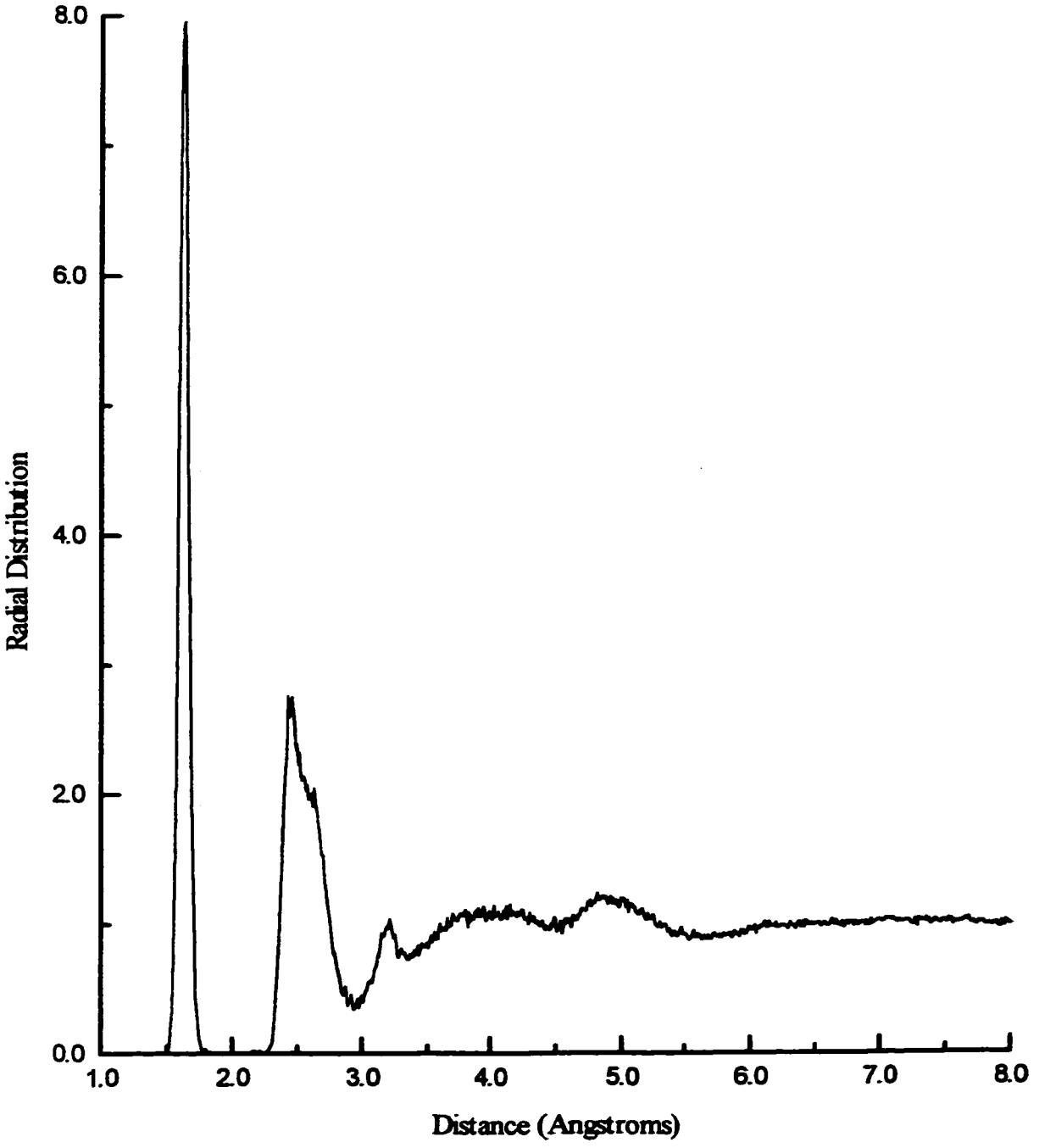

Figure 5.1.3.1. Radial distribution function for 2.0% Eu^{3+}-doped lead silicate glass.

Due to the extensive structural information available in the Eu^{3+}-doped lead silicate glasses, analysis of the general structure of the glass will be divided into two categories: the silicate backbone, the environments of the lead and europium cations.

(i) The silicate backbone

A detailed analysis of the silicate backbone was performed in Sections 5.1.1 and 5.1.2. of this thesis and therefore, in this section, only the interionic distances and average coordination numbers will be discussed to ascertain whether the dopant has any effect.

The average Si-O interatomic distance was found to be 1.62 Å with a full width at half maximum (FWHM) of 0.07 Å. Extrapolation of the CDF curve at the cutoff radius, 2.1 Å, indicated that each silicon ion is tetrahedrally coordinated by 4.00 oxygen ions. The O-Si-O tetrahedral bond angle was found to be 109.7° with a FWHM of 0.06°, which agreed well with experimental findings ranging from 104 -115° and the theoretical calculation of 109.4°. The average Si-O-Si bond angle for the simulated glass was 150° with a FWHM of 14°. The fact that there were very few over or undercoordinated silicons or oxygens present in the simulated glass further justifies the existence of the high degree of local order in the glass.

The O-O and Si-Si distribution functions agreed well with experimental findings. The average interionic distance for the oxygen-oxygen pair was found to be 2.65 Å with a FWHM of 0.28 Å and the average number of oxygen neighbours was found to be 5.5 (Table 5.1.3.1.). The peaks in the silicon-silicon PDF were sharp with the first peak returning a to null value indicating a well defined first coordination shell. The Si-Si interionic distance was determined to be 3.12 Å, having a FWHM of 0.11 Å (Table

5.1.3.1.). Furthermore, the average number of silicon neighbours was found to be 4.1 at a cutoff distance of 3.4 Å.

The present model for the three-body Eu^{3+}-doped lead silicate glass is in good agreement with experimental data [23,30,33] and provides an accurate description of the silicate backbone.

Table 5.1.3.1.

Nearest neighbour distances and coordination numbers for 48% PbO-51%SiO_2-1%Eu_2O_3

Atomic pair	First peak maxima r (Å)	Width of first peak FWHM (Å)	Average Coordination (N)*
O-O	2.65	0.28	5.00 (2.9)
Si-O	1.62	0.07	4.00 (2.1)
Pb-O	2.45	0.14	5.63 (3.2)
Eu-O	2.40	0.07	6.31 (3.2)
Si-Si	3.19	0.11	4.09 (3.4)
Si-Pb	3.2		3.00 (4.2)
	3.7	0.7	
Si-Eu	3.2	0.2	1.80 (4.2)
	3.8	0.3	
Pb-Pb	3.6	1.2	8.00 (4.6)
Pb-Eu	3.5	0.8	8.30 (4.6)

* Number in parentheses refer to distance (in Å) at which the average coordination number has been calculated.

(ii) The environment of the lead and europium cations

The next step in analyzing the glass is to examine the average first coordination shell parameters of the remaining atomic pairs found in the europium doped glass. These parameters, peak positions, peak widths and the average number of nearest-neighbours at a given distance, are presented in Table 5.1.3.1.

Figure's 5.1.3.2.-5.1.3.4. show the PDFs (denoted by 'a') and the CDFs (denoted by 'b') for the lead atomic pairs Pb-O, Pb-Pb, and Pb-Si (solid lines) and the europium atomic pairs, Eu-O, Pb-Eu and Eu-Si (dashed lines).

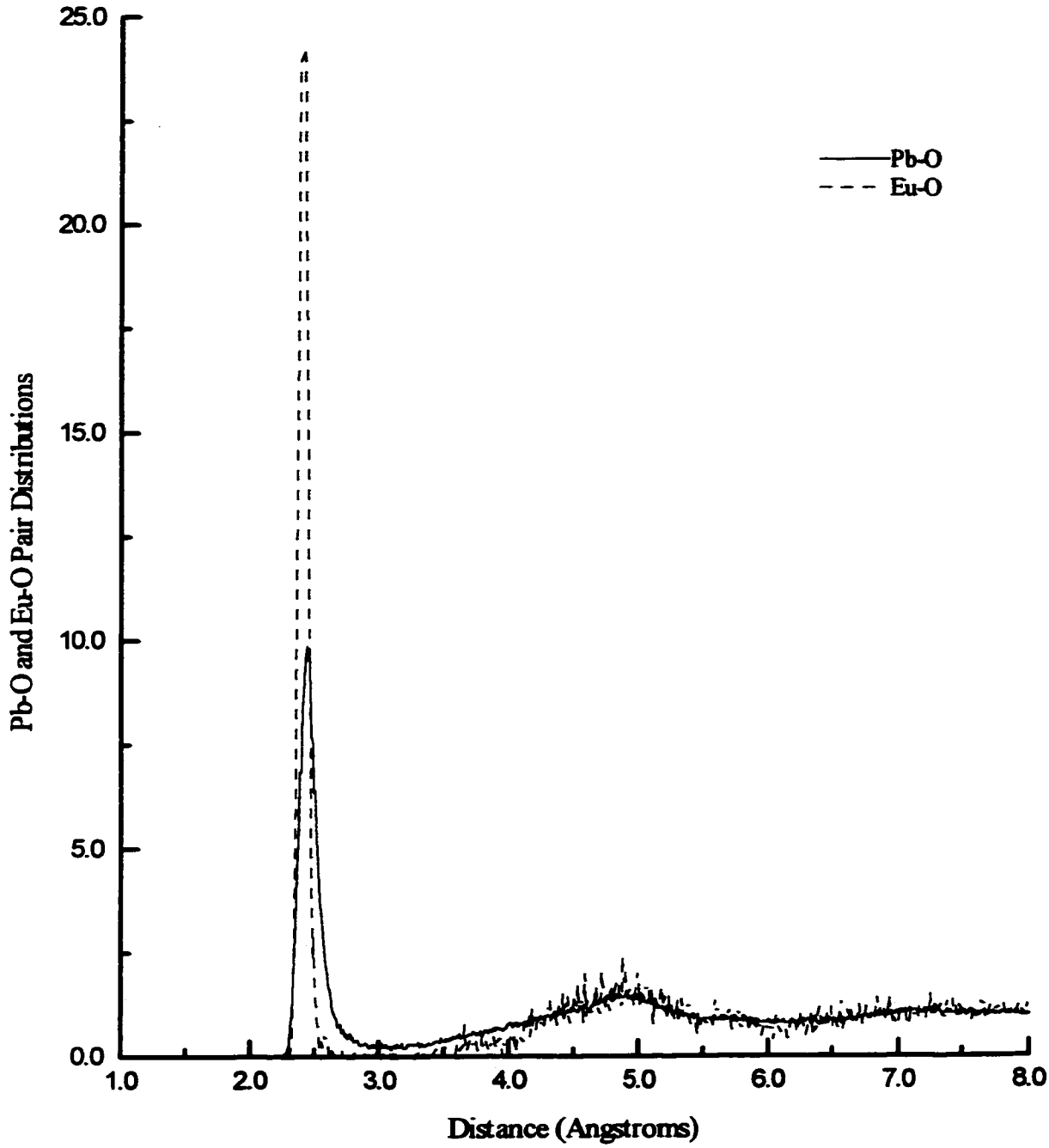

Figure 5.1.3.2a. Pair distribution functions of the Pb-O (solid) and Eu-O (dashed) interionic pairs for the 2.0% Eu^{3+}:$PbO{\cdot}SiO_2$ simulated glass.

The PDFs were the first indication that the europium ions are found in a similar environment to the lead ions and therefore the local environment of the two cations will be discussed concurrently. As reported in Table 5.1.3.1., the average Pb-O interionic distance was found to be 2.43 Å for the first coordination shell with a peak width (FWHM) of 0.14 Å. This result is in good agreement with experimental results obtained by pulsed neutron scattering [23] and X-ray diffraction data [30,35] for lead metasilicate glass. The PDF (Figure 5.1.3.2a.) does not return to a null value after the first maximum indicating that there is no clear distinction between the first and second coordination shell. The curve, however, is relatively sharp and this can be attributed to the strong polarizability of both the Pb^{2+} and the O^{2-} ions. Recall, that at high lead-oxide concentrations, the Pb^{2+} ions partake in the glass forming network [25]. The average coordination of lead, obtained by extrapolation of the CDF at a cutoff radius of 3.2 Å, is 5.63. In comparison, the simulated lead silicate glass parameters agree well with the average structural values calculated for the alamosite crystal [135].

The Eu-O interionic distance was found to be 2.40 Å with a peak width (FWHM) of 0.07 Å (Table 5.1.3.1.). The PDF shows a sharp first peak and returns to a null value indicating there is good separation between the first and second coordination shell. The sharp and narrow first peak indicates that the europium-oxygen local environment is quite ordered. This is further illustrated in the CDF (Figure 5.1.3.2b. - dashed line) where at a cutoff radius of 3.2 Å, a flat distribution is obtained and each europium ion is surrounded by an average of 6.5 oxygen neighbours. No experimental data on europium-doped lead silicate glass was found, however, six coordinated lanthanides in amorphous oxides have been previously reported [66,72,73].

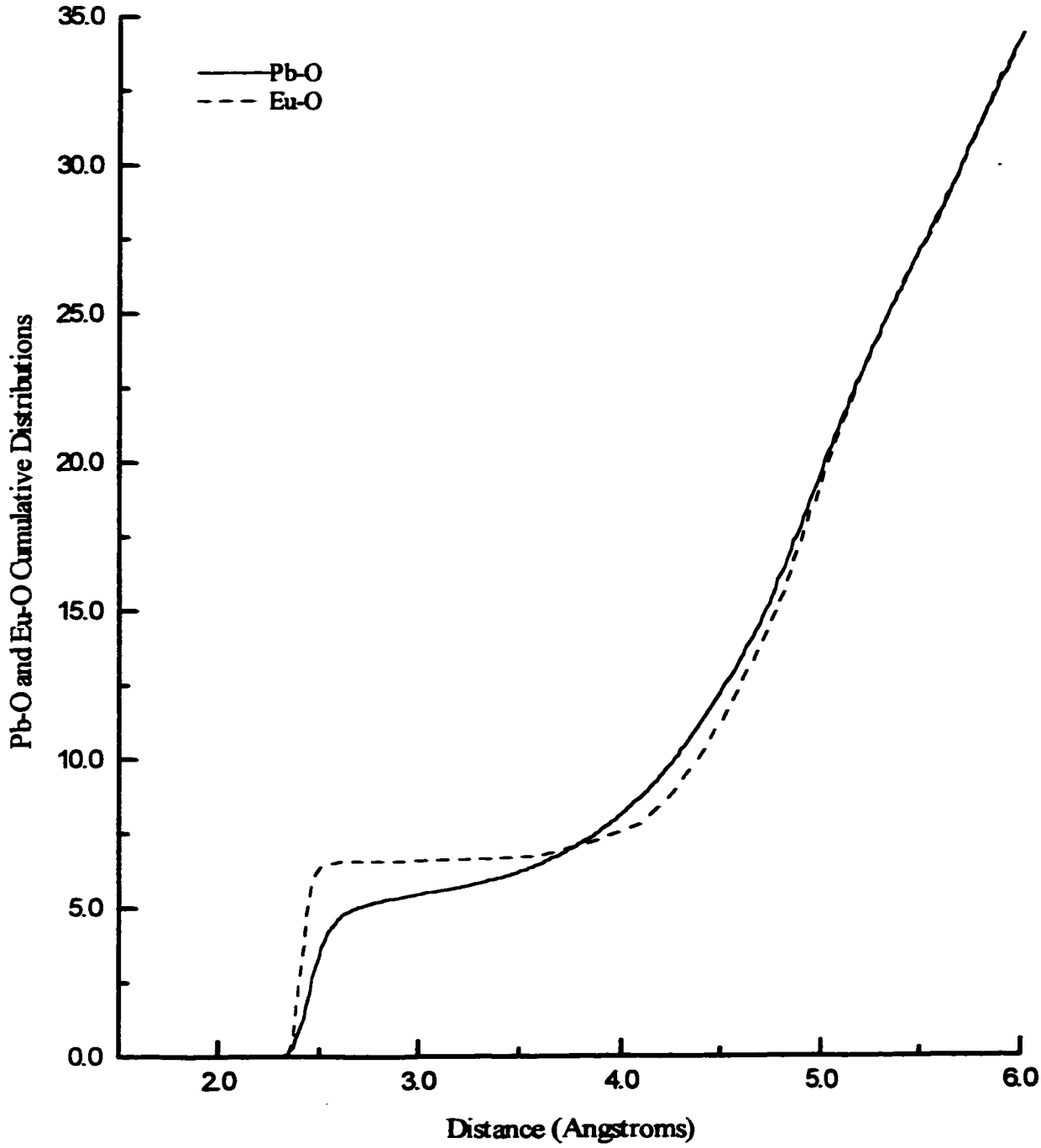

Figure 5.1.3.2b. Cumulative distribution functions of the Pb-O (solid) and Eu-O (dashed) interionic pairs for the 2.0% Eu^{3+}:$PbO{\cdot}SiO_2$ simulated glass.

Robinson, Fournier and Bartram wrote a series of articles [66,72,73] studying Yb^{3+}-doped phosphate, silicate and germanate glasses, Er^{3+} in alkali silicate glasses [67,68] and Nd^{3+}-doped in barium rubidium silicate glass [151]. They postulated from low-temperature absorption and emission spectra of the lanthanide ions that the principal rare-earth environment in these glasses is a distorted six-fold polyhedron. An EXAFS and photoluminescence study of Er^{3+}-doped silica and sodium silicate glass by Marcus and Polman [70] showed that in the case of the sodium silicate sample, the Er^{3+} ions were surrounded by an average of 6.3 oxygens in the first coordination shell. Furthermore, in two previous molecular dynamics simulations studies of Eu^{3+}-doped sodium silicate [45,57] and Eu^{3+}-doped lead metaphosphate [105] glasses, Cormier et al. [57] postulated that the Eu^{3+} ions were coordinated by 6 and 7 oxygens at a cutoff radius of 3.2 Å.

The Pb-Pb and Eu-Pb pair distribution functions are broad and asymmetric (Figure 5.1.3.3a). The Pb-Pb interionic distance was found to be 3.6 Å with a peak width (FWHM) of 1.2 Å with an average coordination number of 8.0 evaluated at a cutoff distance of 4.6 Å. The values reported here for the Pb-Pb pairs are in good agreement with the results obtained by Mydlar et al. [30] from an X-ray study of $PbSiO_3$ glass. The Eu-Pb interionic distance was found to be 3.5 Å with a peak width (FWHM) of 0.8 Å and an average coordination number of 8.3 (cutoff radius of 4.6 Å).

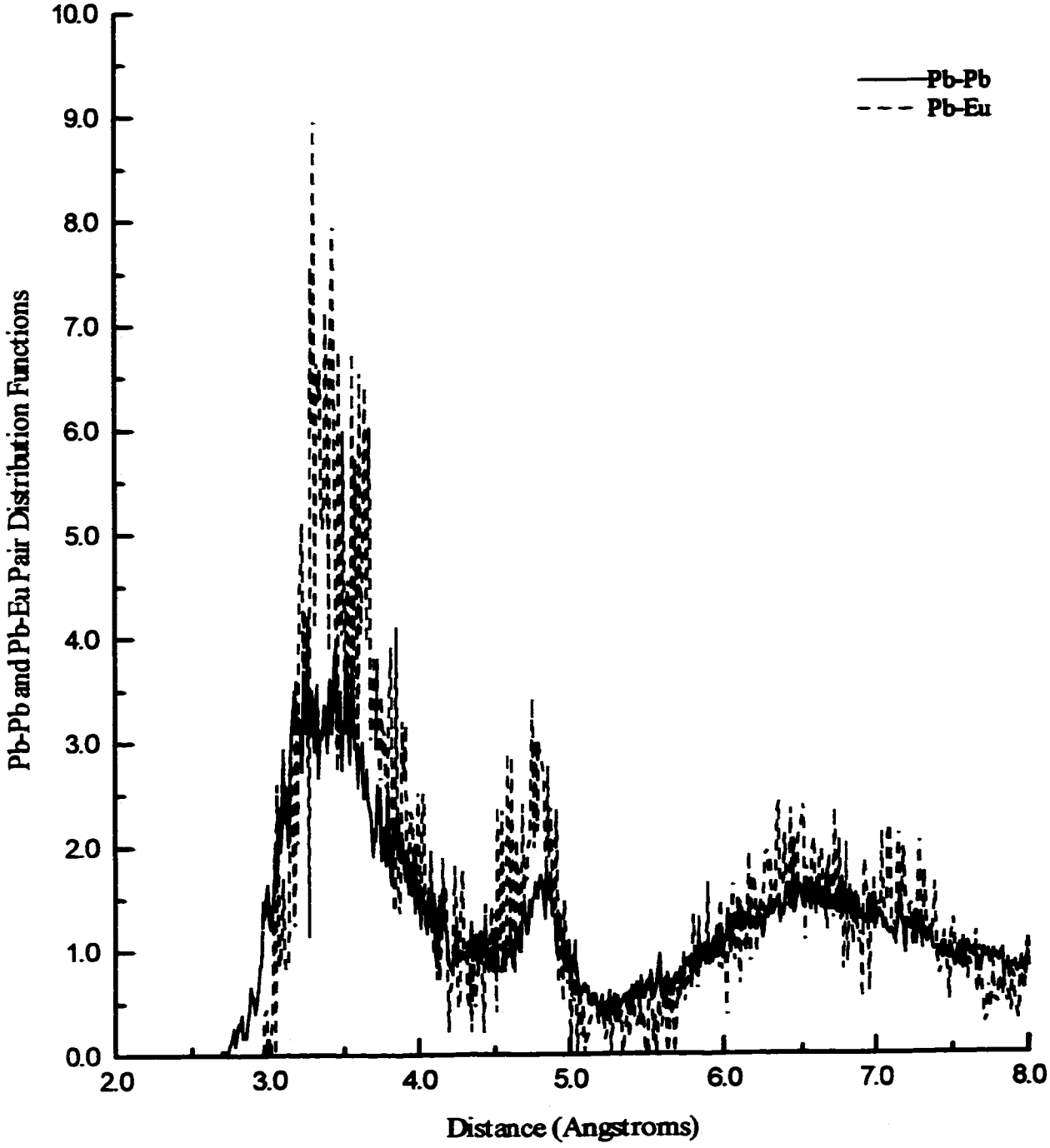

Figure 5.1.3.3a. Pair distribution functions of the Pb-Pb (solid) and Pb-Eu (dashed) interionic pairs for the 2.0% Eu^{3+}:$PbO{\cdot}SiO_2$ simulated glass.

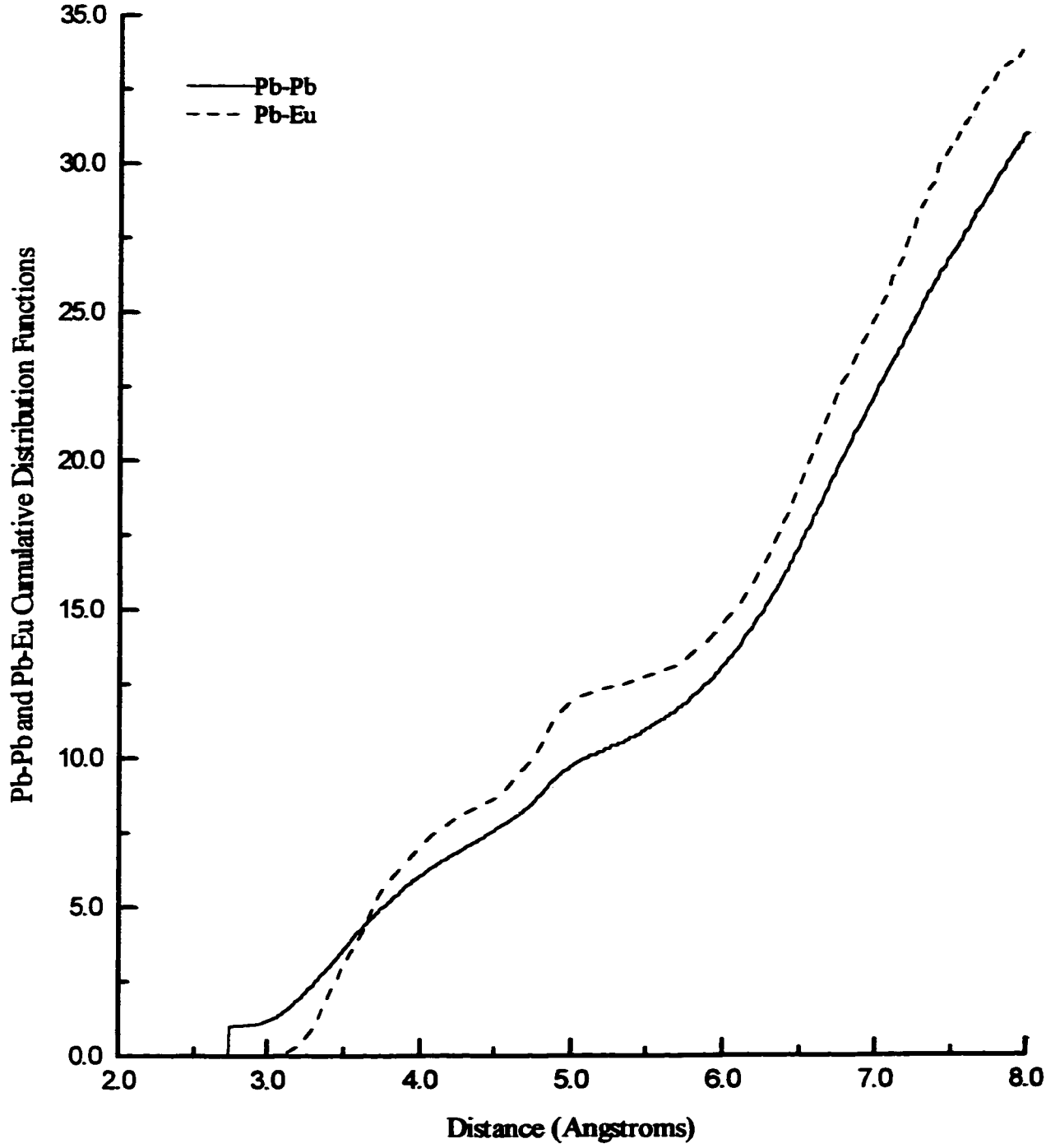

Figure 5.1.3.3b. Cumulative distribution functions of the Pb-Pb (solid) and Pb-Eu (dashed) interionic pairs for the 2.0% Eu^{3+}:$PbO{\cdot}SiO_2$ simulated glass.

The Pb-Si and Eu-Si PDFs and CDFs are shown in Figure's 5.1.3.4a. and 5.1.3.4b., respectively.

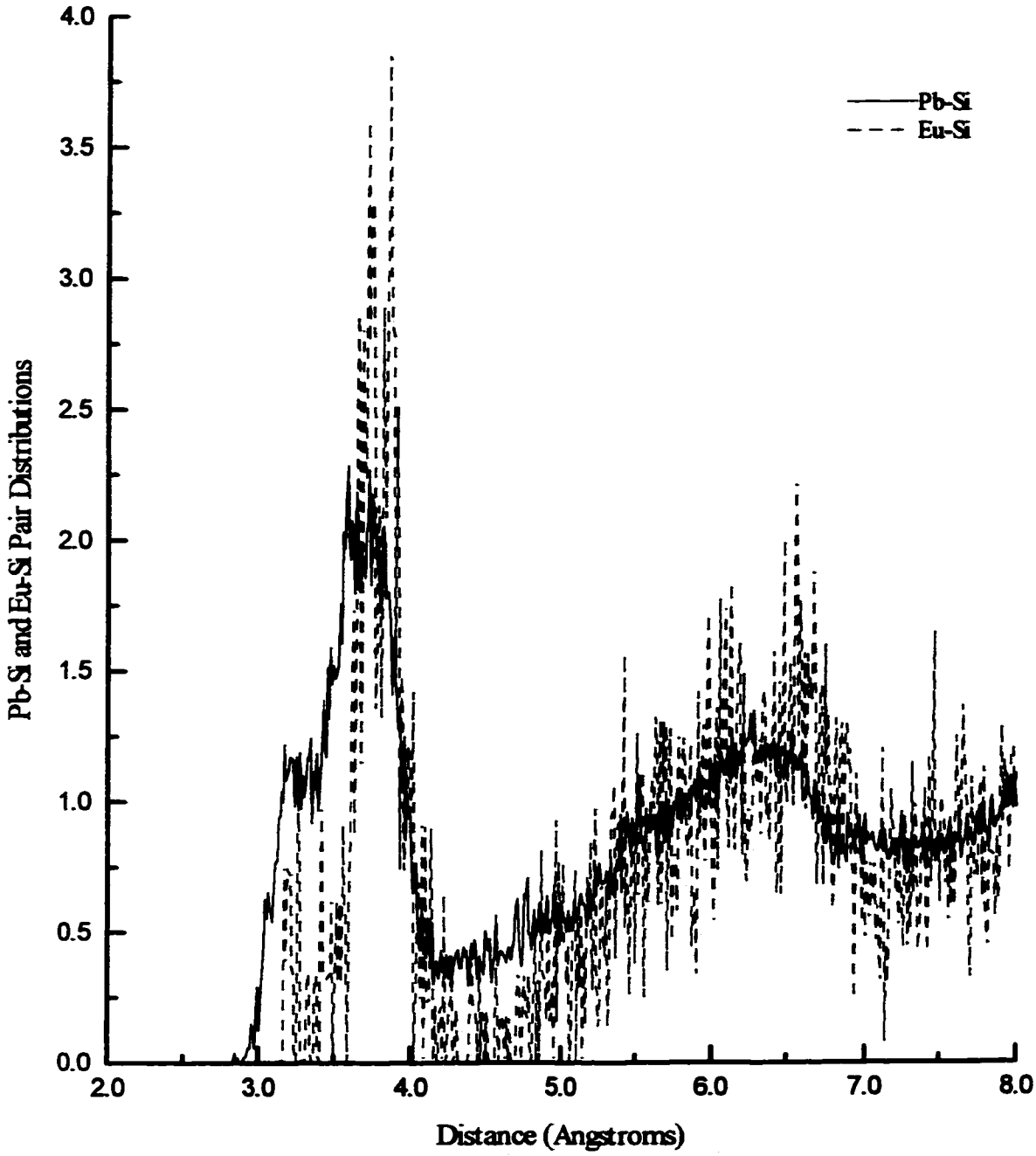

Figure 5.1.3.4a. Pair distribution functions of the Pb-Si (solid) and Eu-Si (dashed) interionic pairs for the 2.0% Eu^{3+}:PbO·SiO_2 simulated glass.

The Pb-Si first coordination peak shows a maximum at 3.81Å with a shoulder at 3.4 Å with an overall FWHM of 1.59 Å and an average coordination number of 3.25 at a cutoff radius of 4.2 Å. The results for the lead-silicon atomic pair differ slightly from those found in alamosite [135]. At a cutoff distance of 4.2 Å, the average coordination number for the three lead sites in the crystal is equal to 5.0. The difference between the coordination values for the crystal and the simulated glass may be attributed to the lead rich and silicon rich regions in the glass. These distinct regions would reduce the number of silicons surrounding the lead ion in the Pb-Si first coordination shell. Similarly, the PDF of the Eu-Si pair (Figure 5.1.3.4a.) shows a peak having a maximum at 3.90 Å with a FWHM of 0.75 Å and a shoulder present at 3.2 Å. The average number of silicons surrounding the europium ion at a cutoff distance of 4.2 Å was determined to be 1.80. The low Eu-Si coordination is not unexpected since the europium ions are located in the lead rich regions of the glass thus a lower number of silicons would be present in the first europium-silicon coordination shell.

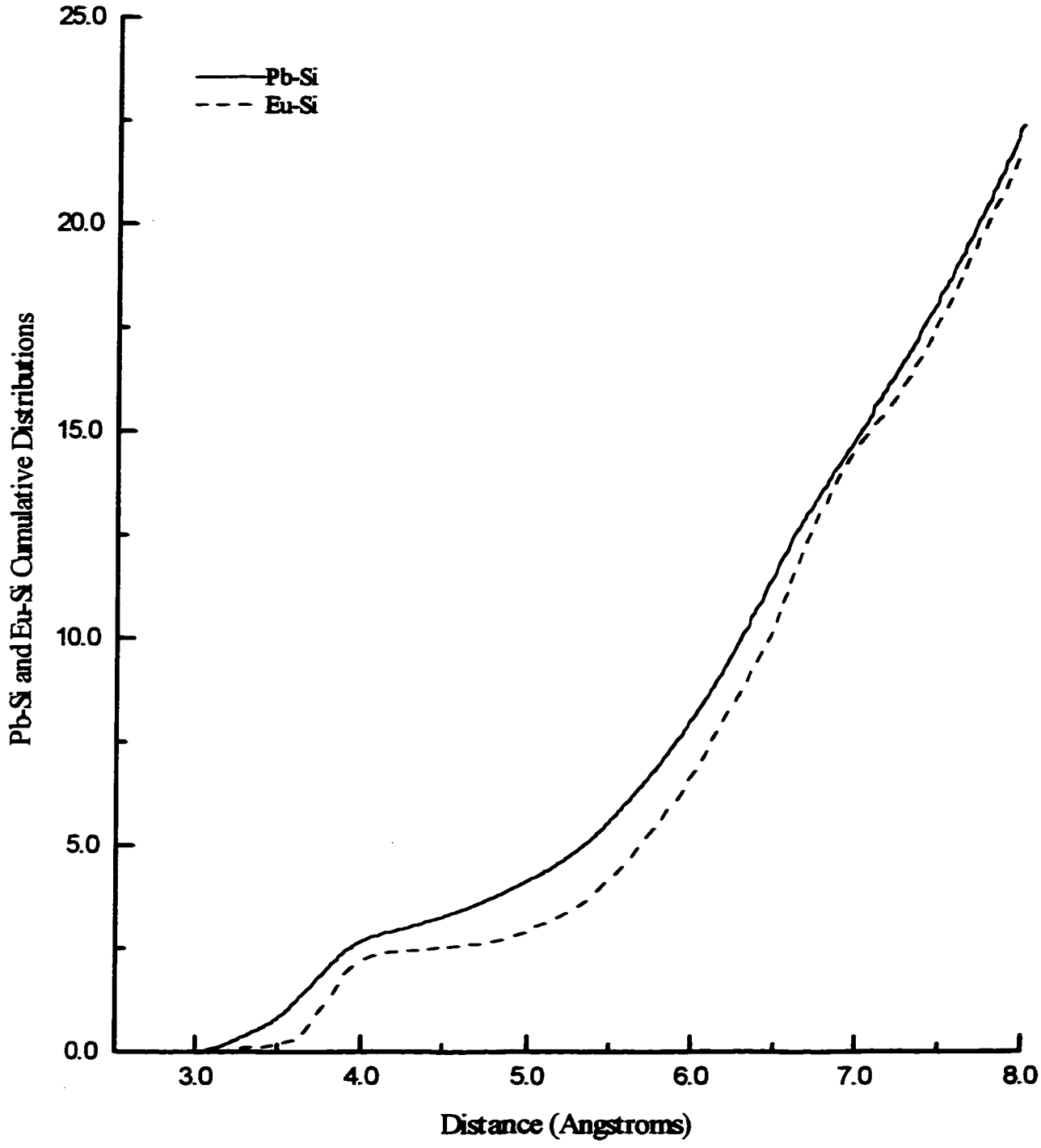

Figure 5.1.3.4b. Cumulative distribution functions of the Pb-Si (solid) and Eu-Si (dashed) interionic pairs for the 2.0% Eu^{3+}:$PbO{\cdot}SiO_2$ simulated glass.

Further quantification that the europium ions are located in the lead rich region of the glass can be obtained by examining the Pb-Eu and Si-Eu pair distribution functions. As expected, the Pb-Eu PDF shows a much more pronounced first peak than the Si-Eu PDF indicating that the europium ions are present in the same environment as the lead ions, that is, in the lead rich regions of the glass.

In order to examine further the environment of the europium ions, a speciation of the oxygen types surrounding individual europium ions was calculated with respect to the silicate network (Table 5.1.3.2a.) and the lead network (Table 5.1.3.2b.). The results presented in Table 5.1.3.2a. and 5.1.3.2b. confirm that the europium ions are distributed within the lead network. We observe from Table 5.1.3.2a. that 72.0% of the oxygens in the first Eu^{3+} coordination shell are not connected to silicon ions and do not partake in the silicon backbone and are associated with the secondary lead network. Furthermore, it can be seen from Table 5.1.3.2b. that approximately 97% (sum of values for $n_{Pb} = 1$ to $n_{Pb} = 5$) of the europium ions have at least one lead neighbour within a distance of 2.8 Å.

Table 5.1.3.2a.

Percent speciation of oxygen in the first Eu^{3+} coordination shell with respect to the silicate network

$n_{Si} = 0$ (free)	$n_{Si} = 1$ (NBO)	$n_{Si} = 2$ (BO)	$n_{Si} > 2$ (anomalies)
72.0	28.0	0.0	0.0

Table 5.1.3.2b.

Percent speciation of oxygen in the first Eu^{3+} coordination shell with respect to the lead network

$n_{Pb} = 0$	$n_{Pb} = 1$	$n_{Pb} = 2$	$n_{Pb} = 3$	$n_{Pb} = 4$	$n_{Pb} = 5$
2.3	16.7	16.7	16.2	31.8	15.9

Figure 5.1.3.6. shows the distribution (in percent) of coordination for the Pb^{2+} and Eu^{3+} ions in the respective first coordination shells. From Figure 5.1.3.6., it can be seen that the Pb^{2+} ions have principally 5 and 6 nearest neighbour oxygens with a smaller number of 4 and 7 coordinated oxygens, whereas the Eu^{3+} ions are coordinated mainly by 6 and 7 nearest neighbour oxygens.

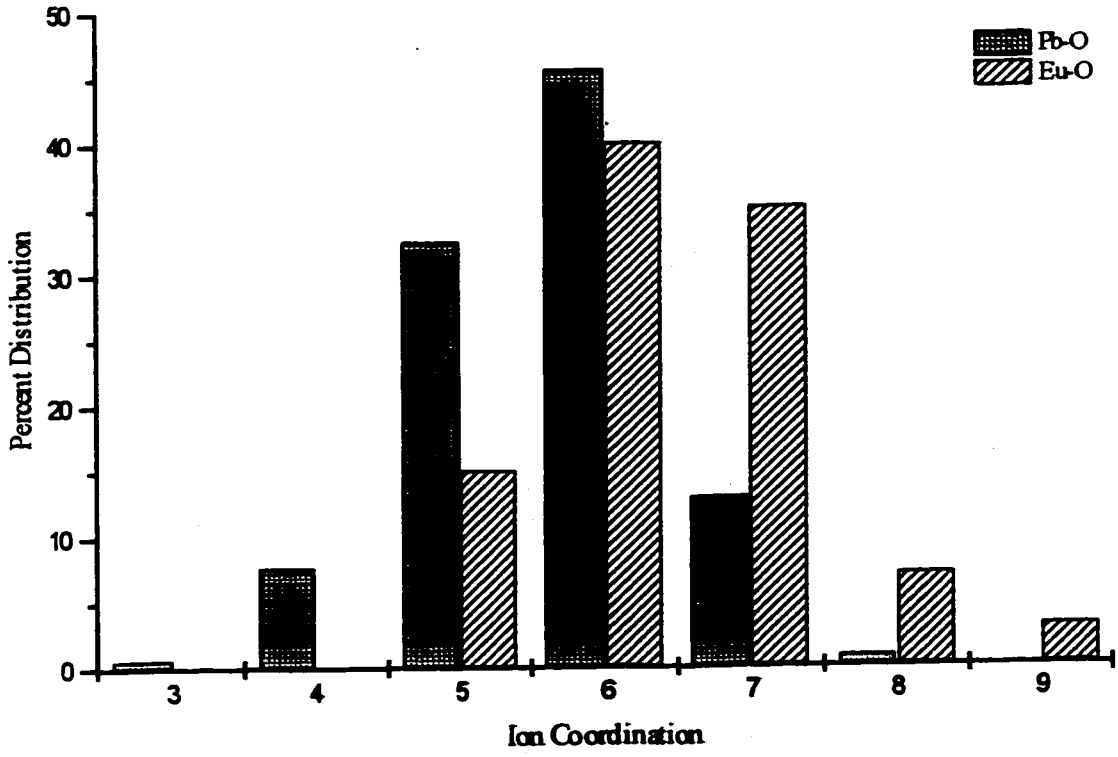

Figure 5.1.3.6. Histogram of the percent coordination distribution for the Pb-O (gray) and Eu-O (dashed) ionic pairs in the first coordination shell (cutoff radius = 3.2Å)

To further investigate the secondary lead network, a bond angle distribution analysis was performed to determine the connectivity of the lead units. The O-Pb-O bond angle distribution has three distinct peaks at 57°, 90° and a broader less intense distribution at 135°. The major distribution occurs at approximately 90° and can be explained by a sixfold coordinated octahedral type structure and the four coordinated species, which are most probably PbO_3 pyramidal structures. Imaoka et al. [35] have postulated, using X-ray diffraction, that at PbO concentrations between 50-66.6 mol%, only PbO_3 pyramidal units are present in $PbO{\cdot}SiO_2$ glass. The bond angle distribution found at 135° may be related to the five coordinated lead species (Figure 5.1.3.6.). The seven coordinated structure could be either a pentagonal bipyramid, a capped octahedron or a capped trigonal prism. All three of the above mentioned geometries would have bond angles in the range of the O-Pb-O and Pb-O-Pb distributions and it is therefore difficult to ascertain exactly which geometry is present. The Pb-O-Pb bond angle distribution has two peaks, one at 92° and another at 160°. This distribution is typical of edge-sharing in glasses. In order to examine if edge sharing is present in the simulated glass, the Pb-O-Pb-O and Si-O-Pb-O linkages were calculated. As previously stated in the discussion of the oxygen-oxygen atomic pair, the shortened O-O bond at 2.40 Å is an indication of edge-sharing in the glass. The first peak maxima in the Pb-Si (Figure 5.1.3.4a.) and Pb-Pb (Figure 5.1.3.3a.) pair distribution functions are comprised of several local maxima and thus the lead ion can occupy a variety of sites in the glass. Figure 5.1.3.7. shows the types of edge-sharing which may be found in the simulated glass. Similar results were observed in a molecular dynamics study of amorphous zinc silicate [141].

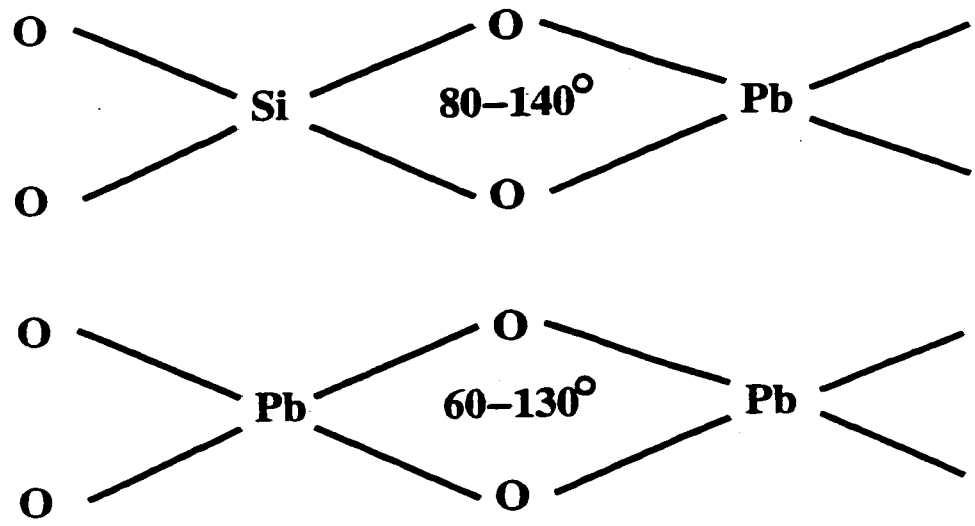

Figure 5.1.3.7. Two types of edge sharing observed in the 2.0% Eu^{3+}-doped lead silicate glass. Si-O-Pb-O (above) and Pb-O-Pb-O (below).

The Eu-O CDF (Figure 5.1.3.2b.), is in good agreement with experimental data [66,70], and shows a very well defined first coordination shell composed of six or seven oxygen ions with the six coordinated environments being slightly predominant. X-ray and neutron diffraction data are the most direct experimental techniques to identify coordination numbers as well as the radial structure around a RE^{3+} (rare-earth) ion. These techniques, however, do not reveal any information on the structure of the first coordination shell or the symmetry of the coordination polyhedra.

In order to visualize directly the structure of the first hydration shell of several rare-earth ions (Nd^{3+}, Sm^{3-}, and Yb^{3+}), Kowall et al. [152,153] generated plots based on the configurations obtained from the MD simulations. The first hydration shells of all the

configurations were accumulated in such a way that the oxygens are superposed to a maximum degree. The authors used a general-purpose program called LSQS from the GROMOS package [152], which provides the rotation matrix to superimpose two identical molecules of different configurations. This method was also employed by Chaussedent et al. [60] to describe the environment of the first hydration shell for a dilute $EuCl_3$ aqueous solution. Calculations of the O-Eu-O and Eu-O-Eu angular distribution functions suggest that there are two different geometric arrangements. In order to isolate the different geometries, a method similar to that used by Chaussedent et al. [60] was employed. After the identification and superposition of the ions, obtained from the ten different configurations, it was found that the geometrical arrangements for the six coordinated species is a distorted octahedron whereas the seven coordinated species show a distorted pentagonal bipyramid geometry. This is shown in Figure 5.1.3.8a and 5.1.3.8b., respectively. For both geometries, large distributions around the mean positions were observed, in contrast to what has been observed for Eu^{3+} in aqueous solutions, whereby the water molecules are arranged around the Eu^{3+} ion according to the vertices of a square antiprism with only small variations [60]. Despite the larger fluctuations observed in the glass structure, only two geometrical arrangements are observed

The simulation of 2% Eu^{3+}-doped lead silicate glass reproduced well bulk structural features such as interionic distances and average coordination numbers observed in X-ray, neutron and EXAFS studies. The simulation showed the presence of two networks, a silicate and lead network. The Eu^{3+} ions were found primarily in the lead network, with only a modest presence in the silicate network, showing that the two cations (Pb^{2+}, Eu^{3+}) share similar environments.

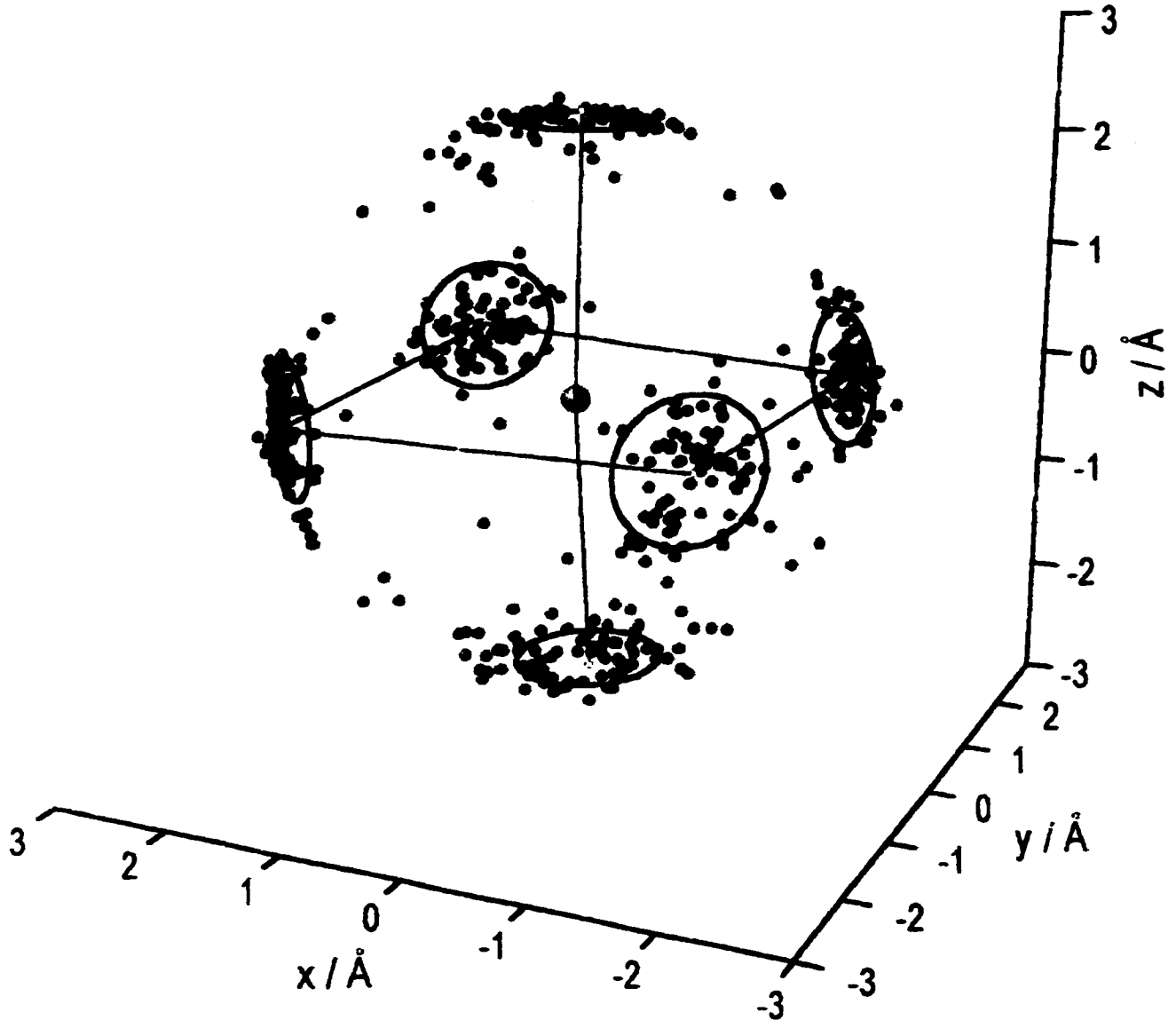

Figure 5.1.3.8a. Geometrical arrangement of a distorted octahedron for the Eu^{3+} ion in 2.0% Eu^{3+}:$PbO{\cdot}SiO_2$ simulated glass.

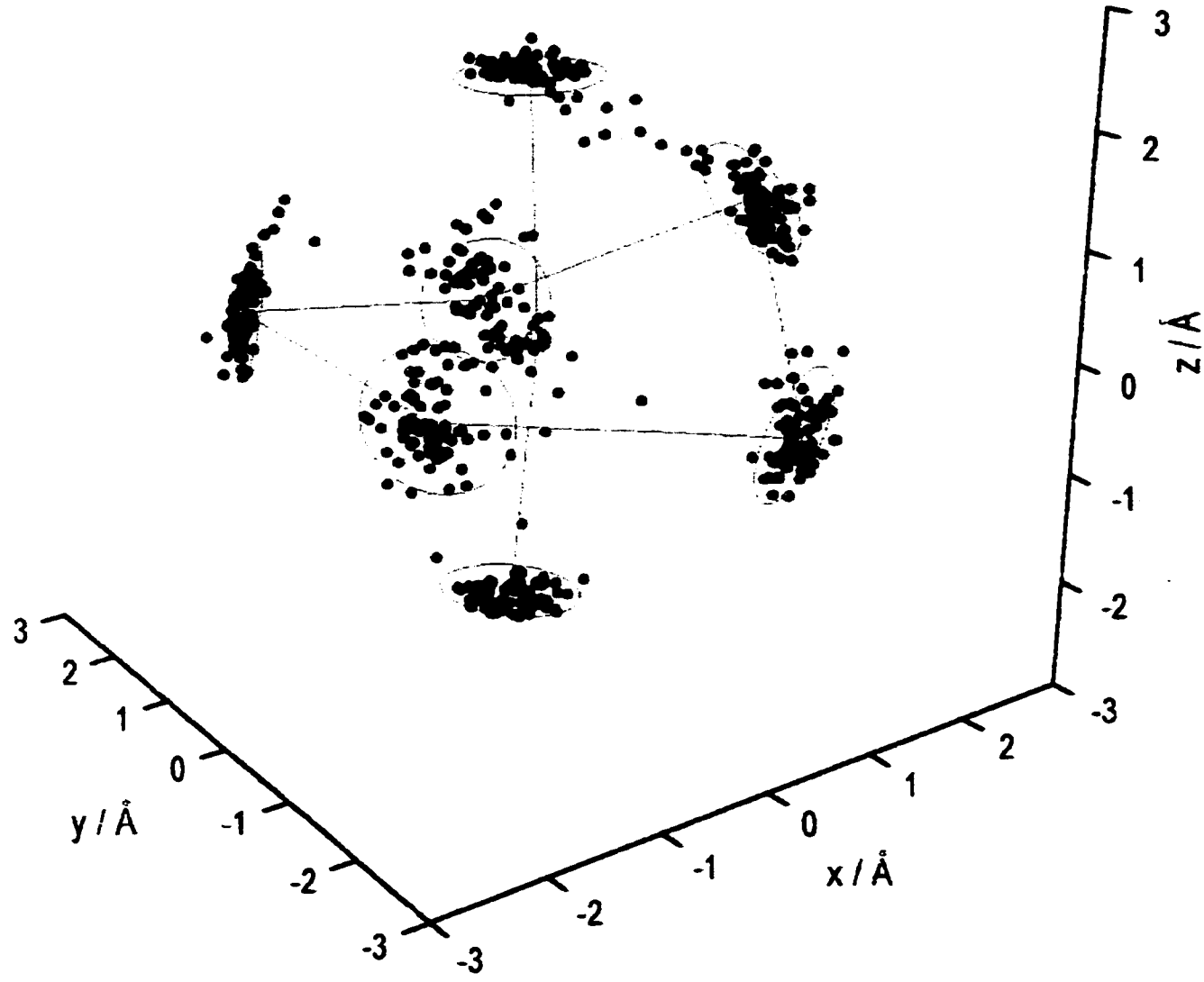

Figure 5.1.3.8b. Geometrical arrangement of a pentagonal bipyramid for the Eu^{3+} ion in 2.0% Eu^{3+}:PbO-SiO_2 simulated glass.

The average coordination number of Eu^{3+} was found to be 6.5 with two major geometrical arrangements contributing to a distorted octahedron and a distorted pentagonal bipyramid.

5.1.4. A comparison of several rare-earth dopants

The change in coordination number from 9 to 6 across the lanthanide series has been reported using both experimental [154,155] and simulation techniques [152,153]. Since the spectroscopic properties of the dopant ions are dependent on the local environment, a study on first coordination sphere of three different rare-earths was performed. Using the three-body potential model described in Section 2.2.2 of this thesis, Eu^{3+}-, Er^{3+}- and Yb^{3+}-doped lead silicate glasses were simulated for a glass composition of $0.48PbO{\cdot}0.51SiO_2{\cdot}0.01RE_2O_3$ for each of the dopant ions. In order to ensure statistical reproducibility, 200 different Eu^{3+} configurations were generated at 300K. The general structure of the doped glasses was determined by calculating the pair (PDF) and cumulative (CDF) distribution functions and no significant differences were found to exist between the glasses.

Figure 5.1.4.1. shows the PDFs for the Eu-O (solid), Er-O (dotted) and Yb-O (dashed) interionic pairs. The Eu-O interionic distance was found to be 2.41Å, the Er-O and Yb-O were found to be 2.26 Å and 2.25Å, respectively. The interionic distances are in good agreement with EXAFS [70] data as well as with the corresponding crystalline counterparts, Eu_2O_3 [156], Er_2O_3 [156] and Yb_2O_3 [156]. The PDFs have a sharp first peak and return to a null value indicating that the RE-O local environment is quite ordered. The differences in the interionic distances can be attributed to the differences in the ionic radii of the rare-earths. Europium has an ionic radius of 109 pm, erbium has a radius of 103 pm and ytterbium a radius of 100 pm.

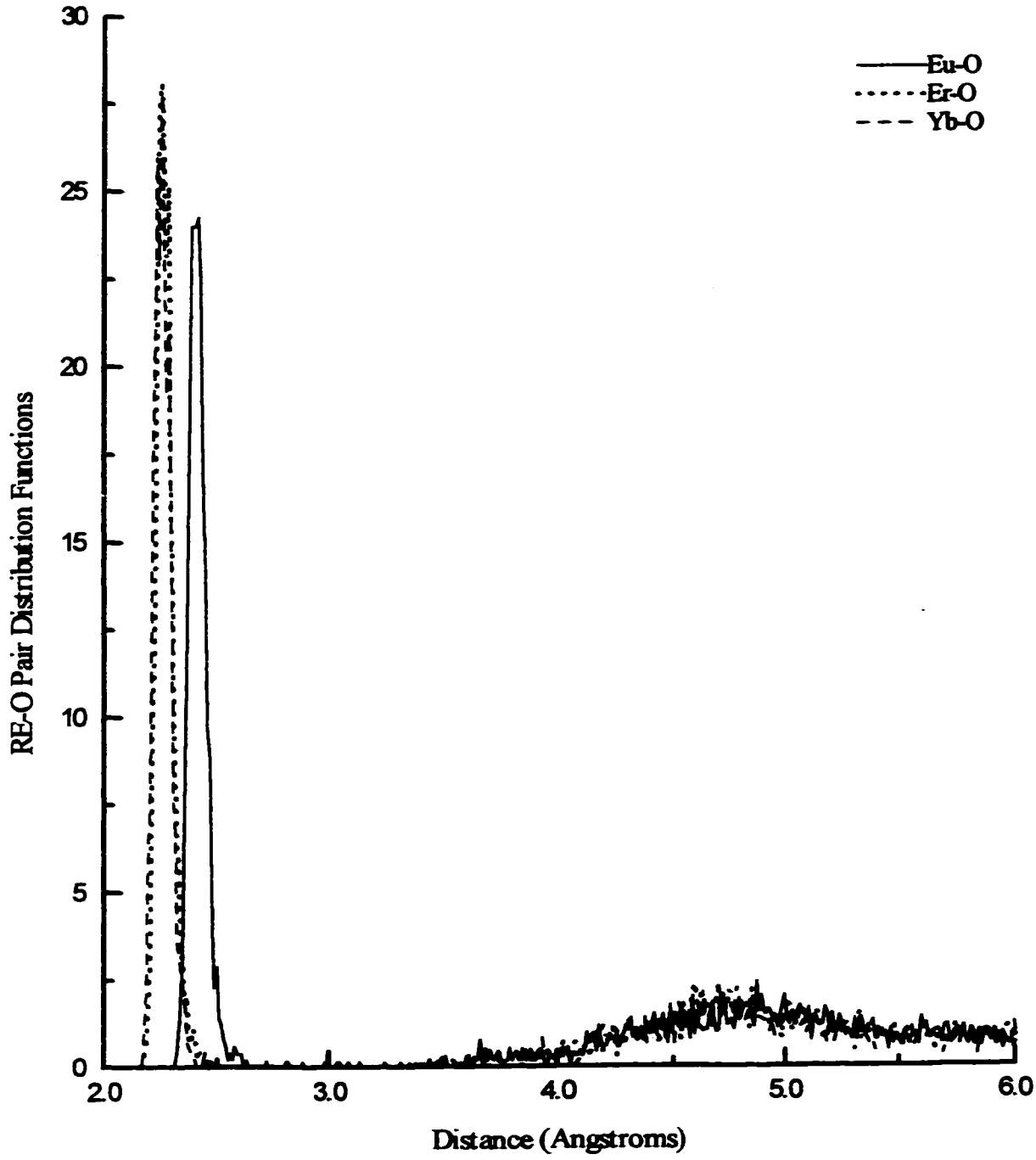

Figure 5.1.4.1. Pair distribution functions of the Eu-O (solid), Er-O (dotted) and Yb-O (dashed) interionic pairs for the 2.0% RE^{3+}-$PbO{\cdot}SiO_2$ simulated glasses.

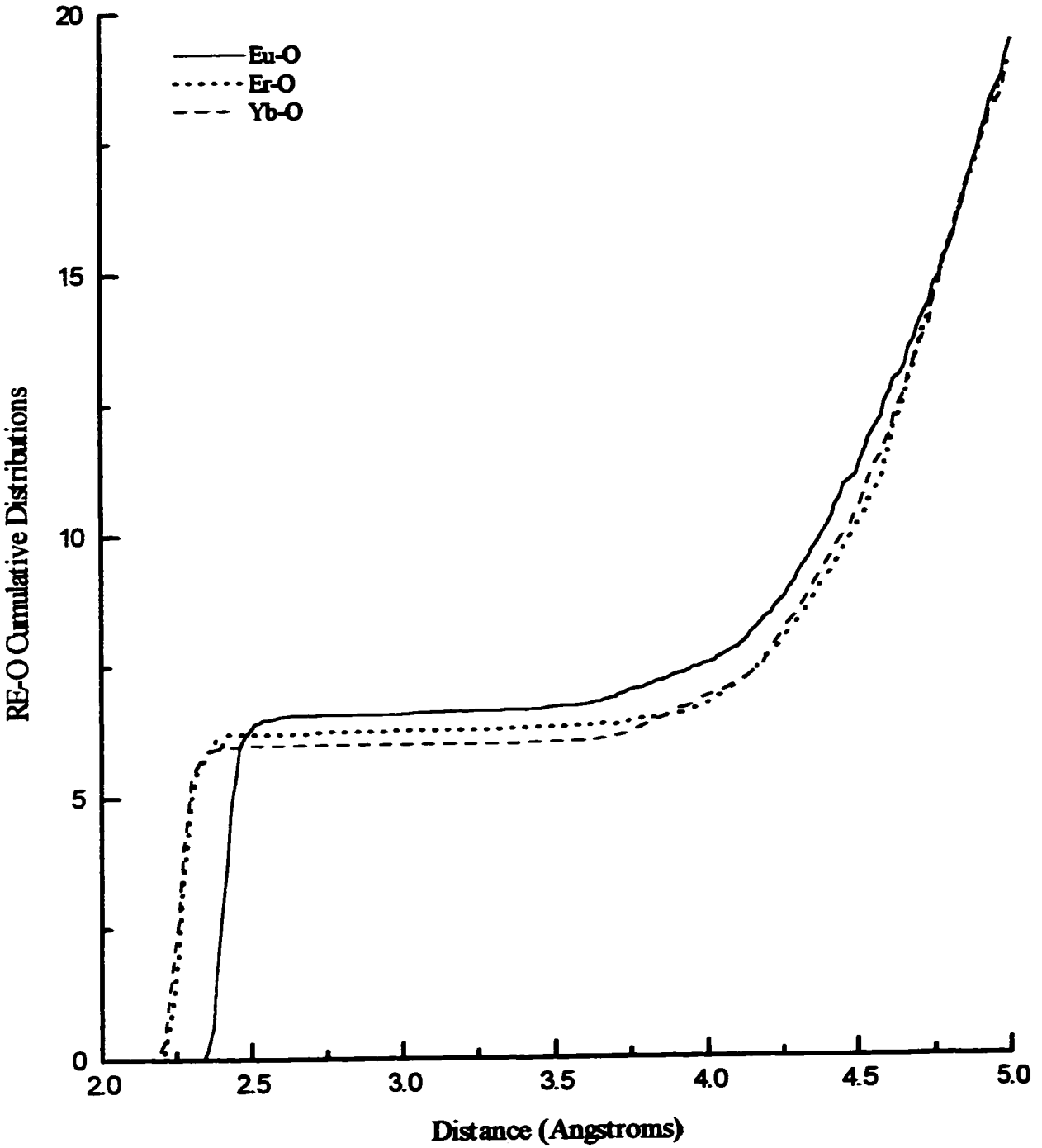

Figure 5.1.4.2. Cumulative distribution functions of the Eu-O (solid), Er-O (dotted) and Yb-O (dashed) interionic pairs for the 2.0% RE^{3+}-$PbO{\cdot}SiO_2$ simulated glasses.

This slight decrease in ionic radii is due to the fact that across the series of rare-earths, the increasing nuclear charge causes a contraction in the radius of the RE^{3+} ion, this is the well known Lanthanide Contraction. Although the difference in the radii is very small, it is sufficiently significant that a change in the interionic distance was observed.

The CDFs for the Eu-O (solid), Er-O (dotted) and Yb-O (dashed) interionic pairs are shown in Figure 5.1.4.2. The Eu^{3+} ion was found to have an average of 6.5 nearest oxygen neighbours at a cutoff radius of 3.2 Å. At the same cutoff radius, Er^{3+} was found to have an average of 6.2 oxygens while Yb^{3+} shows an average of 5.93 nearest oxygen neighbours. As expected, the difference in the average coordination number is not significant and they are in good agreement with those observed experimentally [66,72,73]. However, it is the individual coordination numbers that contribute to the average coordination, which becomes important in defining the local environments for each of the rare-earth ions. Figure 5.1.4.3. shows a histogram of the coordination number distributions for Eu^{3+}, Er^{3+} and Yb^{3+}. As discussed previously in Section 5.1.3. of this thesis, the principal coordination numbers for the europium ions are six and seven. In the case of erbium, 35% of the Er^{3+} ions are six coordinated, 25% are seven coordinated structures and 20% are five coordinated. The ytterbium ions are predominately six coordinated (Figure 5.1.4.3.). However, there is a higher percentage of five coordinated Yb^{3+} ions, which explains the decrease in average coordination number.

From the simulations of the different rare-earth ions it was possible to isolate the different local environments specific to each of the dopants. This becomes important since it is the local environments that influence the spectroscopic properties of the dopant ion. Another substantial result of this study was the verification of the sensitivity of the three-body potential model. Although the differences in ionic radii, interionic distance and

average coordination number between the three rare-earths was quite small, the three-body potential model successfully reproduced these differences in the bulk structural features, and the results were found to be in excellent agreement with experimental data [66,70,72,73].

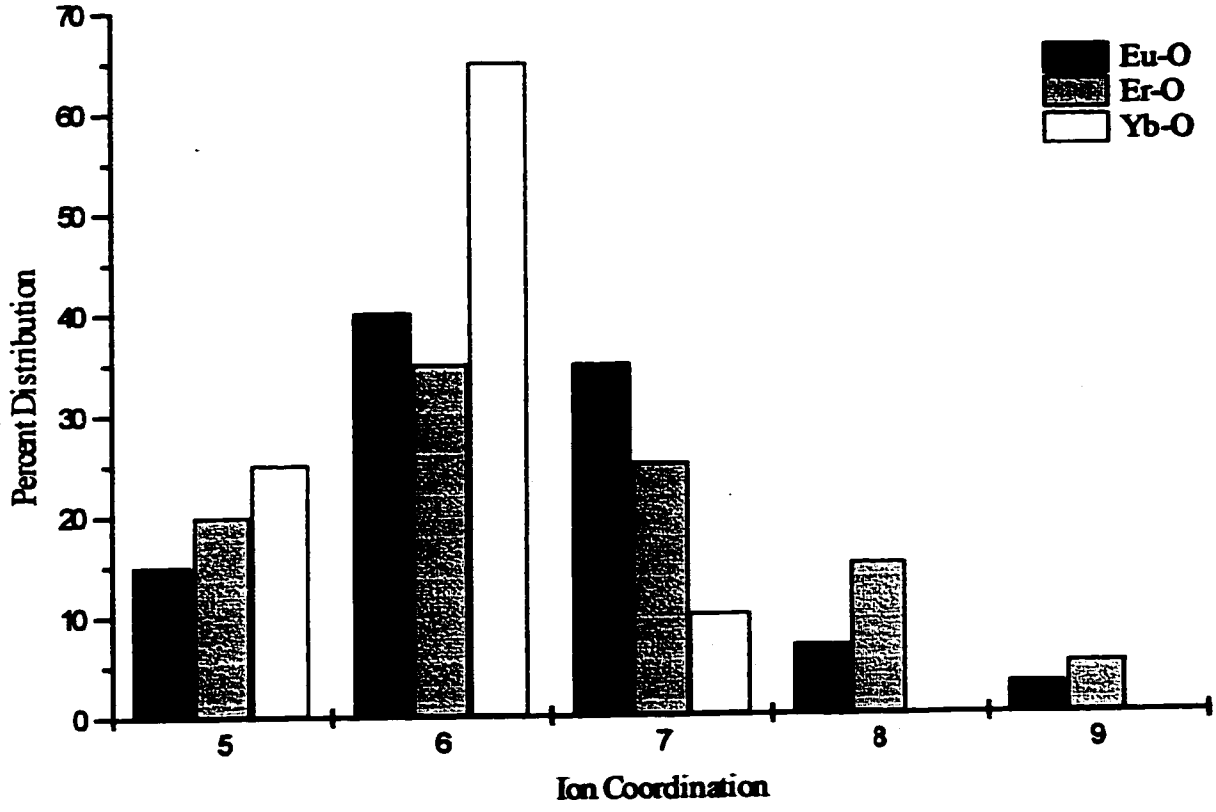

Figure 5.1.4.3. Histogram of the percent coordination distribution for the Eu-O (black) and Er-O (light gray) and Yb-O (white) ionic pairs in the first coordination shell (cutoff radius = 3.2Å)

5.1.5. A study of erbium-erbium clustering in Er^{3+}-doped lead silicate glass

The main reason for studying the clustering of erbium ions is to examine the possibility of intercluster and cluster-to-cluster energy transfer. Within a cluster it is speculated that the rate of energy transfer will be greater than that from cluster-to-cluster. It is important to note, however, that the rate of energy transfer is also dictated by the other ions surrounding Er^{3+}. Stauffer [157] defines a cluster as an ensemble of environments connected to one another by a chain of unbroken nearest-neighbour links from one occupied environment to a neighbouring environment. In the present study, the erbium ions would represent the environments and the oxygen ions the links between these environments. A detailed description of the rare-earth environment in lead silicate glass has been discussed in Sections 5.1.3. and 5.1.4. of this thesis.

In order to examine erbium-erbium clustering, Er^{3+}-doped lead silicate glasses of different Er^{3+} concentrations, 0.2%, 2.0%, 5.2%, 11.0% and 24.8% were simulated. The Er-O pair distribution functions for the 2.0% Er^{3+}-doped glass (solid line) and the 24.8% Er^{3+}-doped glass (dotted line) are shown in Figure 5.1.5.1a., and the respective CDFs in Figure 5.1.5.1b. The PDF of the 24.8% Er^{3+}-doped glass (Figure 5.1.5.1a.) is not as sharp as that for the 2.0% Er^{3+}-doped glass (Figure 5.1.5.1a.). The broadening at the base of the peak for the 24.8% Er^{3+} doped glass is indicative of the erbium ions sharing additional oxygens. Further evidence of this is provided by the CDFs (Figure 5.1.5.1b.). The CDF of the 2.0% Er^{3+}-doped glass is less steep than that for the 24.8% Er^{3+}-doped glass. The pair and cumulative distributions for the remaining concentrations follow the same trends as the 2.0% and 24.8% Er^{3+}-doped glasses, and the broadening of the peak increases with an increase in Er^{3+} concentration.

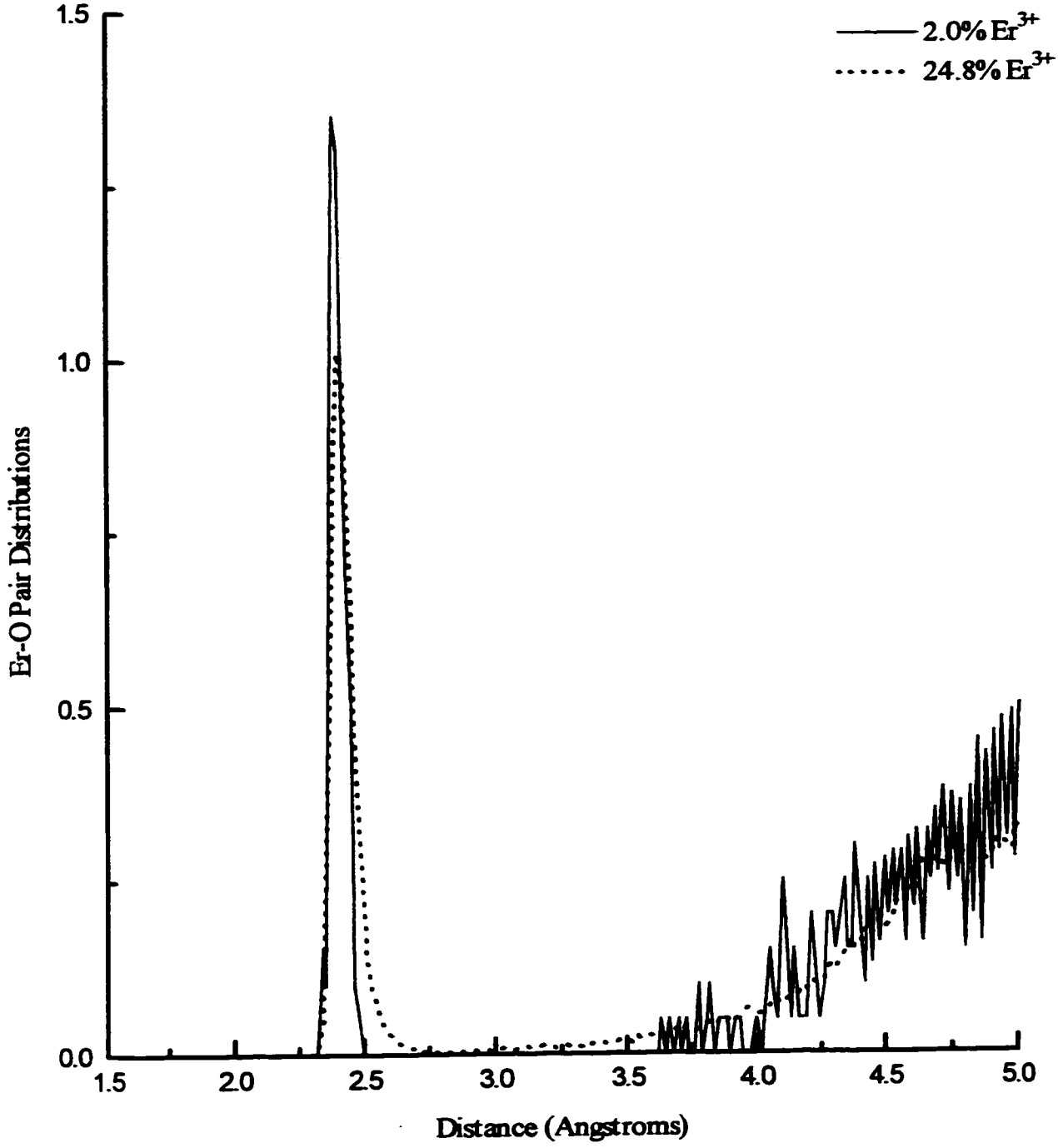

Figure 5.1.5.1a. Pair distribution functions of the Er-O ionic pair for the simulated 2.0% Er^{3+}:$PbO{\cdot}SiO_2$ glass (solid line) and the 24.8% Er^{3+}:$PbO{\cdot}SiO_2$ glass (dashed line).

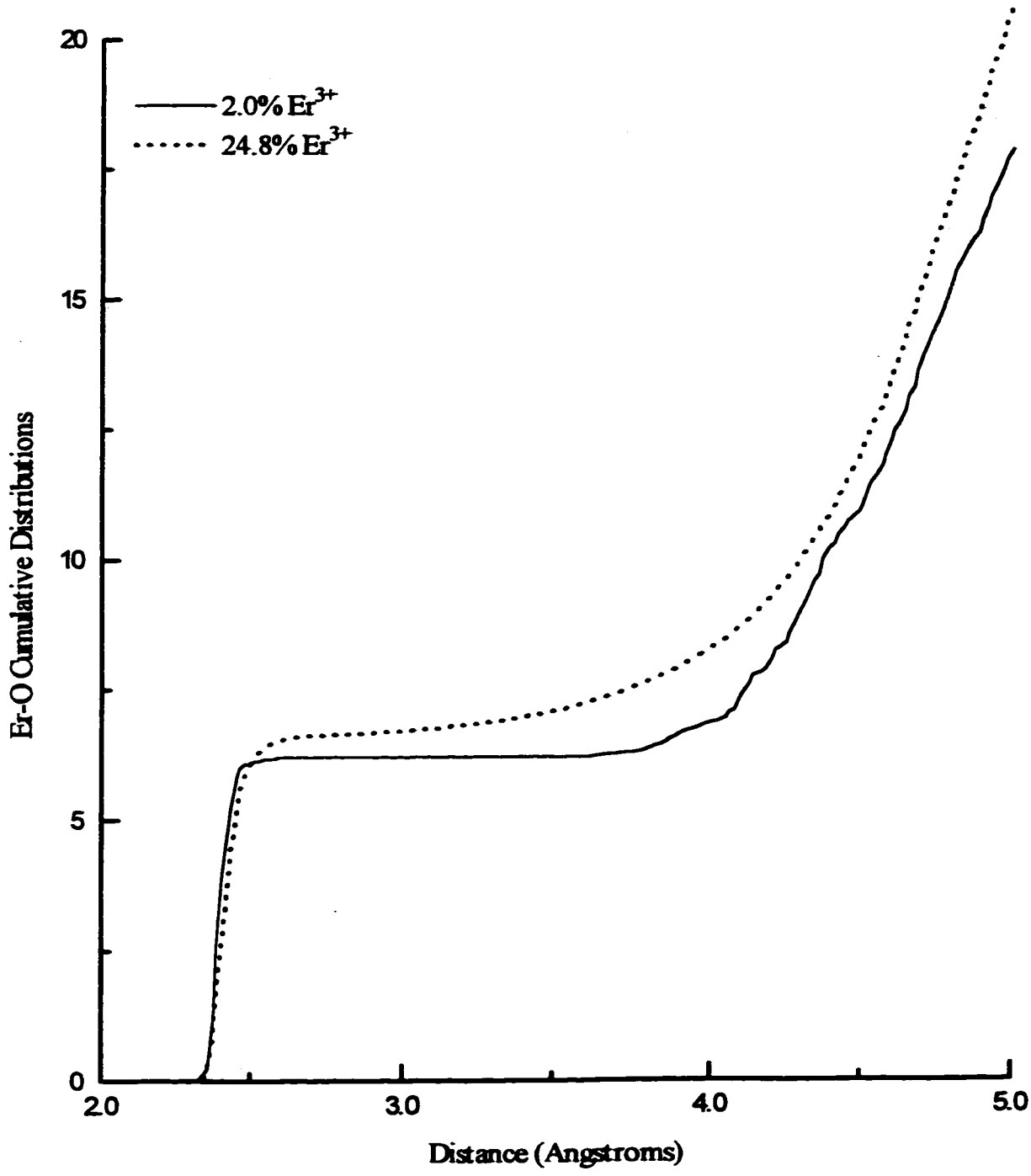

Figure 5.1.5.1b. Cumulative distribution functions of the Er-O ionic pair for the simulated 2.0% Er^{3+}:$PbO{\cdot}SiO_2$ glass (solid line) and the 24.8% Er^{3+}:$PbO{\cdot}SiO_2$ glass (dashed line).

The average number of oxygens surrounding the erbium ions for the first coordination shell for each of the aforementioned concentrations is reported in Table 5.1.5.1. An increase in the concentration of Er^{3+} in the glass causes an increase in Er-O coordination. This increase in coordination may be due to an increased amount of erbium-erbium clustering, which effectively allows the erbium ions to share oxygens in the same coordination sphere (3.2Å).

Table 5.1.5.1.

Average Er^{3+} coordination number for the erbium-oxygen first coordination shell (3.2 Å) for X% doped $PbO{\cdot}SiO_2$ simulated glass.

Er^{3+} Concentration (X%)	Average Coordination number
0.2	6.0
2.0	6.2
5.2	6.5
11.0	6.6
24.8	6.8

Figure 5.1.5.2. shows that erbium-erbium clustering in the glass is observed at concentrations as low as 2.0% Er^{3+}. As expected, clustering is more prevalent in the 24.8% Er^{3+}-doped lead silicate glass (Figure 5.1.5.3.).

In order to quantify the effect of clustering, the erbium ions were investigated by using Stauffer's [157] approach to percolation theory. Percolation theory is a mathematical approach describing a large number of physical phenomena ranging from forest fires to liquids passing through a porous medium.

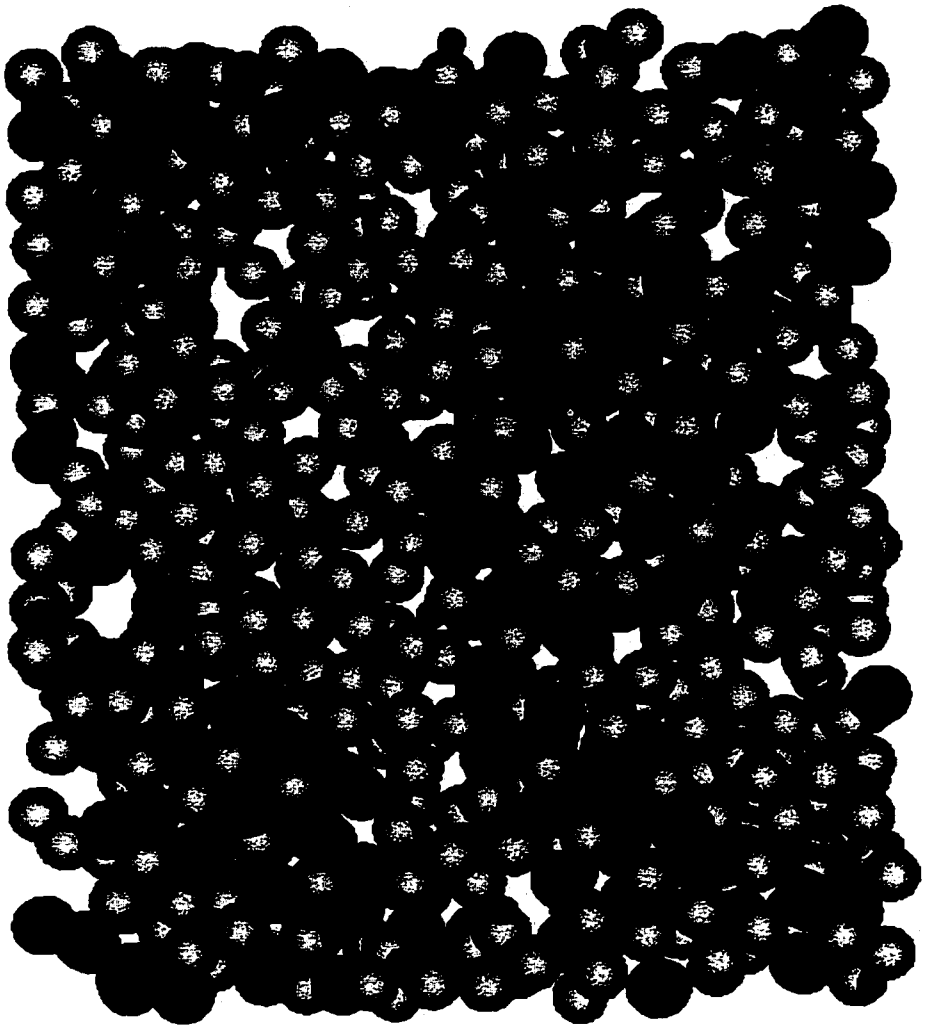

Figure 5.1.5.2. Computer graphics of a slice (xy) of the simulated 2.0% Er^{3+}:$PbO{\cdot}SiO_2$ glass. The black spheres represent the erbium ions, the red spheres represent the lead ions, the small green spheres represent the silicon ion, and the blue-gray spheres represent the oxygen ions.

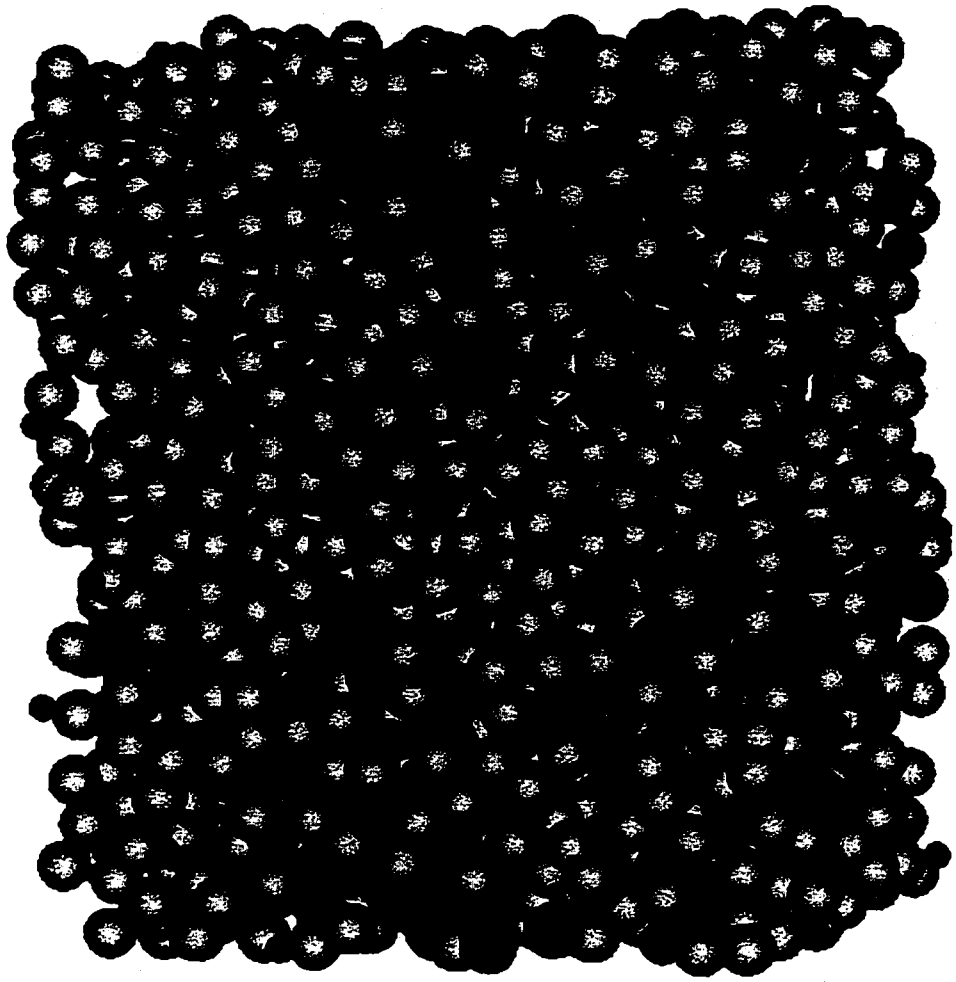

Figure 5.1.5.3. Computer graphics of a slice (xy) of the simulated 24.8% Er^{3+}:$PbO{\cdot}SiO_2$ glass. The black spheres represent the erbium ions, the red spheres represent the lead ions, the small green spheres represent the silicon ion, and the blue-gray spheres represent the oxygen ions.

In this study, the general ideas underlying the percolation theory are employed to study the erbium-erbium clusters in the three-body 2.0% Er^{3+}-doped lead silicate glass, based on a critical interparticle distance, RCL (r_c). Due to the low number of erbium ions present in the 2.0% Eu^{3+}-doped lead silicate glass (20 Er^{3+} ions), the number of overall ions in the glass was doubled to 5040 ions (results in 40 Er^{3+} ions) and 5 different configurations at 300K were generated in order to ensure statistical reproducibility. The RCL distance sets the boundaries of a cluster and any interactions between the erbium ions outside of this distance are neglected [158].

If 40 erbium ions are randomly placed in a box of 45.53 Å of side, the average distance between the ions is 13.31Å. For an ion to be contained in a cluster implies that two ions are close together, therefore, 13.31Å represents the closest distance between two ions in a perfect lattice. The MD configurations of the erbium ions at 300K, generated using the three-body potential model, was used as an input file for a FORTRAN program designed to examine clustering by isolating ion clusters within a given configuration. The ions are contained in a box of unit length centered at the origin. The classification algorithm begins by sorting N number of ions into clusters, whereby a critical cluster radius (r_c) defines the boundaries of a given cluster, and then the number of ions within each cluster is counted. More precisely, a cluster C (relative to r_c) of ions, from the total number of N ions of a system in a given configuration is defined as follows and C is a cluster if and only if the following conditions are met [158]:

(1) If $i \in C$ and $r_{ij} \leq r_c$ then $j \in C$

(2) If A is any set satisfying (1), and if i is in both A and C, then $A \cap C = C$ (where $\cap$ indicates set intersection)

The distance between particles i and j is denoted by rij. Condition (2) guarantees that a cluster, *C*, is not comprised of two or more disjoint groups that are separated by a distance greater than r_c [158]. The critical cluster radius, r_c, is varied in order to determine the distance at which all of the erbium ions are contained in one main cluster. The number of clusters was counted for distances from 1Å to 15Å in increments of 0.25 Å. For a given erbium ion in a specific cluster, the program verifies all cluster members (ions) against all other possible members before proceeding to other clusters. The average number of erbium ions clustered for the five configurations at varying r_c distances, is illustrated in Table 5.1.5.1.

Table 5.1.5.1.

The average number of Er^{3+} ions clustered at varying RCL (r_c) distances

Distance (Angstroms)	Number of Er^{3+} ions clustered
4.0	3.0
5.0	9.6
6.0	14.2
7.0	20.8
8.0	29.0
9.0	32.2
10.0	34.0
11.0	37.2
12.0	38.0
13.0	39.4
14.0	39.8
15.0	40.0

Figure 5.1.5.1. shows the average number of erbium ions clustered versus all calculated RCL (r_c) distances for the five Er^{3+} configurations.

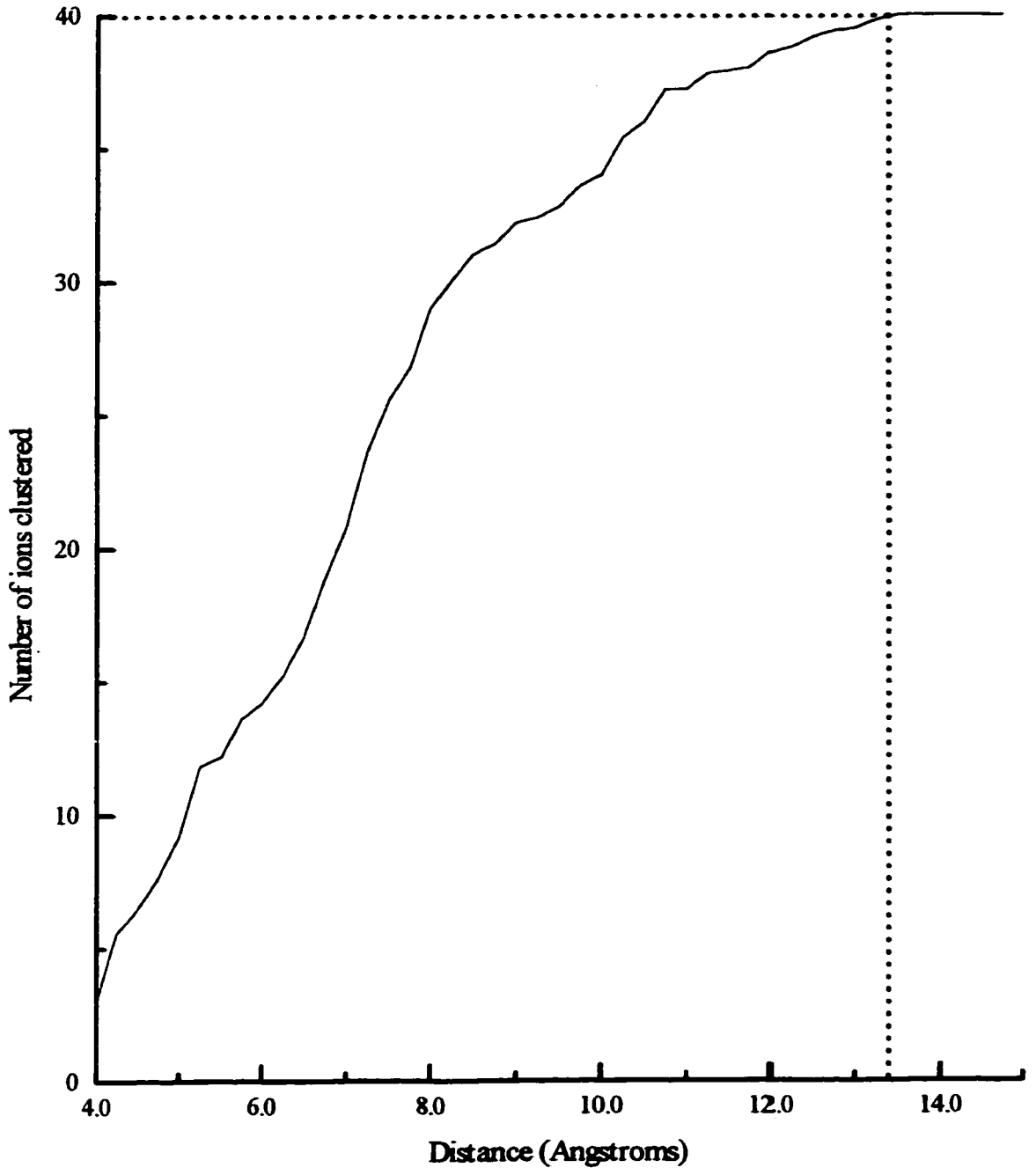

Figure 5.1.5.1. Graphical representation of the average critical cluster distance, r_c (dashed line) for five different configurations of 40 Er^{3+} ions.

In terms of a statistical correlation, it was expected that the critical cluster distance of the glasses would be close to that of the perfect lattice (13.31 Å). As seen by the plateau in Figure 5.1.5.1., the erbium ions are contained in one main cluster at approximately 13.35 Å, in excellent agreement with the perfect lattice which predicted a distance of 13.31Å.

The aforementioned results illustrated the occurrence of clustering, but not the evolution of clustering with respect to distance. Is the glass made up of a large number of small clusters or a small number of large clusters? In order to quantify this concept, the distribution of clusters was examined over five distances with identical intervals. (see Table 5.1.5.2.). The range of distances was chosen to be in the center of the cluster region such that the number of clusters is sufficiently large enough to yield a random cluster size distribution. This range was chosen due to the fact that distances that are too close to 4.0 Å would result in the erbium ions having clusters of one and distances approaching the critical cluster distance (13.35 Å) would consist of erbium ions in very large cluster groups. The number of cluster types for a given cluster group at specific cluster distances is shown in Table 5.1.5.2.

The results in Table 5.1.5.2. indicate that the glasses are made up of a large number of small clusters and not a small number of large clusters. These results are in good agreement with the CDF (Figure 5.1.5.1b.) and the pictorial representation of the 2.0% Er^{3+}-doped lead silicate glass (Figure 5.1.5.2.).

Table 5.1.5.2.

Average* Er^{3+}-Er^{3+} cluster patterns for the 2.0% Er^{3+}-doped lead silicate glasses

Distance	Average distribution of cluster types									
(Å)	1	2	3	4	5	6	7	8	9	10
5.0	28	3	1	-	-	-	-	-	-	-
6.0	26	4	2	-	-	-	-	-	-	-
7.0	18	5	4	-	-	-	-	-	-	-
8.0	10	3	4	3	-	-	-	-	-	-
9.0	6	1	1	5	-	-	-	1	-	-
10.0	3	1	1	5	-	-	-	-	-	1

* Represents the results of the five simulated configurations

Stauffer [157] states that the percolation processes can either be 'random' or 'correlated'. For the purpose of this study, correlation refers to the positioning of a given erbium ion due to the influence of its neighbours. At present it is not possible to ascertain whether or not correlation between ions exists in the glasses. This effect is very important since the primary reason for examining the clustering of erbium ions was to investigate the possibility of intercluster and cluster-to-cluster energy transfer, which becomes significant due to the fact that the rate of energy transfer is speculated to greater within a cluster than from cluster-to-cluster. In order to quantify these speculations, further studies such as examining the spatial structure of the cluster distributions, would be required.

The concentration study of Er^{3+}-doped lead silicate glass showed that erbium-erbium clustering was observed at concentrations as low as 2.0% Er^{3+}. Moreover, it was found that an increase in the concentration of Er^{3+} in the glass causes an increase in Er-O

coordination, which may be due to the increased amount of erbium-erbium clustering observed at the higher Er^{3+} concentrations. Employing Stauffer's [157] approach to percolation theory the average critical cluster distance, for the 2.0% Er^{3+}-doped lead silicate glass, was determined to be 13.35 Å and it was found that the glass consists of a large number of smaller erbium-erbium clusters and not a small number of large clusters.

5.2 SPECTROSCOPY OF THE SIMULATED AND EXPERIMENTAL RARE-EARTH DOPED LEAD SILICATE GLASSES

In this section of the thesis, the correlations between the local rare-earth environment and the calculated emission spectra of Eu^{3+} and Er^{3+} doped in lead silicate glass are examined. The emission spectra were generated using a point-charge crystal-field model that includes J-mixing, which was originally developed for doped crystalline materials [109]. This method was used previously by Cormier et al. [57,45] to generate the absorption and emission spectra of Eu^{3+}:Na_2O-$2SiO_2$ glass and with slight modification, by Chaussedent et al. [61,62] to generate the emission spectrum of Eu^{3+} in aqueous solution.

In summary, the general method can be described as follows. From the configurations generated by the MD simulations, the crystal-field parameters are generated since, by knowing the position and charge of each ion in the glass, the electrostatic potential at the rare-earth site can be calculated. The crystal-field parameters are then used to calculate the energy splitting of each J-manifold and the transition probabilities. Lastly, the simulated emission spectra are obtained and compared with the corresponding experimental spectra.

The crystal-field model used in this thesis is same as that used by Cormier et al. [57] but with several important modifications, as suggested by the work of Chaussedent et al. [61,62]. The computational model, as well as the necessary assumptions made, is outlined in the following section.

5.2.1. The computational model

5.2.1.1. Point-charge crystal-field model

The three-body potential model uses the full ion charge and introduces "covalency" in terms of bond directionality for the silicon-oxygen and lead-oxygen ion pairs, interactions with the rare-earth ions were all electrostatic (ionic).

Contrary to the three-body potential model, the covalent interactions between the *f* electrons of the RE^{3+} ion and host lattice were introduced in the crystal field calculation by considering the effective charges of the ions instead of the formal charges. Karayianis and Morrison [159] found that the introduction of partial charges had a significant effect on the fitting of experimentally obtained energy levels. They stated that the inclusion of partial charges in the crystal-field calculation reduces the magnitude of the electrostatic interaction between ions and leads to a simulation of the effects of covalency. It is important to note, however, that this does not involve the introduction of an actual covalency term into the crystal-field calculation [45]. The effective charges, employed in this thesis, were calculated using the following equation:

$$V_{ij}^{BMH}(R_{MIN}) = \frac{e^2 q_i q_j}{R_{MIN}} \qquad 5.2.1.1.1.$$

where,

$$\left(\frac{\mathrm{d}V_{ij}^{BMH}}{\mathrm{d}R}\right)_{R=R_{MIN}} = 0 \qquad 5.2.1.1.2.$$

The simulation of the Eu^{3+} and Er^{3+} emission spectra was performed with the following effective charges: (i) oxygen -0.8788, (ii) silicon=1.9775, (iii) lead=0.6553 and (iv) europium and erbium = 1.0717.

5.2.1.2. Point symmetry of the RE^{3+} ion

The disordered nature of glasses imposes that the lowest possible symmetry should be employed, that is, the point symmetry of the rare-earth ion sites should be regarded as C_1. Calculations performed using C_1 symmetry are not restricted by the selection rules and as a result, most researchers found that simple point-charge crystal-field calculations became too time consuming.

Cormier et al. [57] successfully generated the absorption and emission spectra of Eu^{3+} in sodium disilicate glass using a C_{2v} point group symmetry. Their reasons for choosing a C_{2v} symmetry were the same as those initially proposed by Brecher and Riseberg [49,50]. First, C_{2v} symmetry is the highest symmetry for which the full splitting of the $^7F_1$ and $^7F_2$ levels is accounted for (see Table 3.3.2.). In other words, although the choice of a higher symmetry would reduce the calculation of contributing parameters, it does not permit a complete calculation of all participating Stark sub-levels. Second, C_{2v} symmetry is a subgroup of almost all of the higher point symmetry, thus allowing for the application of the descending symmetries technique [139,140]. Third, it was the lowest symmetry for which simple crystal-field calculations could be performed without taxing the workstations.

Although a considerable amount of information can still be obtained, it must be noted that using a C_{2v} point group symmetry is an approximation. As a result of this approximation, there are several B_{kq} parameters with odd q that are considered to be zero

and are thus neglected. In reality, however, these parameters are not zero and may contribute significantly in the calculation of the energy levels. This effect is most notable in the simulation of the $^5D_0 \rightarrow {}^7F_2$ transition in the Eu^{3+}-doped sodium disilicate glass by Cormier et al. [57]. Although the overall intensity of the simulated transition was acceptable, the authors were unable to reproduce the observed intensity distribution of the five Stark components of this transition.

In the simulation of the emission spectrum of Eu^{3+} in aqueous solution, Chaussedent et al. [61,62] used a C_1 point group symmetry, which involved the calculation of twenty-seven B_{kq} and thirty-six A_{kq} parameters. The simulated spectrum was in better agreement with the experimental spectrum, but the most important improvement was in the simulation of the $^5D_0 \rightarrow {}^7F_2$ transition. In C_1 symmetry, the selection rules do not play an important role, and the mixing of the states becomes more important with the effect that the calculation of the intensities takes into account all of the radiative transitions possible.

Due to the marked improvement in the simulated emission spectrum of Eu^{3+} by Chaussedent et al. [61,62], a C_1 point group symmetry was also employed in this thesis for the generation of the emission spectra of the Eu^{3+}- and Er^{3+} -doped lead silicate glasses.

5.2.1.3. Calculation of the crystal-field parameters

The fact that the B_{kq} parameters for values of $k > 2$ are completely convergent would indicate that the crystal-field calculations could be limited to ion-ion interactions within the first coordination sphere. However, there are two important parameters, A_{1q} and B_{2q}, which do not converge at the first coordination sphere distances [111].

In order to rectify this problem, Cormier et al. [57] included all the ions in their simulated ensemble since they found that B_{2q} parameters converged to a given value only after 12 Å. This approach proved to be effective since the total number of ions in each configuration was 600, which could be contained within the limits of the distance cutoff. However, they did not make any adjustments to the A_{1q} parameters.

Chaussedent [62] introduced an correction function to take into account the error incurred from the summation over all ions within the boundaries of the simulation box. Their method involved a truncation of the electrostatic interaction potential after a certain distance, r_c. The electrostatic interaction potential was corrected by multiplying by a function, $f(r)$ which is equal to zero at distances $r \geq r_c$, such that value of r_c was chosen to be less than half the MD box length. The function, $f(r)$, therefore, modified the potential function for all interactions within the range of $r = 0$ to $r = r_c$.

In order to avoid complications due to long range interactions, the correction function must be taken into account for the calculation of the A_{kq} parameters where $k = 1$ and 2 such that, the dipolar component of the crystal-field parameter is related to A_{1q} as follows:

$$\begin{aligned} E_x &= -\sqrt{2}/e\,\mathrm{Re}(A_{11}) \\ E_y &= -\sqrt{2}/e\,\mathrm{Im}(A_{11}) \\ E_x &= 1/e\,A_{10} \end{aligned} \qquad \text{5.2.1.3.1.}$$

and,

$$E = -e\sum_j q_j \frac{R_j}{R_j^3}, \quad \text{where } E_j = -\nabla V_j \qquad \text{5.2.1.3.2.}$$

The correction factor $f(r)$ is introduced into the electrostatic potential as follows:

$$V_j = eq_j \frac{f(R_j)}{R_j} \qquad 5.2.1.3.3.$$

such that,

$$E = \sum_j eq_j \frac{R_j}{R_j^3} S(R_j) \qquad 5.2.1.3.4.$$

where,

$$S(r) = f(r) - r\frac{df(r)}{dr} \qquad 5.2.1.3.5.$$

Similarly to A_{1q}, the second-order B_{2q} parameters were also calculated by including the tensoral elements of the quadrupole parameters with the correction function as follows:

$$B_{20} = \frac{e\rho_2}{2} Q_{zz}$$

$$\mathrm{Re}(B_{21}) = -\frac{e\rho_2}{\sqrt{6}} Q_{xz}$$

$$\mathrm{Im}(B_{21}) = -\frac{e\rho_2}{\sqrt{6}} Q_{yz} \qquad \text{5.2.1.3.6.}$$

$$\mathrm{Re}(B_{22}) = \frac{e\rho_2}{2\sqrt{6}} (Q_{xx} - Q_{yy})$$

$$\mathrm{Im}(B_{22}) = \frac{e\rho_2}{\sqrt{6}} Q_{xy}$$

with,

$$Q_{\alpha\beta} = \sum_j \frac{e q_j}{R_j^3} \left[\left(\frac{3 X_j^\alpha X_j^\beta}{R_j^2} - \delta_{\alpha\beta} \right) S(R_j) + X_j^\alpha X_j^\beta f''(R_j) \right] \qquad \text{5.2.1.3.7.}$$

where, $\delta_{\alpha\beta}$ is the Kronecker delta and $f' = d^2/dr^2 f(r)$.

Chaussedent [62] found that in using equation 5.2.1.3.6. to calculate the B_{2q} parameters, all the second-order terms converged. Moreover, by forcing the long-range electrostatic interactions to approach zero at $r = r_c$, the long range screening effect due to the charges is taken into account.

The correction function used in the calculations can be expressed by the following equations:

$$S(r) = \begin{cases} 1 - 2\left(\frac{r}{r_c}\right)^2 + \left(\frac{r}{r_c}\right)^4 & r < r_c, \\ 0 & r \le r_c \end{cases} \qquad \text{5.2.3.1.8.}$$

Differentiating equation 5.2.3.1.5., the correction function is given as:

$$f(r)=\begin{cases}1-\dfrac{8}{3}\dfrac{r}{r_c}+2\left(\dfrac{r}{r_c}\right)^2-\dfrac{1}{3}\left(\dfrac{r}{r_c}\right)^4 & r<r_c,\\ 0 & r\le r_c\end{cases} \qquad 5.2.3.1.9.$$

The intensity of an electric dipole allowed transition, such as the $^5D_0 \rightarrow {}^7F_2$ transition in Eu^{3+}, is dependent on the A_{kq} parameters, particularly the A_{1q}. The problems with the intensities of the individual Stark component for the $^5D_0 \rightarrow {}^7F_2$ transition in the simulated model by Cormier et al. [57] could also be due to the lack of a correction term for the A_{1q} parameters. Chaussedent [62] shows a better agreement with the experimental spectrum for the same transition. Therefore, the crystal-field model in this thesis employed the aforementioned correction factor in calculating the A_{1q} and B_{2q} parameters.

5.2.2. The simulated and experimental emission spectra of Eu^{3+}

5.2.2.1. The emission spectrum

Figure 5.2.2.1.1. shows the experimental (solid line) and simulated (dashed line) emission spectrum of the $^5D_0 \rightarrow {}^7F_J$ (J = 0,4) transitions for the 2.0% Eu^{3+}-doped lead silicate glass. The room temperature experimental emission spectrum was obtained by exciting at 514.5 nm, that is, directly into the $^5D_1 \leftarrow {}^7F_0$ absorption band. Excitation at 514.5 nm ensures that the full ensemble of Eu^{3+} ions will be excited [45]. The simulated emission spectrum is calculated from 10 different configurations at 300K, representing a total of 200 Eu^{3+} ions.

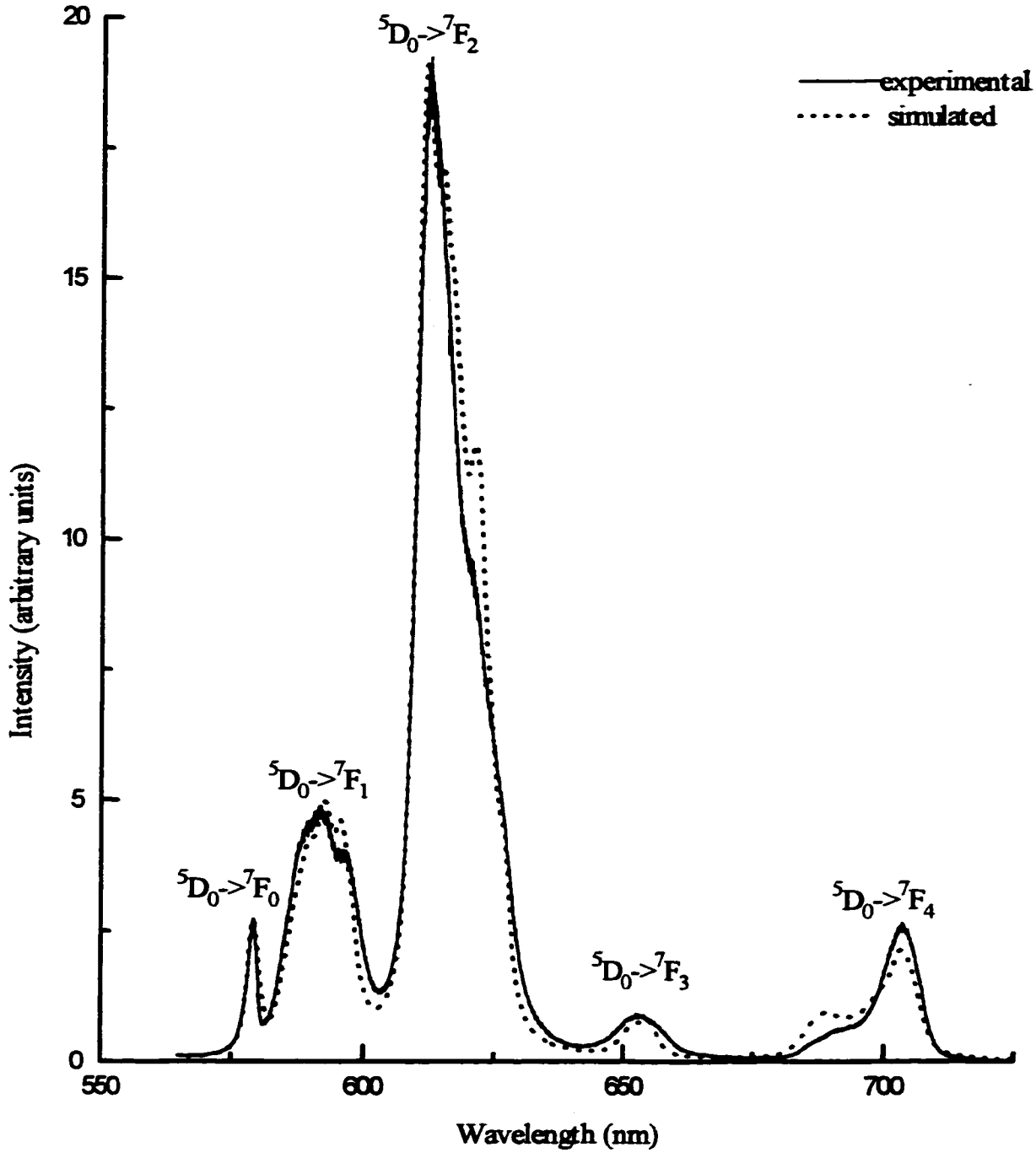

Figure 5.2.2.1.1. Comparison between the room temperature $^5D_0 \rightarrow ^7F_J$ (J=0,4) emission spectra of experimental and simulated Eu^{3+}-doped lead silicate glass.

A good agreement exists with respect to the overall positions and energy level splittings between the simulated and experimental spectra. In particular, the $^5D_0 \rightarrow {}^7F_0$, $^7F_1$ and $^7F_3$ transitions are qualitatively in very good agreement with the experimental spectrum. The most noticeable improvement in the simulated spectrum occurs for the $^5D_0 \rightarrow {}^7F_2$ transition. Recall, that in the simulations by Cormier et al. [57] the individual intensities of the Stark components were in poor agreement with the experimental spectra. Although there are still some slight differences between the simulated and experimental spectra in the present model, it is not unexpected since it is more difficult to simulate electric dipole transitions. Both Cormier et al. [57] and Chaussedent [62] attributed the differences between the experimental and simulated spectra to be largely due to the fact that the simulations are of a "static" spectrum, where the amorphous environment only provides a static average electrostatic field. Dynamical processes, such as vibronic coupling or energy transfer, which effect the laboratory glass, are absent in the simulated spectrum. Kuroda et al. [162,163] stated that the presence of dynamic coupling and in particular the inclusion of the polarizability is essential in the proper calculation of the electric dipole intensity distribution of transitions which exhibit quadrupole-dipole coupling mechanisms, such as the $^5D_0 \rightarrow {}^7F_2$ transition.

The same effect is seen with respect to the other electric dipole transition, $^5D_0 \rightarrow {}^7F_4$. The position of this transition (simulated spectrum) is in good agreement with the experimental spectrum, but the intensities are slightly different. The simulation, however, was successful in reproducing the asymmetry found in this transition. This is another improvement to the model by Cormier et al. [57], which did not simulate the asymmetry present in the electric dipole transition. Moreover, introduction of the

correction term for the A_{1q} parameters has resulted in a considerable improvement to both of the electric dipole transitions, namely, the $^5D_0 \rightarrow {}^7F_2$, $^7F_4$ transitions in the simulated Eu^{3+}-doped lead silicate glass.

In general, the $^5D_0 \rightarrow {}^7F_1$ transition is very sensitive to the local structure of the rare-earth ion. The removal of the degeneracy of the levels in this transition is due entirely to the B_{2q} parameters. Thus, the corrections made to the B_{2q} parameters were successful, since there is a good agreement between the simulated and experimental spectra.

In summary, the assumptions made in the crystal-field model resulted in a simulated emission spectrum, which is in good agreement with the experimental spectrum.

5.2.2.2. Spectra-structure relationships

One of the primary goals of optical spectroscopists is to be able to infer structural information from experimentally obtained spectra, while computational chemists continually search for validation of their structural models. Coupling the strengths of both fields of research, we have refined a tool that could shed a new light on the role of dopants in optical materials.

The experimental emission spectrum represents the average contribution of all the local environments of the rare-earth ion. In the Eu^{3+}-doped lead silicate glass, the europium ions were found to have an average coordination of 6.5 nearest neighbour oxygens, with the major geometrical contributions being a distorted six-coordinated octahedron and a distorted seven coordinated pentagonal bipyramid (see section 5.1.3.). Figure 5.2.2.2.1. shows the simulated emission spectrum for Eu^{3+} as well as the simulated emission spectrum for the pure six-coordinated Eu^{3+} ions (inset-top) and the simulated emission spectrum for the pure seven-coordinated Eu^{3+} ions (inset-bottom).

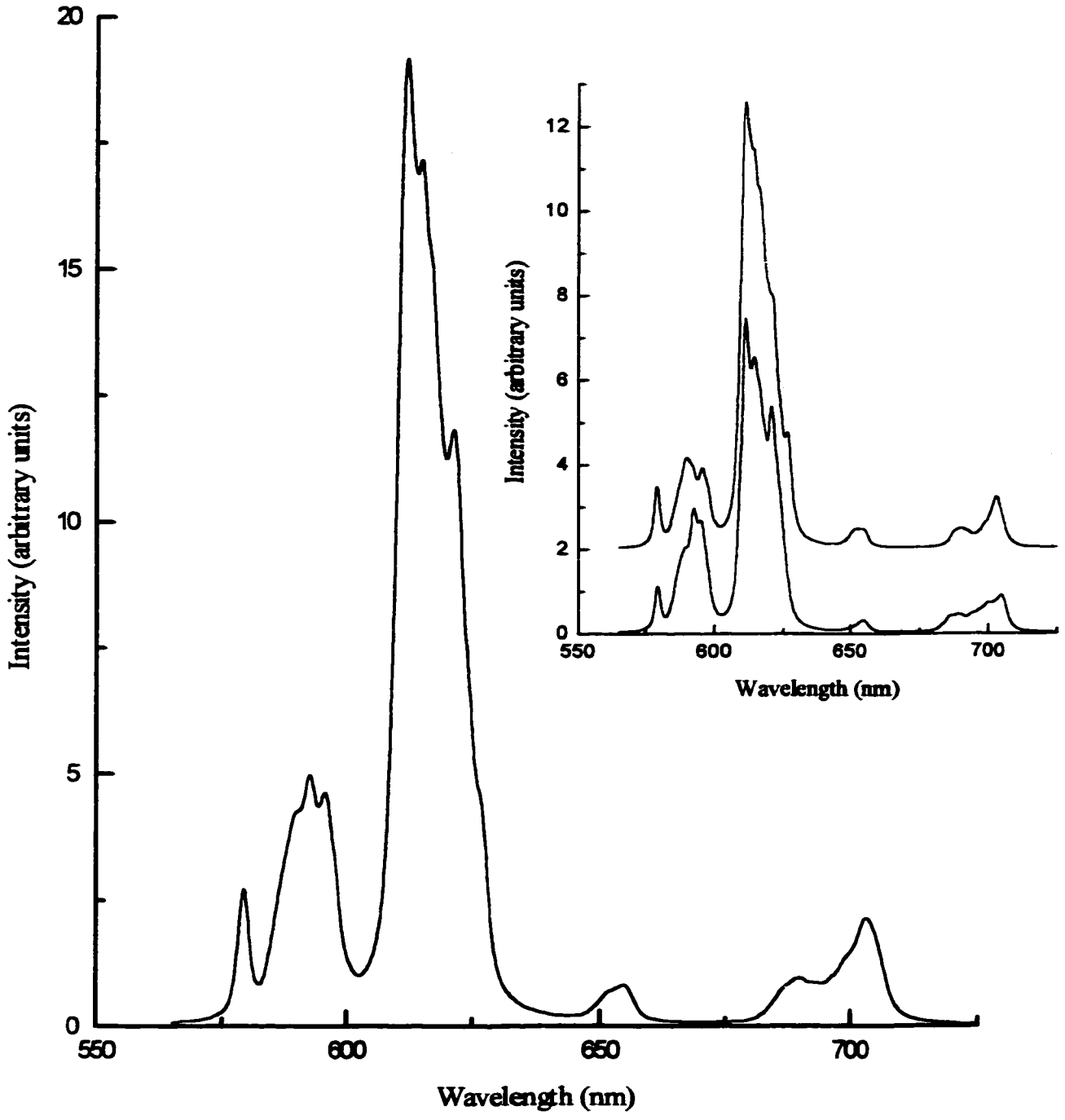

Figure 5.2.2.2.1. Simulated emission spectra for Eu^{3+}-doped lead silicate glass. Inset shows the simulated spectrum of six-coordinated Eu^{3+} (top) and the simulated spectrum of seven-coordinated Eu^{3+} (bottom).

The simulated spectra of the six and seven coordinated Eu^{3+} ions show a major difference in the $^5D_0 \rightarrow {}^7F_2$ transition. This transition shows more spectral features for the seven coordinated Eu^{3+} ions. We postulate that for the seven coordinated species the crystal-field is stronger, thus splitting the J levels to a greater extent.

Comparison of the simulated and experimental emission spectra in the previous section (5.2.2.1.) indicated that the MD simulation is an accurate description of the Eu^{3+}-doped lead silicate glass. The most important feature of Figure 5.2.2.2.1. is that we are able, with confidence, to simulate the emission spectra of a rare-earth ion with respect to the distinct structure of the local environments.

5.2.3. The simulated and experimental emission spectra of Er^{3+}

Figure 5.2.3.1. shows the experimental (solid) and simulated (dashed) emission spectra for the $^2H_{11/2} \rightarrow {}^4I_{15/2}$ and the $^4S_{3/2} \rightarrow {}^4I_{15/2}$ transitions for the Er^{3+}-doped lead silicate glass. The room temperature experimental emission spectrum was excited at 488 nm. The simulated emission spectrum represents 10 different configurations obtained from the MD simulation at 300K, which represents 200 Er^{3+} environments.

Overall, a fair agreement has been obtained between the experimental and simulated emission spectra for Er^{3+}. In the case of the $^2H_{11/2} \rightarrow {}^4I_{15/2}$ transition (see Figure 5.2.3.1.), the position and energy splittings of the peak is quite good but the intensity is too high. For the $^4S_{3/2} \rightarrow {}^4I_{15/2}$ transition, the intensity and overall position of the peak are quite good, but the energy splitting is not accurate. Due to the increased number of energy levels in the Er^{3+} ion, the emission spectrum is much more difficult to simulate than that of Eu^{3+}. However, there are additional factors that contribute to the complexity of the Er^{3+}

spectrum. Experimentally, non-radiative processes such as multiphonon relaxation or energy transfer are operative from the $^2H_{11/2}$ and $^4S_{3/2}$ energy levels [24]. As previously mentioned, the simulated spectrum is a "static" spectrum and any dynamical processes which effect the experimental spectrum will be absent from the simulated spectrum. In order to obtain a better representation of the Er^{3+} spectrum, the dynamics of the system must be incorporated into the calculation.

Figure 5.2.3.2. shows the experimental (solid) and simulated (dashed) emission spectra for the $^4I_{13/2} \rightarrow {}^4I_{15/2}$ transition (laser transition) for the Er^{3+}-doped lead silicate glass. The room temperature experimental emission spectrum was excited at 488 nm and was autophased on the $^4I_{13/2}$ transition in order to maximize the 1.5μm band. The simulated emission spectrum is a contribution of 10 different configurations obtained from the MD simulation at 300K, representing 200 Er^{3+} environments.

The simulated model fails to accurately reproduce the $^4I_{13/2} \rightarrow {}^4I_{15/2}$ transition. As shown in Figure 5.2.3.2., the overall intensity of the $^4I_{13/2} \rightarrow {}^4I_{15/2}$ transition is adequate, however, we were unable to reproduce the intensity distribution of the Stark components. In an upconversion study of Er^{3+}-doped lead silicate glass, Capobianco et al. [24] propose an upconversion mechanism due to the sequential absorption of photons from the metastable $^4I_{13/2}$ state to explain their experimental results. Therefore, due to the lack of a dynamical contribution, the present simulated model is unable to represent the occurrence of such processes as upconversion.

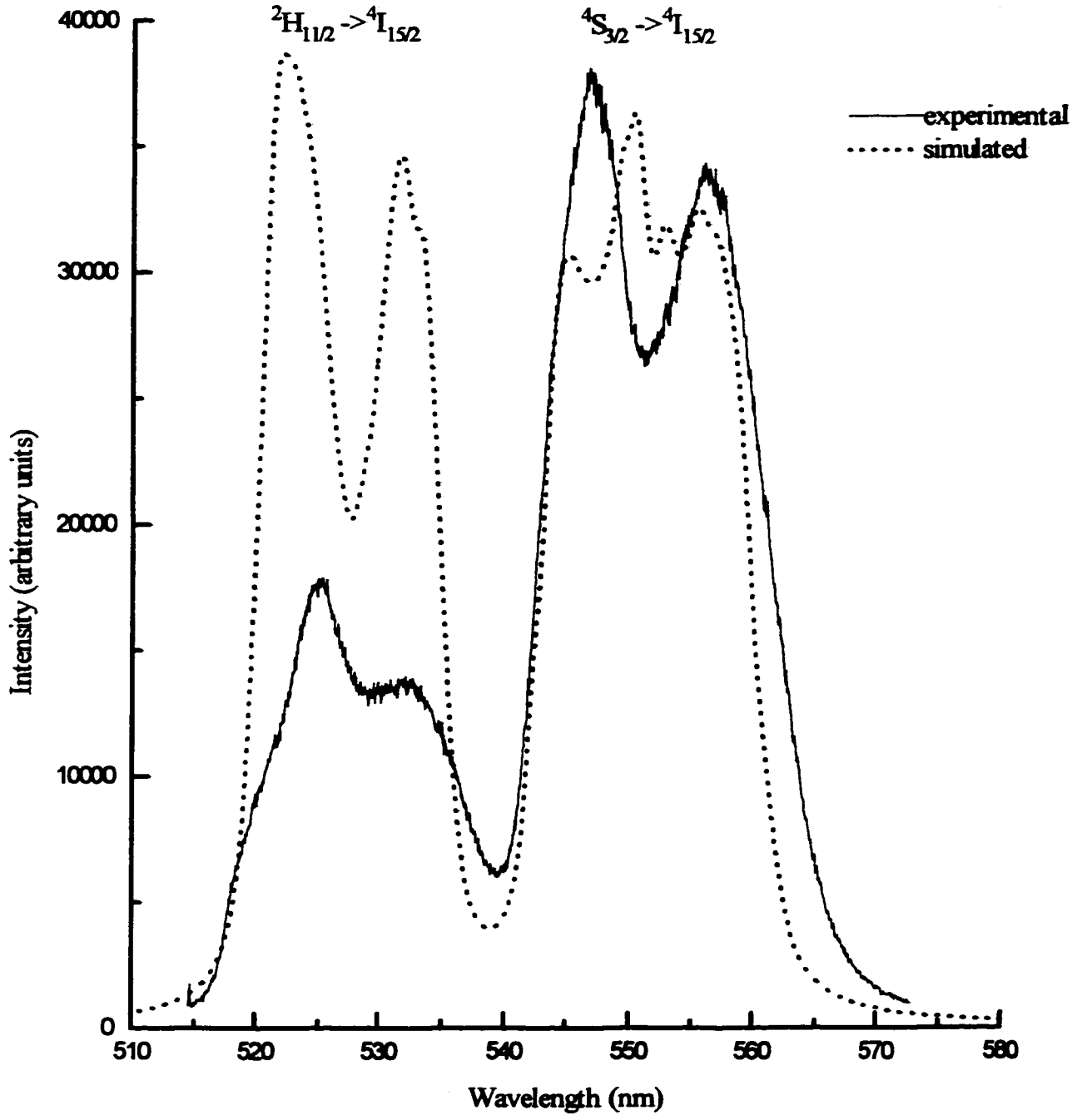

Figure 5.2.3.1. Comparison between the room temperature $^2H_{11/2} \rightarrow {}^4I_{15/2}$ and $^4S_{3/2} \rightarrow {}^4I_{15/2}$ emission spectra of experimental and simulated Er^{3+}-doped lead silicate glass.

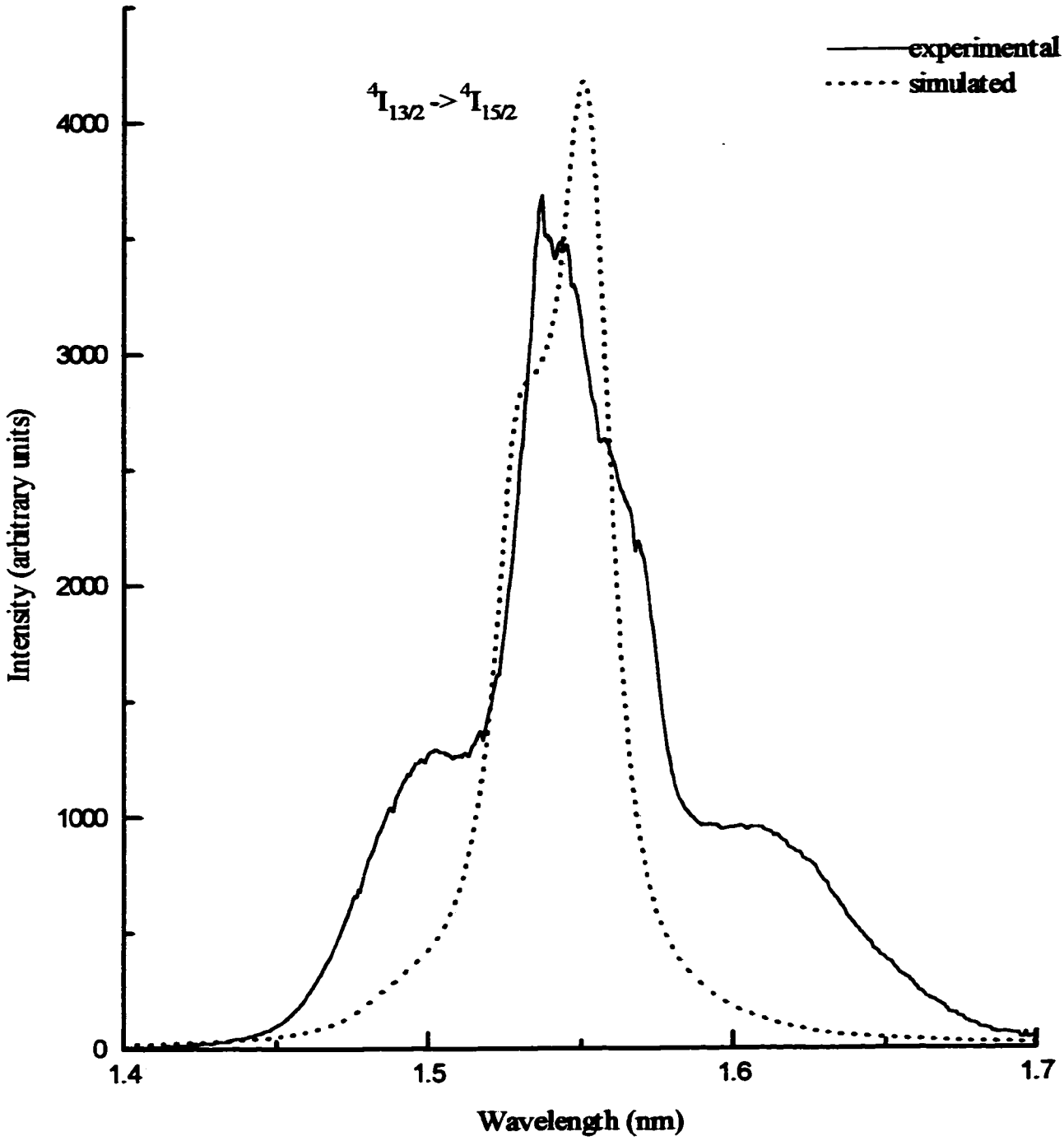

Figure 5.2.3.2. Comparison between the room temperature $^2I_{13/2} \rightarrow {}^4I_{15/2}$ emission spectra of experimental and simulated Er^{3+}-doped lead silicate glass.

In order to resolve such discrepancies in the Er^{3+} transitions, a more sophisticated crystal-field model is required to account for the dynamical process present in the glass. Although still in the developmental phase, the model proposed to examine clustering and energy transfer between erbium ions (see section 5.1.5.) should provide the necessary information on the dynamical processes occurring within the 2.0% Er^{3+}-doped lead silicate glass.

CHAPTER 6

6.0 THE WRAP UP: CONCLUSIONS AND FUTURE WORK

6.1 CONCLUSIONS

Optical spectroscopic methods have been commonly employed to investigate the local structure of rare-earth ions doped in inorganic materials in an attempt to better understand the influence of the matrix on the luminescence of the rare-earth ions. However, these methods only provide average structural information and a more detailed description of the local environment of the rare-earth ions is necessary. The use of computational techniques, such as molecular dynamics, provides information at the microscopic level, and has been used extensively in recent years to investigate the local structure of doped inorganic glasses. Moreover, coupled with a point-charge crystal-field model, the MD technique has proved to be a very powerful tool in the simulation of the optical spectra of rare-earth ions doped in inorganic glasses.

In this thesis, we have focused our attention on developing a more realistic potential model to better describe the environment surrounding the rare-earth ion. The configurations generated from the MD simulations were used in a point-charge crystal-field model, as described by C_1 symmetry, to generate the emission spectra of the rare-earth ions. By refining both the aforementioned methods, we have developed a model that can isolate the individual geometrical RE^{3+} environments and calculate the individual emission spectra corresponding to each of the different geometrical arrangements. This in turn has allowed us to obtain a more complete description of the local structure of the RE^{3+} ion with respect to the overall emission spectrum.

Molecular dynamics techniques were employed to simulate undoped and rare-earth doped lead silicate glasses. The importance of simulating lead silicate glasses stems from the fact that high concentrations of PbO in the random network can drastically influence the spectroscopic behavior of the rare-earth ion, either by forcing the rare-earth ion into an uncommon coordination geometry, and/or by affecting its transition probabilities [24]. Moreover, in recent years, high technology applications such as nuclear scintillators and upconversion laser devices have demanded a greater understanding and control over these and other structurally related optical properties.

The first goal of this thesis was to examine the structure of undoped lead silicate glass using both a two-body and a three-body potential model. The two-body model used an electrostatic Born-Mayer Huggins (BMH) potential, while the three-body model was comprised of a modified two-body BMH potential and an additional three-body bonding term, to account for the partial covalency present in the Si-O and Pb-O ionic pairs. Structural features of the simulations of undoped $PbO{\cdot}SiO_2$ glass were found to be in excellent agreement with published experimental results. Nearest neighbour distances and average coordination numbers were in good agreement with those obtained from X-ray and neutron diffraction and EXAFS studies. The primary results from the study can be summarized as follows:

(i) The average silicon coordination was found to be 4.0 in both the two- and three-body simulated glasses.

(ii) The tetrahedral angle at $\approx 110°$ was sharper using the three-body model in comparison to the two-body simulated model.

(iii) From the pair and bond-angle distribution functions, it is evident that the three-body potential increased the local order around the silicon

ions. This can be seen by the well-defined tetrahedral units, the improvements to the Si-O-Si bond angle distributions and the lowering of bond defects.

(iv) In the three-body potential model the lead behaved as network formers which can been seen by the presence of the two distinct networks, a silicon rich region and a lead rich region; an effect which has also been observed experimentally. In contrast, in the two-body potential model the lead ions acted as typical network modifiers.

It can therefore be concluded that the simulated models are a good representation of the structure of undoped $PbO{\cdot}SiO_2$ glass and that the three-body potential model produced a marked improvement over the two-body potential model.

In order to obtain a better description of the effect of the lead ion in silicate glasses, the subsequent step in our analysis of the undoped lead silicate glass was to simulate glasses with low and high lead-oxide content. The three-body potential model was used since it was very successful in describing the structure of lead silicate glass (50mol% PbO). The following observations were made concerning the role of the lead ion at different PbO concentrations in lead silicate glass:

(i) It was found that at low PbO concentrations (22 mol% PbO), the lead ion behaved as a traditional modifier, with the lead ions distributed throughout the glass and low lead-oxygen coordination.

(ii) At 50 mol% PbO, the lead ion was found to behave as both a modifier and a former and the glass displayed two distinct networks; the silicate network and the secondary lead network.

(iii) In the high lead glass (70 mol% PbO), the lead ion behaved as a network former and an increase in PbO coordination was observed due to the lead ions sharing neighbouring oxygens. The presence of lead rich regions predominated in the glass and the two networks (silicon and lead) were connected via edge-sharing oxygens.

The structural features of the three simulated glasses were found to be in good agreement with experimental results.

Once a good description of the undoped glass was obtained, we proceeded to examine the local environment of the rare-earth ions in lead silicate glass. A 2.0% Eu^{3+}-doped lead silicate glass was simulated using the three-body potential. The simulation of Eu^{3+}-doped glass reproduced well bulk structural features such as interionic distances and average coordination numbers which were in good agreement with X-ray, neutron and EXAFS results. Moreover, as reported for the undoped glasses, the Eu^{3+}-doped glass also showed the presence of the two networks, the silicate network and the lead network.

The results of the simulation are summarized as follows:

(i) The Eu^{3+} ions were found primarily in the lead network, with only a modest presence in the silicate network, showing that the two cations (Pb^{2+}, Eu^{3+}) share similar environments.

(ii) The average coordination number of Eu^{3+} was found to be 6.5

(iii) Using a general-purpose program to superimpose the identical molecules of different configurations, it was found that two main geometrical arrangements exist for the Eu^{3+} ion: a six-coordinated distorted octahedral and a seven-coordinated distorted pentagonal bipyramid.

Since the spectroscopic properties of the dopant ions are dependent on the local environment, we performed an in depth investigation on first coordination sphere of three different rare-earth ions. Using the three-body potential model, Eu^{3+}-, Er^{3+}- and Yb^{3+}-doped lead silicate glasses were simulated. The conclusions are:

(i) The average coordination of the rare-earth ions was found to be 6.5 for Eu^{3+}, 6.2 for Er^{3+}, and 5.93 for Yb^{3+}.

(ii) From the simulations of the different rare-earth ions, the individual local environments specific to each of the dopants were isolated which is important due to the influence of the local environments on the spectroscopic properties of the dopant ions.

(iii) Illustrated the sensitivity of the three-body potential model to simulate small differences found in the rare-earth ions.

Although the differences in ionic radii, interionic distance and average coordination number between the three rare-earths was quite small, the three-body potential model successfully reproduced these differences in the bulk structural features, and the results were found to be in excellent agreement with experimental data.

We decided to perform a concentration study on the Er^{3+}-doped lead silicate glass in order to study the clustering of erbium ions, and to examine the possibility of intercluster and cluster-to-cluster energy transfer. This study was motivated by the recent observation of substantial room-temperature up-conversion from infrared to visible radiation in Er^{3+} doped and Er^{3+}/Yb^{3+} co-doped $PbSiO_3$ glasses [24]. In order to examine erbium-erbium clustering, glasses of the following Er^{3+} concentrations, 0.2%, 2.0%, 5.2%, 11.0% and 24.8% were simulated. In order to quantify the effect of clustering, the erbium ions were investigated using Stauffer's [157] approach to percolation theory.

The following can be concluded from our study:

(i) Erbium-erbium clustering was observed at concentrations as low as 2.0% Er^{3+}.

(ii) An increase in the concentration of Er^{3+} in the glass caused an increase in Er-O coordination. This effect is due to an increased amount of erbium-erbium clustering, which resulted in the erbium ions sharing oxygens within the same coordination sphere (3.2Å).

(iii) Employing Stauffer's [157] approach to percolation theory the average critical cluster distance, for the 2.0% Er^{3+}-doped lead silicate glass, was determined to be 13.35 Å.

(iv) The 2.0% Er^{3+}-doped lead silicate glass was found to consist of a large number of smaller erbium-erbium clusters and not a small number of large clusters.

A successful validation of the simulated structural model of the $PbO{\cdot}SiO_2{:}RE^{3+}$ glass was performed through a comparison between the room-temperature emission spectra of the experimental glass and the calculated emission spectra of the simulated glass. The simulated spectra were obtained using a point-charge crystal-field model, with a C_1 symmetry for the RE^{3+} environment. The splitting of the J manifolds, and the corresponding transition probabilities of the simulated RE^{3+} ions were also calculated.

The simulation of the $^5D_0 \rightarrow {}^7F_J$ (J=0-4) transitions in the Eu^{3+} ion spectra were found to be in good agreement with the experimental emission spectrum. The most noticeable improvement introduced using our model was the simulation of the $^5D_0 \rightarrow {}^7F_2$ transition. Prior simulations by other researchers, resulted in a poor agreement with the

experimental spectra for the $^5D_0 \rightarrow {}^7F_2$ transition. We attribute this improvement to the addition of a correction factor, which was used to calculate the A_{1q} and B_{2q} parameters, in our crystal-field model.

The most important conclusion in our simulations of the Eu^{3+} emission spectrum is that we were able, with confidence, to separate and simulate the emission spectra of a rare-earth ion based on the specific geometrical arrangements of the local environments.

Simulations of $^2H_{11/2} \rightarrow {}^4I_{15/2}$ and the $^4S_{3/2} \rightarrow {}^4I_{15/2}$ transitions in the Er^{3+} ion were found to be in moderate agreement with the corresponding room temperature experimental spectrum. Similarly, simulation of the $^4I_{13/2} \rightarrow {}^4I_{15/2}$ transition in Er^{3+} was found to be in poor agreement with the experimental room temperature emission spectrum. We attribute these discrepancies to the fact that there are many dynamical processes, such as upconversion and energy transfer, which are occurring in the Er^{3+}-doped lead silicate glass that influence the experimental spectrum. We were unable to simulate these processes due to the constraints of our present model. As a result, further work and a more sophisticated model is required.

6.2. FUTURE WORK

In this thesis, an in depth investigation on the structure and optical properties of rare-earth ions doped in lead silicate glasses was performed using computer simulation techniques. The goal was to provide a detailed structural analysis of the local environment of the rare-earth ion using a three-body potential model and to calculate the corresponding emission spectrum. Any future work, would involve the improvement of both the methods used: the first is with respect to the potential function used in the molecular

dynamics simulation and the second is in the point-charge crystal-field method used to generate the spectra.

Specifically, the following points should be considered in greater detail:

(i) To improve the computational procedure, further parameterization of the potential parameters is required. One of the primary structural characteristics in lead silicate glass is the polarizability of the lead ions. The present three-body potential model, used in this thesis, takes into account the partial covalency of the lead ions but does account for the polarizability. There are two methods that can be employed to include polarizability in a potential model. The first would be to introduce a polarizability term directly into the potential function. This has been done very successfully in simulations of water [164,165], but does result in more intense computational calculations. However, with the advent of technology, faster computers are becoming more and more available, and computing power is not as large an obstacle as it was in the past. The second option would be to include a floating charge for the lead ion, which would represent the electronic distribution of charge. This method is much more difficult, but would provide a more realistic interpretation.

(ii) Improvements to the three-body potential parameters could be made using *ab intio* methods, such as Hartree-Fock calculations on small clusters of ions.

(iii) Using the angular overlap model would improve the covalent term in the crystal-field model.

(iv) A more in depth study of the clustering of the rare-earth ions should also be performed. The main reason for studying the clustering of erbium ions is to examine the possibility of intercluster and cluster-to-cluster energy transfer. In

order to do this, dynamical processes should be included into the calculation of the simulated spectra. One suggestion could be the inclusion an ion-ion coupling term in the perturbation Hamiltonian. Moreover, non-radiative transitions due to single and multiphonon processes, which effect the rate of energy transfer, could also be calculated by including an ion-lattice coupling term into the perturbation Hamiltonian.

(v) Once an accurate model, which accounts for dynamical processes, has been developed, we will be in a position to simulate the upconversion process. The calculations will entail the simulation of co-doped Er^{3+}/Yb^{3+}-lead silicate glasses.

CHAPTER 7

7.0 REFERENCES

1. W. M. Yen, in Optical Spectroscopy of Glasses, I. Zschokke ed., D. Reidel Publishing Company, (1986) 23.

2. J.S. Nordyke, Lead in the World of Ceramics – A Source Book for Scientists, Engineers and Students, The American Ceramic Society, Inc., (1984) 11.

3. G.E. Rindone, in Luminescence of Inorganic Solids, P. Goldberg ed., Academic Press (1966) 419.

4. C.R.A. Catlow, Am. Rev. Mater. Sci., 16 (1986) 517.

5. A. Paul, in Chemistry of Glasses, Chapman and Hall, London (1990).

6. W.A. Weyl and E. C. Marboe in The Constitution of Glasses: A Dynamic Interpretation, Vol I., Wiley (Interscience) (1963).

7. A.C. Wright, in Experimental Techniques of Glass Science, C.J. Simmon and O.H. El-Bayoumi eds., The American Ceramic Society, (1993) 205.

8. H. Scholze, in Glass Nature, Structure and Properties, M.J. Lakin translated, Springer-Verlag (1991).

9. W.H. Zachariasen, J. Am. Chem. Soc., 54 (1932) 3841.

10. B.E. Warren, H. Krutter and O. Morningstar, J. Am. Ceram. Soc., 19 (1936) 202.

11. V. M. Goldschmidt, Norsk. Vid. Akad., Oslo No. 8, (1926).

12. B.E. Warren and J. Biscoe, J. Am. Ceram. Soc., 21 (1938) 259.

13. F. Zernicke and J. A. Prins, Z. Phys., 41 (1927) 184.

14. P. Debye and H. Menke, Z. Physik, 31 (1930) 797.

15. A.A. Lebedev, Bull. Acad. Sci. USSR, Phys. Ser. 4 (1940) 584.

16. J.T. Randall, H. R. Rooksby and B. S. Cooper, J. Soc. Glass Tech., 14 (1930) 219.

17. N.N. Valenkov and E. A. Porai-Koshitz, Z. Krist., 95 (1936) 195.

18. M. L. Huggins, J. Am. Ceram. Soc., 38 (1955) 172.

19. L. W. Tilton, J. Res. Nat. Bur. Stand., 59 (1957) 139.

20. H. A. Robinson, J. Phys. Chem. Solids, 26 (1965) 209.

21. R. L. Mozzi and B.E. Warren, J. Appl. Cryst. 2 (1969) 164.

22. P. W. Wang and L. Zhang, J. Non-Cryst. Solids, 194 (1996) 129.

23. K. Yamada, A. Matsumoto, N. Niimura, T.Fukunaga, N. Hayashi and N. Watanabe, J. Phys. Soc. Japan, 55(3) (1986) 831.

24. J. A. Capobianco, G. Prevost, P. P. Proulx, P. Kabro and M. Bettinelli, Opt. Materials, 6 (1996) 175.

25. E.M. Rabinovich, J. Mat. Sci., 11 (1976) 925.

26. G. J. Bair, J. Am. Ceram. Soc., 19 (1936) 339.

27. J. Krough-Moe, Zs. Physikalische Chem. Neue Folge 18 (1958) 223.

28. G. O. Bagdyk'yants and A. G. Alekseev, in The Structure of Glass, Vol 2., (Transl. from Russian) Consultants Bureau, (1960) 198.

29. G. Brosset, Phys. Chem. Glasses, 4 (1963) 99.

30. M.F. Mydlar, N.J. Kreidel, J.K. Hendren and C.T. Clayton, Phys. Chem. Glasses, 11(6) (1970) 196.

31. L. Liu, Z. Phys. B., 90 (1993) 393.

32. T. Fujiu and M. Ogino, J. Non-Cryst. Solids, 64 (1984) 287.

33. H. Morikawa and Y. Takagi, J. Non-Cryst. Solids, 53 (1982) 173.

34. J. Leciejewicz, Acta Crystallogr. 14 (1961) 1304.

35. M. Imaoka, H. Hasegawa and I. Yasui, J. Non-Cryst. Solids, 85 (1986) 393.

36. H. Hosono, H. Kawazoe and T. Kanazawa, Yogya-Kyokai-Shi, 90 (1982) 544.

37. J. Götz, D. Hoebbel and W. Wieker, J. Non-Cryst. Solids 20 (1976) 413.

38. R. M. Smart and E. P. Glasser, Phys. Chem. Glasses, 19 (1978) 95.

39. A. Montenero, L. Dimesso. G. Antonioli, P. P. Lottici and G. Vlaic, in "Conference Proceedings Vol 25 – 2nd European Conference on Progess in X-Ray Synchrotron Radiation Research", A. Balerna, E. Bernieri and S. Mobilio eds., Bologna (1990).

40. R. Dupree, N.Ford and D. Holland, Phys. Chem Glasses, 28(2) (1987) 78.

41. G.C. Cormier, T. Peres and J.A. Capobianco, J. Non-Cryst. Solids, 195 (1996) 125.

42. E. M. Levin and S. Block, J. Am. Ceram. Soc., 40 (1957) 95, 113.

43. D. K. Rice and L. G. DeShazer, Phys. Rev. B., 186 (2) (1969) 387.

44. R. Tomaschek, Trans. Faraday Soc., 35 (1939) 148.

45. G. Cormier, "*Molecular Dynamics Simuation and Crystal-Field Theory: Predicting the optical spectra and structure of rare-earth doped inorganic glasses*", PhD. Thesis, Concordia University, 1993.

46. P. K. Gallagher, C. R. Kurkjian and P. M. Bridenbaugh, Phys. Chem. Glasses, 6 (3) (1965) 95.

47. D. K. Rice and L. G. DeShazer, J. Chem. Phys., 52(1) (1970) 172.

48. M. M. Mann and L. G. DeShazer, J. Appl. Phys., 41(7) (1970) 2951.

49. C. Bresher and L. A. Riseberg, Phys. Rev. B., 3(1) (1976) 81.

50. C. Bresher and L. A. Riseberg, Phys. Rev. B. 21(6) (1980) 2607.

51. S. A. Brawer and M. J. Weber, Phys. Rev. Lett. 45 (6) (1980) 460.

52. S. A. Brawer and M. J. Weber, J. Non-Cryst. Solids, 38&39 (1980) 9.

53. S. A. Brawer and M. J. Weber, J. Chem. Phys., 75(7) (1981) 3522.

54. M. J. Weber and S. A. Brawer, J. Non-Cryst. Solids, 52 (1982) 321.

55. M. J. Weber and S. A. Brawer, J. Phys. (Paris) Coll. C9 suppl. au n°12, tome 43, (1982) 291.

56. K. Hirao and N. Soga, J. Am. Ceram. Soc., 68 (10) (1985) 515.

57. G. Cormier, J. A. Capobianco, C. A. Morrison and A. Monteil, Phys. Rev. B., 48 (22) (1993) 16290.

58. G. Cormier and J. A. Capobianco, Europhys. Lett., 24(9) (1993) 743.

59. G. Cormier, J. A. Capobianco and C. A. Morrison, J. Chem. Soc. Faraday Trans., 90(5) (1994) 755.

60. S. Chaussedent and A. Monteil, J. Phys. Chem., 105(5) (1996) 6532.

61. S. Chaussedent, M. Monteil, M. Ferrari and L. Del Longo, Philos. Mag. B., 77(2) (1998) 681.

62. S. Chaussedent, *'Etude par simulation numérique de la structure et de la dynamiue d'un ion luminescent en solution dans l'eau. Calcul des propriétés spectroscopiques.'*. PhD. Thesis, Université d'Angers UFR Sciences, 1997.

63. A. Renuka Devi and C. K. Jayasankar, J. Non-Cryst. Solids, 197 (1996) 111.

64. R. Reisefeld and Y. Eckstein, J. Solid-State Chem., 5 (1972) 174.

65. R. Reisefeld, R. Veapoldi, L. Boehm and M. Ish-Shalom, J. Solid State Chem., 75(26) (1971) 3980.

66. J. T. Fournier and R. H. Bartram, J. Chem. Phys. Solids, 21 (1970) 2615.

67. C.C. Robinson, J. Non-Cryst. Solids, 15 (1974) 1.

68. C.C. Robinson, J. Non-Cryst. Solids, 15 (1974) 11.

69. M. Wolf and J. O. Thomas, J. Mater. Chem., 4(6) (1994) 839.

70. M. A. Marcus and A. Polman, J. Non-Cryst. Solids, 136 (1991) 260.

71. S. K. Barber, in Interaction of radiation with solids, A. Bishay ed., Plenum, (1967) 593.

72. C. C. Robinson and J. T. Fournier, Chem. Phys. Lett., 3(7) (1969) 517.

73. C. C. Robinson and J. T. Fournier, J. Phys. Chem. Solids, 31 (1970) 895.

74. S. Mockovciak, J. Pantoflicek and K. Patek, Phys. Stat. Sol., 11 (1965) 401.

75. K. R. Lea, M. J. M. Leask and W. P. Wolf, J. Phys. Chem. Solids, 23 (1962) 1381.

76. K. W. H. Stevens, Proc. Phys. Soc. Lond. A65 (1952) 209.

77. R. J. Elliott and K. W. H. Stevens, Proc. Roy. Soc., A218 (1953) 553.

78. M. Wolf, S. Edvardsson, M. A. Zendjas, J. O. Thomas, Phys. Rev. B., 48(14) (1993) 10129.

79. C.R.A. Catlow, R. G. Bell and J. D. Gale, J. Mater. Chem., 4(6) (1994) 781.

80. W. F. van Gunsteren and H. J. C. Berendsen, Angew. Chem. Int., Ed. Engl., 29 (1990) 992.

81. K. Kremer, in Computer Simulation in Chemical Physics, M. P. Allen and D. J. Tildesley eds., Kluwer, Dordrecht (1993).

82. M.P. Allen and D. J. Tildesley, Computer Simulation of Liquids, Oxford University Press, London (1987).

83. M. P. Allen, Philos. Trans. R. Soc. London, Ser. A., 334 (1993) 323.

84. C. R. A. Catlow and W. C. Mackrodt, Computer Simulation of Solids, Lecture Notes in Physics, 166, Springer-Verglag, Berlin (1982).

85. J. H. Simmons, R. Ochoa and T. M. Neidt, in Experimental Techniques of Glass Science, C. J. Simmon and O. H. El-Bayoumi eds., The American Ceramic Society (1993).

86. D. Fincham and D. M. Heyes, in Advances in Physics, Vol. LXIII, (1985).

87. C. R. A. Catlow, C. M. Freeman, M. S. Islam, R. A. Jackson, M. Leslie and S. M. Tomlinson, Philos. Mag. A., 58(1) (1988) 123.

88. B. J. Alder and T. E. Wainright, J. Chem. Phys., 27 (1957) 1208.

89. A. Rahman, Phys. Rev. A., 136(2A) (1964) 405.

90. L. V. Woodcock, C. A. Angell and P. Cheeseman, J. Chem. Phys. 65 (4), (1976) 1565.

91. T. F. Soules, J. Chem. Phys., 71(11) (1979) 4570.

92. S. K. Mitra, M. Amini, D. Fincham and R. W. Hockney, Phil. Mag. B. 43(2) (1981) 365.

93. S. K. Mitra, Phil. Mag. B., 45(5) (1982) 529.

94. S. K. Mitra and R. W. Hockney, Phil. Mag. B., 48(2) (1983) 151.

95. B. P. Feuston and S. H. Garofalini, J. Chem. Phys. 89(9) (1988) 5818.

96. F. H. Stillinger and T. A. Weber, Phys. Rev. B., 31(8) (1985) 5262.

97. R. G. Newell, B. P. Feuston and S. H. Garofalini, J. Mater. Res., 4(2) (1989) 434.

98. P. Vashishta, R. K. Kalia, José P. Rino and I. Ebbsjö, Phys. Rev. B., 41(17) (1990) 12197.

99. B. Vessal, M. Amini, M. Leslie and C. R. A. Catlow, Mol. Sim., 5 (1990) 1.

100. J. J. Pluth, J. V. Smith and J. Faber Jr., J. Appl. Phys., 51 (1985) 1045.

101. J. A. Barker and D. Henderson, Rev. Mod. Phys., 48 (1976) 587.

102. J. P. Hansen and I. R. MacDonald, Theory of Simple Liquids, Academic, London (1976).

103. M. L. Lockhead and K. L. Bray, J. Non-Cryst. Solids, 170 (1994) 143.

104. J. Braunstein, G. Mamanton and G. P. Smith, Advances in Molten State Chemistry, Plenum Press, New York (1975).

105. G. Cormier, J. A. Capobianco and C. A. Morrison, J. Non-Cryst. Solids, 168 (1994) 115.

106. B. G. Wybourne, Spectroscopic properties of rare-earths, Interscience (1965).

107. J. M. Haile, Molecular Dynamics Simulation, Elementary Methods, John-Wiley and Sons Inc., New York (1992).

108. A. Nordsieck, Math. Comput., 16 (1962) 22.

109. H. A. Bethe, Ann. Physik, 3 (1929) 133.

110. S. Hüfner, Optical Spectra of Transparent Earth Compounds, Academic Press Inc., London (1978).

111. B. Z. Malkin, in Spectroscopy of Solids Containing Rare Earth Ions, A. A. Kaplyanskii and R. M. Macfarlane eds., Elsevier Science Publishing Company Inc., (1987).

112. B. Hendersen and G. F. Imbush, Optical Spectroscopy of Inorganic Solids, Oxford Science Publications, New York, (1989).

113. S. Tanabe, K. Tamai, K. Hirao and N. Soga, Phys. Rev. B., 47 (1993) 2507.

114. L. H. Thomas, Nature, 107 (1926) 514.

115. J. Frenkel, Z. Phys. 37 (1926) 243.

116. G. H. Dieke, Spectra and energy levels of rare-earth ions in crystals, Interscience, (1968).

117. W. T. Carnall, P. R. Fields and K. Rajnak, J. Chem Phys., 49(10) (1968) 4450.

118. C. A. Morrison and R. P. Leavitt, in Handbook on the Physics and Chemistry of Rare-Earths, K. A. Gschneider and L. Eyring eds., North-Holland, (1982) chap. 46.

119. R. Reisfeld, in Structure and Bonding, Vol. 13, J.D. Dunitz, P. Hemmerich, J. A. Ibers, C. K. Jørgensen, J. B. Neilands, Sir Ronald S. Nyholm, D. Reinen and R. J. P. Williams eds., Springer-Verlag, (1973).

120. C. A. Morrison, Crystal-fields for transition-metal ions in laser host materials, Springer-Verlag, (1992).

121. R. P. Leavitt, C. A. Morrison and D. E. Wortman, Rare earth ion-host crystal field interactions 3. Three-parameter theory of crystal fields, Harry Diamond Laboratories Report TR-1673 (1975).

122. S. Fraga, K. M. S. Saxena and J. Karwowski, Physical Science Data 5. Handbook of atomic data, Elsevier, New York (1976).

123. R. M. Sternheimer, M. Blume and R. F. Peierls, Phys. Rev., 173 (1968) 376.

124. R. P. Leavitt, C. A. Morrison and D. E. Wortman, Harry Diamond Laboratories Report HDL-TR-1673, NTIS#AD-A017-849, (1975).

125. C. A. Morrison and R. P. Leavitt, J. Chem. Phys., 71(6) (1979) 2366.

126. R. S. Drago, Physical Methods in Chemistry, W. B. Saunders Company, Philadelphia, (1977).

127. M. Tinkham, Group theory and quantum mechanics, McGraw-Hill, New-York, (1964).

128. R. D. Peacock, in Structure and Bonding, Vol. 22, J. D. Dunitz, P. Hemmerich, R. H. Holm, J. A. Ibers, C. K. Jørgensen, J. B. Neilands, D. Reinen and R. J. P. Williams eds., Springer-Verlag, (1975).

129. B. DiBartolo, Optical Interactions in Solids, John Wiley and Sons, New York, (1968).

130. E. U. Condon and G. H. Shortley, The theory of atomic spectra, Cambridge University Press, (1957).

131. B. R. Judd, Phys. Rev., 127(3) (1962) 750.

132. C. A. Morrison, R. P. Leavitt, J. B. Gruber and N. C. Chang, J. Chem. Phys., 79 (10) (1983) 4758.

133. R. P. Leavitt and C. A. Morrison, J. Chem. Phys., 73 (1980) 749.

134. W. F. Krupke, Phys. Rev., 145(1) (1966) 325.

135. M.L. Boucher and D.R. Peacor, Z. Kristallogr. 126 (1968) 98.

136. C. A. Morrison and R. P. Leavitt, Harry Diamond Laboratories, Internal Report, (1991).

137. W. H. Press, B. P. Flannery, S. A. Teukolsky and W. T. Vetterling, Numerical Recipes, The art of scientific computting, Cambridge University Press, (1989) 346.

138. R. E. Christoffersen, Basic Principles and Techniques of Molecular Quantum Mechanics, Springer-Verlag, (1989).

139. M. Misawa, D. L. Price and K. Suzuki, J. Non-Cryst. Solids, 37 (1980) 85.

140. P.A.V. Johnston, A. C. Wright and R. N. Sinclair, J. Non-Cryst. Solids, 57 (1983) 447.

141. A. B. Rosenthal and S. H. Garofalini, J. Non-Cryst. Solids, 87 (1986) 254.

142. A. C. Hannon, B. Vessal and J. M. Parker, J. Non-Cryst. Solids, 150 (1992) 97.

143. B. M. J. Smets and T. P. A. Lommen, J. Non-Cryst. Solids, 48 (1982) 423.

144. E. Lippmaa, M. Mägi, A. Samosan, G. Englehardt and A-R. Grimmer, J. Am. Chem. Soc., 102 (1980) 4889.

145. J. P. Rino, I. Ebbsjö, R.K. Kalia, A. Nakano and P. Vashista, Am. Phys. Soc., 47(6) (1993) 3053.

146. P.P. Lottici, G. Antonioli and A. Montenero, Am. Crystallo. Ass., 27 (1991) 300.

147. T. Peres, D. A. Litton, J. A. Capobianco and S. H. Garofalini, J. Non-Cryst. Solids, 221 (1997) 34.

148. A. Dietzel, Z. Elektrochem, 48 (1942) 9.

149. G. N. Greaves, A. Fontaine, P. Lagarde, D. Raoux and S. J. Gurman, Nature (London) 293 (1981) 611.

150. S. H. Garofalini and S. Levine, J. Amer. Ceram. Soc., 68 (1985)376.

151. C. C. Robinson, J. Chem. Phys., 54(8) (1971) 3572.

152. Th. Kowall, F. Foglia, L. Helm and A. E. Merbach, J. Phys. Chem., 99(1995) 13078.

153. Th. Kowall, F. Foglia, L. Helm and A. E. Merbach, J. Am. Chem. Soc., 117 (1995) 3790.

154. F. H. Spedding, M. J. Pikal and B. O. Ayers, J. Phys., Chem. 70 (1966) 2440.

155. T. Mioduski and S. Siekierski, J. Inorg. Nucl. Chem., 37 (1975) 1647.

156. R.W.G. Wykoff, Crystal Structures 2nd Edition, Interscience, New York, 1963.

157. D. Stauffer, A. Aharony, Introduction to Percolation Theory, 2nd edition, Taylor & Francis, London, (1992).

158. S. D. Stoddard, J. Comp. Phys., 27 (1978) 291.

159. N. Karayianis and C. A. Morrison, Harry Diamond Laboratories, HDL-TR-1682, (1975).

160. W. G. Fately, F. R. Dollish, N. T. MacDevitt and F. F. Bentley, Infrared and Raman selection rules for molecular and lattice vibrations: The correlation method, Wiley-Interscience, New-York, (1972).

161. R. P. Leavitt, C. A. Morrison and D. E. Wortman, J. Chem. Phys., 61(3) (1974) 1250.

162. R. Kuroda, S. F. Mason and C. Rosini, Chem. Phys. Lett., 70(1980) 11.

163. R. Kuroda, S. F. Mason and C. Rosini, J. Chem. Soc. Faraday Trans., 2(77) (1981) 2125.

164. K. Watanabe and M.L. Klein, Chem. Phys., 131 (1989) 157.

165. F. H. Stillinger and A. Rahman, J. Chem. Phys., 60(4) (1974) 1545.